TERAHERTZ TIME-DOMAIN SPECTROSCOPY: FROM PROTEINS TO NANOSTRUCTURES

A Dissertation
Presented to the Faculty of the Graduate School
of Cornell University
in Partial Fulfillment of the Requirements for the Degree of
Doctor of Philosophy

by
Paul A. George
August 2009

TERAHERTZ TIME-DOMAIN SPECTROSCOPY: FROM PROTEINS TO NANOSTRUCTURES

Paul A. George, Ph.D.

Cornell University 2009

This dissertation presents the Terahertz spectroscopy of several systems ranging from proteins to nanostructures. First, Terahertz Time-Domain Spectroscopy is introduced as a unique and powerful technique for studying physical processes that occur at Terahertz frequencies or on picosecond timescales. A detailed analysis of the design, construction, and performance of different types of Terahertz Time-Domain Spectrometers is presented. Next, discussion of the Terahertz frequency response of Bovine Serum Albumin protein and novel integrated photonic components measured using these spectrometers is discussed. In the penultimate and final chapters of this dissertation, the study of the ultrafast carrier dynamics in optically excited epitaxial graphene and germanium nanowires, respectively, using multi-color Optical-Pump Terahertz-Probe Spectroscopy is presented.

BIOGRAPHICAL SKETCH

Paul Anthony George was born on September 4, 1982 to Joseph George, a marine engineer, and Joan Patricia George, an elementary school teacher, in White Plains, NY. He entered this world under the additional graces of his sister, Jennifer George, and a most-appropriately named golden retriever. He grew up in the small town of Purchase, which is not too far from his place of birth, and attended Purchase Elementary School and later Louis M. Klein Middle School. While growing up, he enjoyed playing sports – ice hockey, baseball, lacrosse (the mortal enemy of baseball), and skiing –, playing the piano and the trombone, spending time with his friends, and participating in a whole host of other activities that normally keep kids occupied. Paul's roots as an engineer were sown at an early age when he and his Dad spent lots of time building plastic models (including a majestic space shuttle which met an unfortunate end under a falling stack of books), model rockets, working on cars, and fixing things around the house. Upon entering the ninth grade, Paul chose to switch school districts and attend Mamaroneck High School. There, his interests in math and science peaked – perhaps regrettably at the expense of his other academic responsibilities – partly due to inspiration from several important teachers. In eleventh and twelfth grade, his future as an engineer became all but solidified. Next stop, college.

Paul attended Cornell University and enrolled as a freshman in August, 2000. In retrospect, the decision to attend Cornell was a relatively easy one – it may have even been made in 1996 when he first came to the University with his sister for a tour – and proved to be the right one without an iota of doubt. At Cornell, Paul pursued Electrical and Computer Engineering with an initial focus on Computer Architecture. His interests took a dramatic shift during the

Spring 2003 semester when he took his first course on Quantum Mechanics. He found the material fascinating because of its seemingly mysterious and counter-intuitive nature. This one class inspired him to pursue similar coursework and the rest, as they say, is history. As an undergraduate, Paul spent lots of time doing things other than studying. He played on the club hockey team, participated in several strategic student committees, was an officer in several student organizations, was an Engineering Ambassador, and developed an incredible group of friends that he certainly will always have. In May 2004, shortly prior to graduation, he was awarded the Merrill Presidential Scholarship which gave him the opportunity to share his success and say ”thank you” to a very-deserving high school math teacher. He considers this his most important academic honor.

Following his completion of the undergraduate curriculum, Paul elected to stay at Cornell to pursue a Masters of Engineering degree in Electrical and Computer Engineering under his soon-to-be PhD advisor, Farhan Rana. His M.Eng, as it’s known, was atypical in that it had a distinct research focus and ultimately led him into the PhD program at Cornell. Even though staying at Cornell for an additional several years to pursue a PhD was a tough decision, it proved to be a good one. His thesis work, again conducted under Farhan Rana, focused on the spectroscopy of systems at Terahertz frequencies. In July 2009, after nine years at Cornell University, his stay as a student was complete.

To those whose names with which I am adorned. For your efforts and the opportunities they have afforded me. You deserve this.

ACKNOWLEDGEMENTS

I have always believed that the Acknowledgements section is one of the most intriguing sections of any thesis. Encoded in the cryptic little snippets about important people and things strewn throughout this section are a world of experiences and relationships that helped define and mold a graduate student’s career and life. It is through this section that the reader gets some insight into the emotional roller-coaster that is graduate school. What this section lacks in academic stimulation, it undoubtedly makes up for in emotional content and intrigue.

My nine year term as a student at Cornell can be nicely partitioned into my undergraduate era and my graduate era, although I have had several dear friends that have been with me through my entire experience. Let me start by acknowledging them. First, many thanks to my best friends (in alphabetical order) Brian, Burk, Peter and Soneru. Looking back upon all of the great times we had and continue to have together makes me somewhat humble and infinitely appreciative of the quality of our friendship. Next, many thanks to my dearest girl friend - in this case, I mean ”friend-who-is-a-girl” - Jen. Our relationship started during our Senior year, but has grown ever strong since. I cannot thank you enough for your wonderful set of ears, your big heart, and you devotion to the Pittsburgh Penguins! Finally, I’d like to thank my friend Avi for laying it down straight-up.

Thanks to my dear friend Martin Schubert. Our relationship was unique and was characterized by common interests of both the leisure and academic type. I am grateful for taking all of my classes with you and for participating in our many long-winded and very enlightening blackboard/whiteboard discussions. I maintain, to this day, that the crux of my learning as an undergrad stemmed from those detailed - and sometimes heated! - discussions. And, what better mind to have the with? Thanks!

I'd like to thank my friends in the Duffield graduate student office on the third floor. Despite the many shenanigans, I'm pretty sure we still managed to get some stuff done. This list is long, so the omission of a name is not meant as an effrontery, but rather is a failure on my behalf. Starting from my end and working down, here goes. Many thanks to Sunwoo, Omeed, Giorgios, Mustansir, Xiiiiiiiiiiiaaaaaaaaaaaaaoooooooo (Xiao), Rajeev, Suresh, Tiffany, Weinstein (a.k.a. Professor), Eugene (a.k.a. Eugio, a.k.a. Eug), Johnny D. and Rick (at the far end). Also, many thanks to the Phillips and Rhodes ECE crowd: Sasi, Sasha (Alex), Carl, Brad, Jacob, Long, Ania and Colton. Thank you Nini for being so important in my life over the past several years, for laughing and talking, and for all the amazing cooking! I'd like to also thank Shayaan, Shankar, and Simelgor for all of their fabrication advice and for ultimately making my life in the CNF easier and more fruitful.

At this point, I turn to my research group both present and past. First, special thanks to Jared for coming in and so seamlessly taking over our THz work. I feel very confident that the next few years of your career will be marked by tremendous success. The same goes for Haining. Despite your (relative) youth, you're dedication and work ethic will serve you well. Thanks to Dave, as well, even though you did introduce me to annoying K-Pop and BOA. Thanks to our undergrads Justin, Misha, and Wallace. You guys are good and will only continue to get better.

Next, a very special to thanks to my great friends and former research colleagues Messieurs Jahan Dawlaty and Faisal Ahmad (to whom I dedicate the first sentence of this thesis). Your contributions to my career are so substantial that they merit their own paragraph. We grew up together as students - although you both are admittedly older and, with that, more mature! - and learned together. Our frequent discussions helped me grow as a thinker. To Jahan, thank you for your relentless professionalism (and, ”Dude! OK, OK, OK!”). And Faisal, I’m pretty sure you’re the nicest person I’ve ever met

It is true that a tall building is only as mighty as its foundation. On that note, I turn to those people that really (seriously, really) made it happen. Without you all, I don’t know where I would be. First, thanks to Dan and Jamie (especially for the bowls of M&M’s) in Phillips. Next, a huge thanks to Scott Coldren for helping me stay organized, for bending the occasional rule to help me sidestep some of the formalities and bureaucracy, for talking about music and Tom Clancy, for having a set of open ears, and for persistently sending me all of those emails despite the fact that you knew I wouldn’t read them! And, undoubtedly, I would be nowhere with my loading-dock sweethearts. Thank you so much Cheryl Francis and Dorothy (”L.A. Woman”) Palladino. You guys rock!

A very special thanks to my research advisor Professor Farhan Rana for providing me with the insight, guidance, intuition, and inspiration for all these years. Our relationship dates back to 2003 when I first dropped into your office to ask you about the effective mass of electrons in Si. Needless to say I was, and continue to be, impressed when you answered without hesitating or consulting a book! I’d also like to thank my committee members for both being committee members and for the inspirational courses they taught that ultimately led me down the PhD track. Thank you Professor Edwin Kan (ECE 457, Fall 2003) and Professor Frank Wise (A&EP 450, Fall 2003, and A&EP 440, Spring 2004). I’d also like to thank Professor Gaeta, Professor Buhrman and Professor Lipson for helping inspire me. Special thanks to Professor Pollock for letting me build my first THz spectrometer in your lab! Thanks to Professor Bhave for all of the enlightening conversations as well as for ”occasionally” serving as a proxy in my exams. Finally, thanks to my teacher and friend Mr. Gill. Even though it has been over a decade since I first sat in your class, you are without a doubt still my teacher.

During my graduate career, I began a small career as an entrepreneur when I co-founded VideoNote. My experiences running a small company have proved challenging but very enlightening in their own regard. With that, I'd like to thank Ryan Morris, my business partner and friend. I look upon our future successes with optimism.

Thanks to my dearest and most unlikely friend Zana. You have been, without a doubt, my closest confidant and friend during my graduate student career. With you I have grown and begun to see and understand life in a very different way. Thank you for helping me through some tough times and for inspiring me to push on. Most of all, thank you for being *not*-me.

Last, but not least, to my family. Thank you so, so much for giving me the opportunity to pursue my dreams. To Mom and Dad (p.s. thanks for letting me constructively procrastinate for five more years!), to Jenn and Andrew, to Uncle John, to Chris and Jeff, to Grandma and Grandpa George, to Grandma and Grandpa Strati (everyday for the past four years, I have looked upon your WWII pictures with pride and humility for inspiration), and to George and Spikey (because dogs are family members too). Thank you all. I love you dearly and miss you very much.

TABLE OF CONTENTS

LIST OF TABLES

LIST OF FIGURES

CHAPTER 1

AN INTRODUCTION TO TERAHERTZ TIME-DOMAIN SPECTROSCOPY

1.1 The Electromagnetic Spectrum

These are indeed very exciting times. The electromagnetic spectrum – the scale onto which the oscillatory speed of electromagnetic waves is mapped – has been almost entirely conquered from DC all the way to X-Rays. To date, human beings have found a variety of ways of generating, manipulating, detecting and (most importantly) utilizing all different types of electromagnetic waves. Even thousands of years ago, well before James Clerk Maxwell's penning of a system of equations that so elegantly describe the origins of electromagnetic waves, humans relied upon optical frequency (visible light) and infrared frequency (heat) electromagnetic radiation from the Sun and fire to grow crops, cook dinner, and forge weapons. Today, armed with an intimate knowledge of both how these waves work as well as the processes by which they are created, man's utilization of electromagnetic waves has grown tremendously. A quick survey of the electromagnetic spectrum serves as a demonstration of this. First, however, some nomenclature. Electromagnetic waves are typically characterized by one of two quantities: wavelength (units: meters) or frequency (units: Hertz, abbreviated Hz = one oscillation of the electromagnetic wave per second). It is well known that the wavelength and frequency of a wave are inversely related by the multiplicative factor c, the speed of light.

One of the most pervasive types of electromagnetic waves that we encounter on a daily basis, that of alternating-current (AC) electricity, occupies the extreme low end of the spectrum and oscillates at a frequency of 60 Hz in the

United States of America. The spectrum ranging from near 0 Hz (also known as DC) through several hundred Megahertz (MHz, one million Hertz) is spanned by different types of communication systems, including deep-ocean submarine communication (50 Hz), AM radio (100 KHz) and FM radio (100 MHz). At higher frequencies ranging from several Gigahertz (GHz, one billion Hertz) to several hundred GHz, there exist microwave or radio-frequency (RF) devices with applications in computer processors, cell phones, microwave ovens, astronomy, and radars. This entire regime of the electromagnetic spectrum has been thoroughly explored and is ripe with mechanisms for generation.

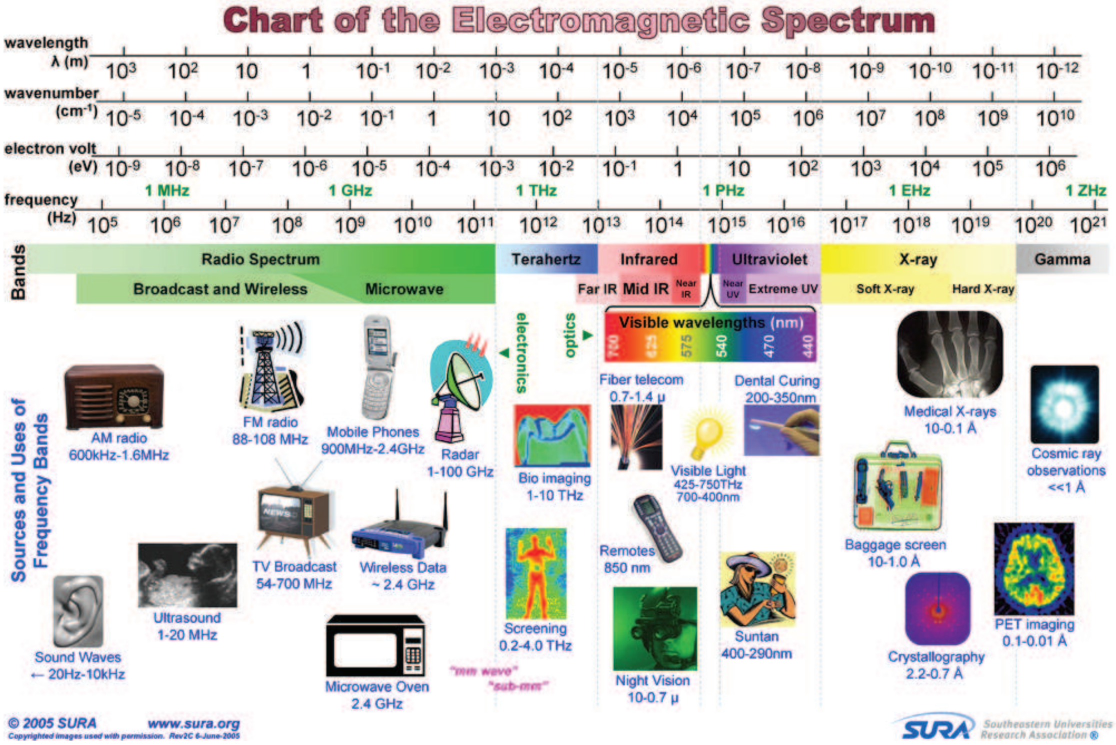

Figure 1.1: The electromagnetic spectrum and its applications from DC through Gamma Rays.

Electromagnetic waves less than 500 GHz have a suitably low frequency that they can be generated electronically from semiconductor-based oscillators. For completeness, it should be mentioned that high power RF devices, such as the phased-array radar of an Aegis missile cruiser or the Arecibo radio astronomy observatory in Puerto Rico, utilize massive klystron or magnetron vacuum-based free-electron sources. The power generating capabilities of these devices dwarfs that of their semiconductor counterparts and extends into the several Megawatt (MW, one million Watts) range. Unfortunately, neither free-electron devices nor semiconductor oscillators can be scaled to operate at frequencies much above 500 GHz with either ease or efficiency. At frequencies higher than 500 GHz, there exists a gap in the electromagnetic spectrum.

On the opposite side of this gap lands us in the infrared and optical regimes of the electromagnetic spectrum. The frequency of this portion of the spectrum is so high – in the Petahertz (PHz, one million billion Hertz) range – and it is customary to characterize these waves in terms of their wavelengths. Starting near 30 μm (1 μm = one millionth of a meter) and ending near 2 μm is the mid-infrared spectrum that is useful for thermal imaging, night vision, industrial fabrication, and studying space. At wavelengths between 2 μm and 700 nm (1 nm = one billionth of a meter) exists the near-infrared which is home to the all-important 1550 nm optical telecommunication portion of the electromagnetic spectrum. Electromagnetic waves at shorter wavelengths between 700 nm and 400 nm are visible to humans and vary in color from red to blue. It would be a dramatic understatement to merely remark that the visible portion of the electromagnetic spectrum is important to all creatures of the Earth.

Electromagnetic waves in the infrared and optical portions of the spectrum have frequencies that are too high to be generated electronically, as mentioned earlier. Instead, these types of waves are typically created using resonant energy transitions of electrons in materials. This emission process takes on two forms –

incoherent spontaneous emission, as is found in light-emitting diodes, and coherent stimulated emission, as is found in lasers (laser is an acronym for **l**ight **a**mplification by **s**timulated **e**mission of **r**adiation) – and ultimately involves the creation of a photon, or quantum of electromagnetic radiation, by an electron as it loses energy. At even higher frequencies and shorter wavelengths, the electromagnetic spectrum enters the ultra-violet (UV), X-Ray, and finally Gamma Ray regions. It should be noted that, even though the electromagnetic radiation that we use to cook a potato in the microwave and the visible electromagnetic radiation that helps us see are seemingly very different in nature, they are actually quite similar with the only difference being frequency. In fact, the same set of physical laws and equations governs the existence and behavior of all electromagnetic waves.

1.2 The Terahertz Gap

Now, the gap. The region of the spectrum that spans from 700 GHz all the way to 10,000 GHz (a wavelength of 30 μm) is the under-utilized Terahertz frequency range (THz, one trillion Hertz). Fundamentally, the reason that the THz range is, to date, known as the ”THz Gap” is a consequence of scale. Terahertz frequencies are too high to be accessed electronically – recall that semiconductor oscillators can only efficiently reach frequencies of up to 800 GHz and are ultimately limited by the speed at which electrons can move – and are too low to be generated from lasers or similar devices. To understand this latter point, it is first important to understand the concept of black-body radiation.

Max Planck was the first to correctly describe the electromagnetic radiation that is emitted by a hot ″black-body″ – this can literally mean a hot black box with a hole in it. As Planck showed, the emission characteristics of these so-called black-body radiators is determined entirely by their temperature and is governed by an equation known as Planck's Law. At room temperature (300 K), the black-body spectrum is centered in the THz frequency range. This fundamental fact has presented a large impedance to the development of THz sources and detectors. At a very basic level, any potential THz laser would require isolation from this ″sea of noise″ in order to operate. The only way to escape this overwhelming amount of black-body noise is to operate THz emission devices are cryogenic temperatures; this is hardly an acceptable approach for making useful devices that are suitable for integration into everyday life. To date, there exist no promising room-temperature THz emitters that are capable of producing even milliwatt power levels.

Unfortunately, utilization of the THz portion of the electromagnetic spectrum suffers from a veritable ″chicken-or-the-egg″ style debate. Given the lack of useful sources and detectors, the incentive to pursue applications that use THz radiation is reduced. Conversely, given the lack of current applications – which may or may not stem from the lack or sources, as the logical spiral goes –, the motivation for researches to pursue room-temperature THz sources has also been somewhat reduced. Nonetheless, the potential applications of THz technology are numerous. First, THz radiation is currently being used for satellite communication. It is also being proposed for uses in high-resolution imaging systems for security screening in place of/addition to current RF or optical systems. Because the resolution of an imaging system is inversely proportional to the frequency of electromagnetic wave used, imaging with THz waves offers substantially higher resolution than does imaging with GHz waves. Terahertz frequency waves are similar to X-Rays in that they can propagate through materials that absorb optical radiation, such as clothing. Importantly, though, THz radiation is not ionizing as are X-Rays, and does not cause the generation of free-radicals (essentially liberated electrons inside a cell) that can lead to serious maladies. While many important applications for THz radiation have been proposed, it is difficult to say with conviction which may ever be realized. The pursuit of technology which utilizes THz electromagnetic waves is far from complete. The gap persists.

1.3 THz in the Time Domain

In light of its unfortunate shortcomings, THz technology in its current state has one very important use: science. With the development of ultrafast electronic switches, researches have been able to create THz-based spectroscopy systems in laboratories across the world. While these systems offer little to no practical use because of their bulk, cost and limited efficiency, their unique capabilities poise them as incredibly useful tools for studying certain types of physical phenomena. Terahertz radiation can be used to probe processes that resonate at THz frequencies – think of a mass-on-a-spring that can oscillate one trillion times per second – as well as processes that occur on picosecond (ps, one billionth of a second) timescales. Some examples of the phenomena that can be studied using THz frequency spectroscopy include the rotational and vibrational modes of gases, the conformational state of proteins and DNA, phonons modes of solids, excitons in semiconductor quantum dots, the plasmon resonances of semiconductor nanowires, and the ultrafast dynamics of electrons in semiconductor nanostructures. The experimental apparatus which is the workhorse for performing these THz frequency measurements in called the THz Time-Domain Spectrometer (THz-TDS).

The most salient feature of THz-TDS systems is that they measure the actual THz electric field in time. Standard optical detectors are essentially just photon counters that measure the incident optical power, which is proportional to the squared-magnitude of the incident optical electric field. By directly measuring the THz electric field, complex phase information relating to the propagation of the THz wave can be measured in addition to its total power. In such, THz-TDS systems enable the determination of the complex properties a material, which is manifested in its complex index of refraction, in a single measurement. Moreover, these systems utilize very short bursts of THz radiation, called few-cycle pulses, that have tremendously broad bandwidths. With a single experiment, the complex response of a material can be measured over a bandwidth of several THz. This type of measurement capability is almost entirely unique to THz spectroscopy. As was previously mentioned, these systems are not commercially, or even practically, viable. Terahertz spectrometers of this ilk can only produce nanowatts (nW, one billionth of a Watt) power levels and occupy a good portion of a large optical table. They also require expensive optical equipment, materials, and external ultrafast lasers to operate.

There is no doubt that the ”Terahertz Gap” in the electromagnetic spectrum still exists. The challenges that must be bested to mend this rift are daunting and are fundamentally physical in nature. Truthfully, this gap may not be closed for some time. In the meantime, though, THz frequency electromagnetic waves have settled into an important niche as a backbone for futuristic scientific research in laboratories across the world.

CHAPTER 2

TERAHERTZ TIME-DOMAIN SPECTROMETERS

2.1 Overview

A rudimentary schematic of a Terahertz Time-Domain Spectrometer is shown in Fig. 2.1. At a basic level, THz-TDS's consist of four fundamental components: (1) an ultrafast pulsed laser source; (2) an emitter; (3) a detector; and, (4) a set of collimating optics. Pulses from the ultrafast laser source are passed through a beamsplitter and are incident upon both the emitter and detector. The emitter is placed at the focus of (typically) a 90-degree off-axis parabolic mirror that both collects and collimates the generated few-cycle pulses of THz radiation. While the number of free-space THz optics varies widely depending on application, the freely-propagating THz pulse is ultimately focused onto the detector with a final parabolic mirror. An ultrafast laser pulse is used to optically gate – turn ″on″ and ″off″ – the detector synchronously with the arrival of the THz pulse thereby enabling detection with femtowatt sensitivity. Because the THz power generated by these systems is usually limited to < 100 nW, a lock-in amplifier is utilized for increased detection sensitivity.

The design, construction, and alignment of a THz-TDS is a nontrivial task that requires much patience. As is true with most custom-built experimental setups, there exist a multitude of ways to build THz-TDS's. While much literature can be found on different types of spectrometers that exist, very few works offer a comparison of the performance and benefits of each. What is worse, the proclaimed performance of each varies depending on specifically who you ask. In actuality, it is nearly impossible to make a perfect comparison between any two

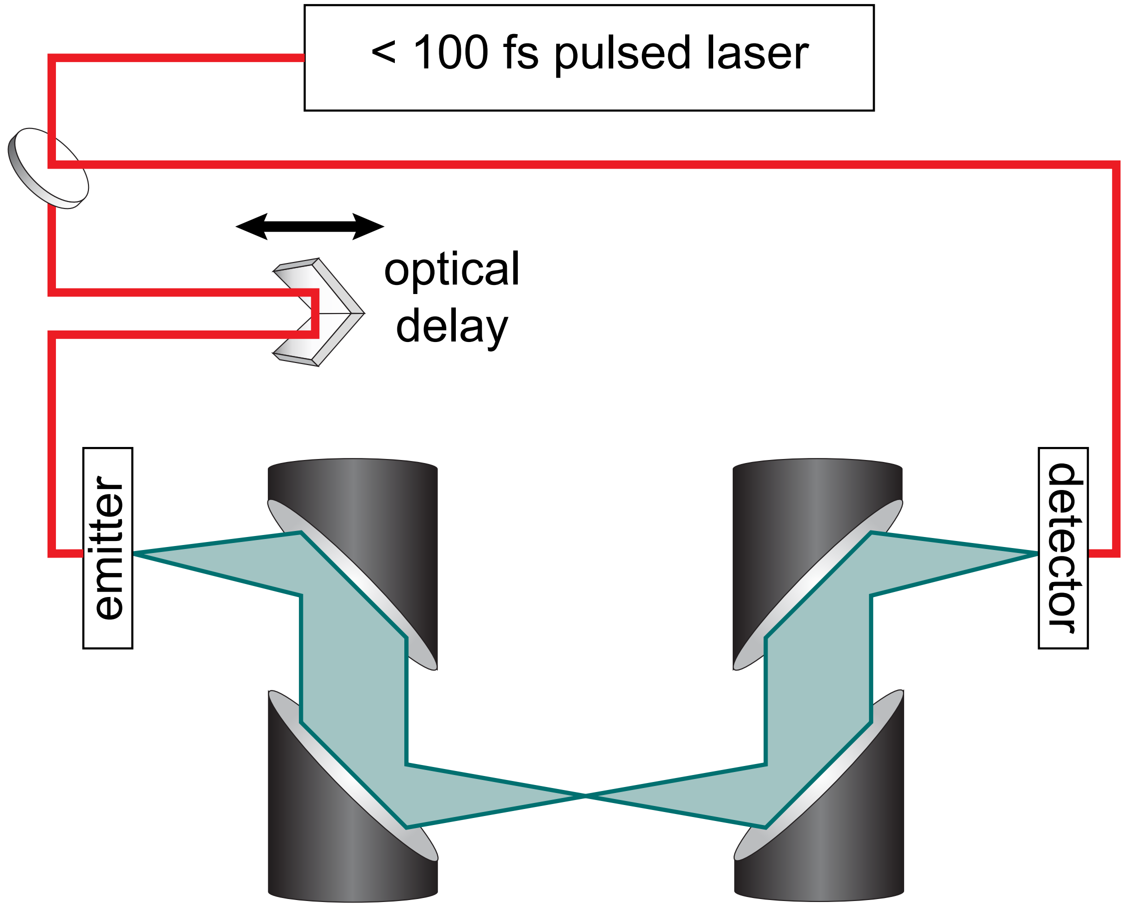

Figure 2.1: A schematic of a basic Terahertz Time-Domain Spectrometer. THz-TDS's consist of four basic components: an ultrafast laser, a THz emitter, a THz detector, and free-space collimating optics. These systems generate few-cycle, ultra-broadband pulses of THz radiation and have power SNR exceeding 10^6:1. The THz electric-field is directly measured in time by sampling it with an ultrafast detector pulse at different temporal delays.

THz spectrometers because the performance of each depends very specifically on many independent variables, including geometry, emitter and detector type, laser power and pulse width, optics choice, etc. In this Chapter, I will present a summary of the several different types of THz-TDS's that I have built, I will discuss the physical mechanisms that underly their operation, and I will comment on the performance, benefits, and downsides of each.

2.2 Ultrafast Laser

While there does exist some flexibility in choosing the emitter/detector pairing, the key component that should ultimately govern the design of the system is the pulsed laser source. Owing to their commercial proliferation, the most commonly utilized pulse laser system for THz spectroscopy is the Ti:Sapphire oscillator. These lasers typically produce <100 fs pulses with energies near 10 nJ and are operate at a center at a wavelength between 780 nm and 800 nm. Regeneratively amplified Ti:Sapphire systems are also commercially available. They offer substantially reduced pulse widths (<35 fs) and increased pulse energies (> 1 mJ), but at a much lower 1 KHz repetition rate. A summary of these pulsed systems is given in Table 2.1.

Table 2.1: A comparison of the pulsed sources commonly used in THz Time-Domain Spectrometers. Amplified systems offer much enhanced pulse energy and peak power. Subsequently, they are well suited for THz generation via optical nonlinear processes.

Source Type	**Pulse Width**	**Pulse Energy**	**Peak Power**
Ti:Sapphire Oscillator (80 MHz)	<100 fs	10-20 nJ	100 KW
Regenerative Amplifier (1 KHz)	<35 fs	1-3 mJ	10 GW

The research presented in this thesis utilized THz-TDS's based exclusively on a 1.5 W Spectra-Physics Tsunami Ti:Sapphire oscillator that routinely produced 90 fs pulses at 81 MHz. Therefore, my discussion of THz emitters and detectors in the following sections will pertain almost entirely to devices compatible with my laser. Although I have no experience with regeneratively amplified lasers, I will briefly mention THz generation using such systems both for completion and as a point of interest.

2.3 Emitters

Terahertz Time-Domain Spectrometers produce few-cycle picosecond pulses of electromagnetic radiation with a center frequency near 1 THz and ultra-wide bandwidths that span 0.1 - 5 THz. From the wave equation for electromagnetic waves in a homogenous media, it can easily be seen that a time-varying current density, $\mathbf{J}(\mathbf{r}, t)$, will couple to propagating electromagnetic waves.

$$\nabla^2 \mathbf{E}(\mathbf{r}, t) = \mu\epsilon \frac{\partial^2 \mathbf{E}(\mathbf{r}, t)}{\partial t^2} + \mu \frac{\partial \mathbf{J}(\mathbf{r}, t)}{\partial t} \tag{2.1}$$

Because $\mathbf{E}$ is related to the first time-derivative of $\mathbf{J}$, the power spectral density of $\mathbf{E}$ will be at least as broad as that of $\mathbf{J}$. Therefore, time-varying currents densities that have spectral components in the THz frequency range will generate THz frequency electromagnetic radiation.

Emitters commonly found in THz-TDS's utilize picosecond or sub-picosecond photogenerated currents to generate few-cycle THz pulses. Figure 2.2 shows a theoretical example of such a time-varying current and the resulting radiated pulse. The current pulse in Fig. 2.2(a) has a high-frequency sharp rising edge that is inversely proportional to the width of the optical excitation pulse and a low-frequency exponentially decaying tail that is due to carrier recombination. As can be seen, the broad spectrum of the radiated pulse is centered near 1 THz and exceeds 4 THz. The two different classes of THz emitter that utilize these current surges will be explained in the following subsections.

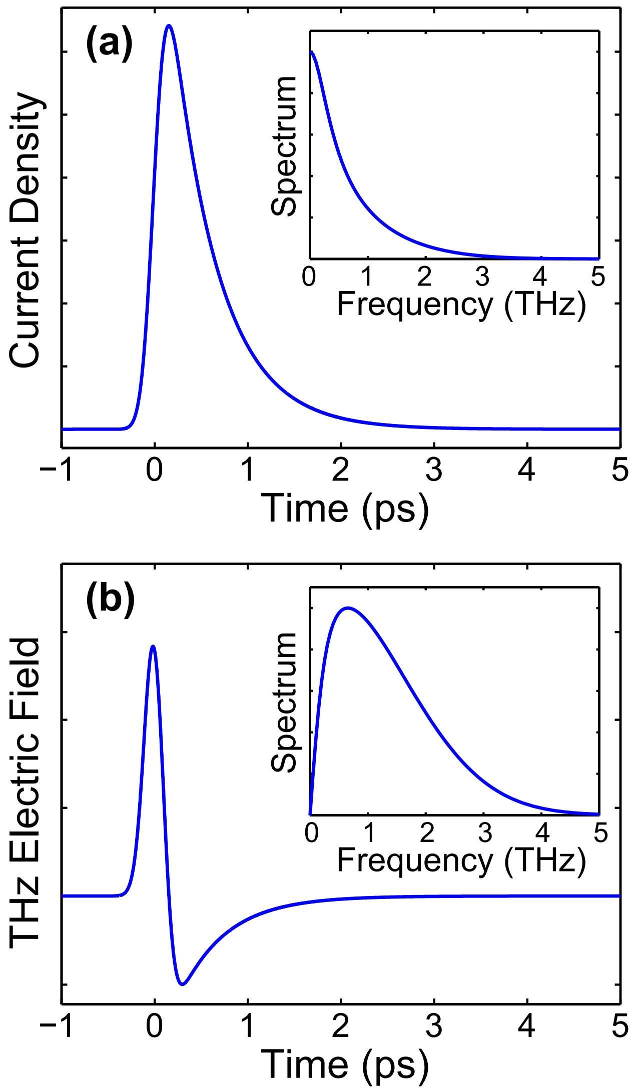

Figure 2.2: The simulated few-cycle THz waveform (b) emitted by a sub-picosecond time-dependent current pulse (a). As can be seen, the spectral density of (b) is centered near 1 THz and has a bandwidth which extends to over 4 THz. Emission of freely propagating few-cycle THz pulses from sub-picosecond current waveforms forms the basis for most emitters found in THz-TDS's.

2.3.1 Surface Emission from III-V Semiconductors

Upon excitation by an ultrafast laser, III-V semiconductors emit few-cycle THz pulses [1, 3]. At the origin of this well-studied phenomena is mid-band Fermi

Level pinning at the semiconductor surface that occurs due to surface-defect-state assisted recombination [1, 3]. Subsequently, majority carriers are depleted within approximately 100 - 300 nm of the surface. The exact mechanism responsible for THz emission depends on the electronic properties of the material.

In wide-bandgap III-V's, such as GaAs and InP (bandgap = 1.43 eV and 1.34 eV, respectively), the bending of conduction and valence bands produces a large built-in electric field at the surface. This field accelerates photoexcited carriers and forms large drift current densities that exist on picosecond timescales (Fig. 2.3) [2, 3, 4]. As the polarity of the built-in electric-field changes with substrate doping, the polarity of the emitted THz pulse from n-type and p-type materials is opposite [3].

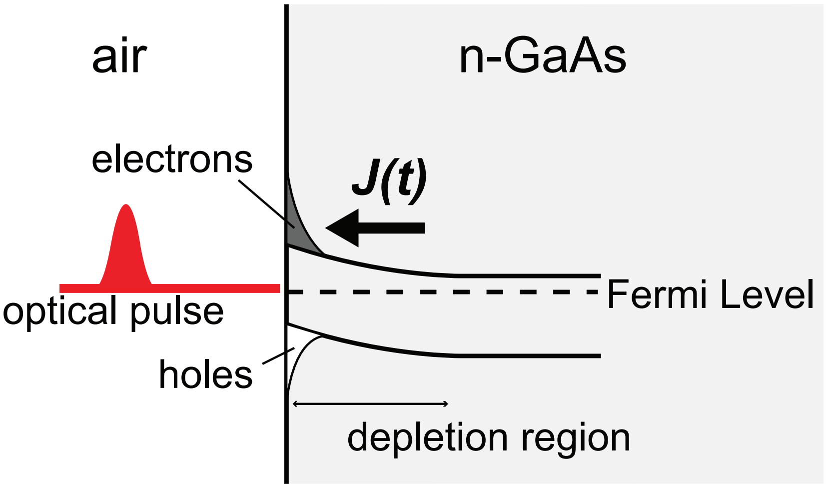

Figure 2.3: Surface emission of few-cycle THz pulses from wide-bandgap III-V semiconductors. The primary emission mechanism is the generation of sub-picosecond drift currents from the large built-in surface field.

In narrow-bandgap III-V's, such as InAs and InSb (bandgap ≈ 0.3 eV and 0.1 eV, respectively), the electric field from band-banding is relatively small and THz emission is predominantly caused by sub-picosecond diffusion currents

[3, 5, 6]. The 1D diffusion current for electrons, $\mathbf{J}_{e_{diff}}$, and holes, $\mathbf{J}_{h_{diff}}$, in a semiconductor is given by the following expression,

$$\mathbf{J}_{e_{diff}} = \mu_e k_B T \frac{\partial n(x)}{\partial x} \mathbf{J}_{h_{diff}} = \mu_h k_B T \frac{\partial p(x)}{\partial x} \tag{2.2}$$

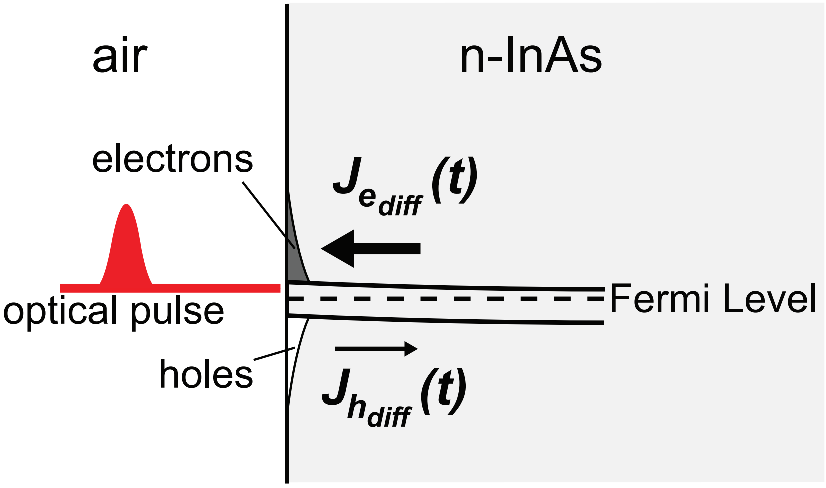

Figure 2.4: Surface emission of few-cycle THz pulses from narrow-bandgap III-V semiconductors. The primary emission mechanism is the generation of sub-picosecond diffusion currents.

where μ_e and μ_h are the electron and hole mobilities, respectively. In InAs these mobilities differ vastly. μ_e = 30,000 $\text{cm}^2/\text{V}\cdot\text{s}$ whereas μ_h = 240 $\text{cm}^2/\text{V}\cdot\text{s}$. Additionally, because the photon energy of a Ti:Sapphire laser pulse is substantially larger than the bandgap of InAs, photoexcitation leads to the generation of a sharp gradient of electrons and holes near the surface. These resulting total diffusion current density $\mathbf{J} = \mathbf{J}_{\text{e}_{\text{diff}}} + \mathbf{J}_{\text{h}_{\text{diff}}} \approx \mathbf{J}_{\text{e}_{\text{diff}}}$ is dominated by the electron diffusion current due to the large electron mobility. Several studies of THz emission from the surface of both n-type and p-type InAs have been conducted. In contrast with emission from wide-bandgap III-V's, the polarity of the emitted THz pulse does not depend on the type of substrate doping [3].

The brightest THz surface emitter is p-type InAs lightly-doped less than 10^{16} cm^{-3} [5]. Lightly doped semiconductors have a larger depletion depth and can therefore support larger photogenerated currents [5, 6]. Unfortunately, it is very challenging to find samples with this level of p-type doping and the InAs samples used in this work were n-type with a doping level of 5×10^{16} cm^{-3}. The measured THz electric-field scaled linearly with optical excitation power up to 1 W.

Practically speaking, THz-TDS's with emitters based on surface emission are the simplest to build. The generation mechanism does not require special phase-matching, precise alignment, or any microfabrication. Moreover, the generated THz pulse propagates co-linearly with the reflected ultrafast laser beam which aids with alignment of free space THz optics. Optical pump pulses should be TM-polarized to exploit Brewster's Angle and should be focused tightly on the emitter. It is, however, important not to focus the optical beam too tightly to avoid damaging the emitter at high excitation fluences. A major setback of surface emission is its low efficiency. Because current dipole generated in the emitter is oriented perpendicular to the surface, most of the THz radiation remains trapped in the substrate by total internal reflection. Excitation powers exceeding 1W are typically needed for this type of emitter.

2.3.2 Photoconductive Emitters

Ultrafast picosecond photoconductive (PC) switches, known as Auston Switches, have been used to generate few-cycle pulses of THz radiation since the mid 1970's [7, 8, 9, 10, 11]. These devices consist of a pair of electrically biased metallic striplines fabricated on a semi-insulating substrate. An ultrafast laser pulse is used to optically excite electron-hole pairs which are then accelerated by the applied external electric field. A schematic of the THz PC emitter used in this work is shown in Fig. 2.5. Separation of the photogenerated carriers generates a space-charge density which then screens the bias field on a sub-picosecond timescale [12, 13]. The emitted THz radiation is almost entirely polarized in the direction of the time-dependent current dipole (perpendicular to the transmission lines) and only a minor component of the emitted field is due to the propagation of sub-picosecond current pulses on the transmission lines themselves.

In typical configurations, these emitters are capable of producing THz pulses with bandwidths from 0.1 - 4 THz, although THz bandwidths exceeding 6 THz from emitters pumped by sub-30fs optical pulses have been demonstrated. The amplitude signal-to-noise-ratio (SNR, defined as the peak THz field amplitude divided by the noise floor) from these PC emitters can be 15,000:1. Such high SNR's are achievable even at excitation powers 100 times less than that needed for surface generation in III-V's. Unlike in surface generation, the current surge in a PC emitter is parallel to the facets of the emitter chip and thereby outcouples to free space much more efficiency.

The PC emitters used in this work were fabricated on 3 inch diameter, 625 μm thick SI-GaAs wafers (>10 MΩ-cm) manufactured by Freiberger Compound Materials. First, the wafer was coated with LOR-5A lift-off photoresist and then SPR220-3 photoresist. The striplines were patterned in the resist using an ABM contact photolithography tool. Next, the resist was developed in MIF-300 for 3 minutes. to achieve a 2μm undercut of the SPR. 50 nm of Ti and 450 nm of Au

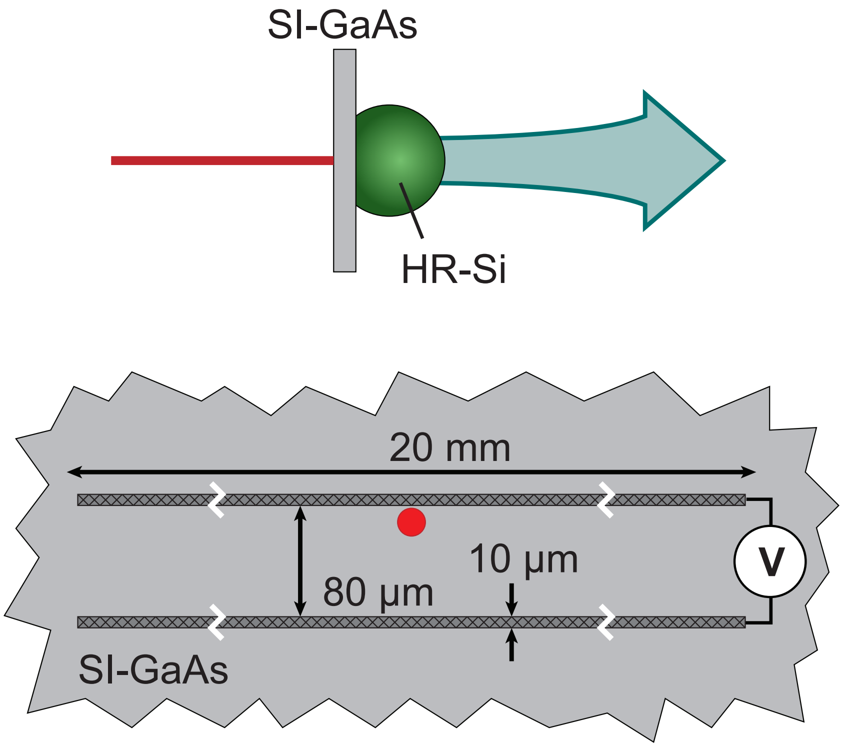

Figure 2.5: A schematic of a THz photoconductive emitter. The emitter is fabricated on a semi-insulating GaAs substrate and consists of Ti/Au striplines separated by 80 μm. A 6.2 mm high-resistivity Si hyperhemispherical lens was butt-coupled to the back of the PC emitter to improve the collimation and out-coupling efficiency of the emitted THz radiation.

were deposited at a rate of 0.15 nm/s using the CHA Mark 50 electron beam evaporator in "Lift-Off Mode." The metal was then lifted-off overnight in 1165 solvent. The details of this process are given in Table 2.2.

The striplines consisted of a pair of 10 μm wide and 20 mm long lines separated by 40, 80, and 160 μm (Fig. 2.5). The effect of stripline geometry on THz-TDS performance is discussed below. Following fabrication, the wafer was diced into 22 mm x 10 mm die that each contained six PC emitters. In some instances, a 90 nm Si_3N_4 anti-reflection coating was deposited on the chips using the IPE plasma-enhance chemical vapor deposition tool. The reflectivity of

Table 2.2: The major steps in the fabrication of photoconductive emitters. This processes is very similar to that used to fabricate photoconductive receivers with two exceptions: (1) thinner SPR955-1.2 was used in place of SPR220-3 (2) Ti/Al was deposited instead of Ti/Au.

Stripline Fabrication Process	
1. LOR-5A spin	45 s @ 3000 RPM
2. LOR bake	5 min @ 180 C
2. SPR220-3 spin	45 s @ 4000 RPM
3. solvent bake	90 s @ 115 C
4. exposure	4 s
5. post exposure bake	90 s @ 115 C
6. develop	3 min
7. metallization	Ti/Au 50 nm/450 nm
8. lift-off	overnight in 1165

this coating was < 5% at 780 nm. Each chip was then glued to the backside of a printed circuit board and then wire-bonded. A picture of a completed and mounted THz PC emitter is shown in Fig. 2.6.

The emitter chips were then placed inside a custom set of mounts and positioned at the focus of a 6″ focal length parabolic mirror. To improve the collimation and collection efficiency of the THz pulse, a 6.2 mm tall high-resistivity (> 10 KΩ-cm) hyperhemispherical Si lens was butt-coupled to the back of the chip. The steps required to align the PC emitter will be discussed later.

In general, there exists a tradeoff between field amplitude and pulse bandwidth from PC emitters. Larger dipoles should produce higher SNR pulses with reduced bandwidth. However, the 80 μm dipoles yielded the best overall per-

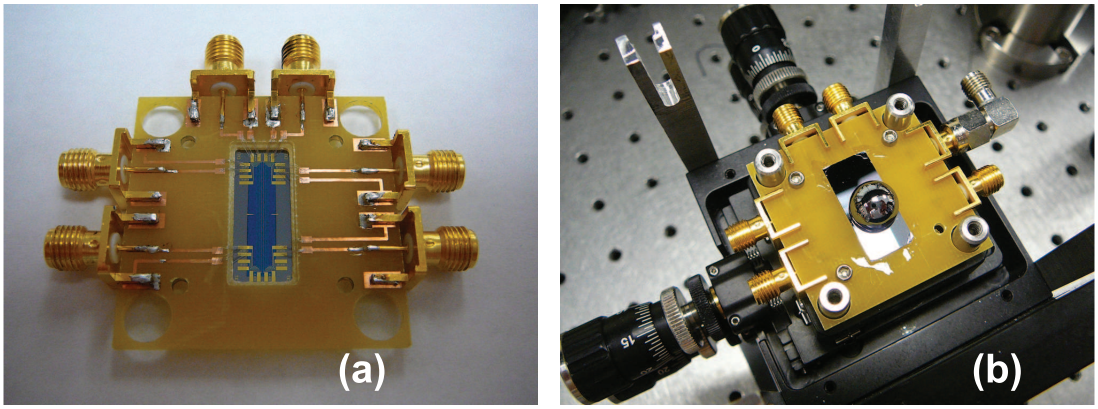

Figure 2.6: (a) A photograph of a PC emitter chip containing 6 stripline THz emitters mounted and wirebonded to a PCB board. The SMA coaxial connectors are used to apply the external bias. The blue strip in the middle of the chip is a 90 nm Si_3N_4 AR coating. (b) The emitter chip in a custom optical mount. A HR-Si hyperhemispherical lens is butt-coupled to the back of the chip.

formance as determined experimentally. This may be due to detector limitations as well as the limitations in the performance of the free-space THz optics and Si lenses at higher frequencies. Additionally, it should be noted that the THz field amplitude and bandwidth depend strongly on the size and position of the optical focus on the PC dipole.

Figure 2.7 (a) and (b) show the PC transmitter current and the maximum THz electric-field amplitude versus optical excitation power for different emitter bias voltages, respectively. The transmitter current and THz field have similar functional dependence on optical power and emitter bias, although the current is slightly more linear at low excitation powers. Both exhibit a sharp ”turn-on” that occurs at decreased optical powers as the electrical bias is increased. This feature is believed to be due to the rapid increase of thermionic current over the Ti/GaAs Schottky barrier with an increased in the photogenerated carrier density. At larger biases, the Schottky barrier is lowered and ”turn-on” happens at smaller carrier densities. For 80 μm dipoles, the maximum emitter photocurrent, optical power, and bias voltage were 0.9 mA, 7.5 mW, and 90 V respectively. These parameters were selected to maximize the emitted THz field and the longevity of the emitter while minimizing the effects of pump beam fluctuations and misalignment on emitter performance.

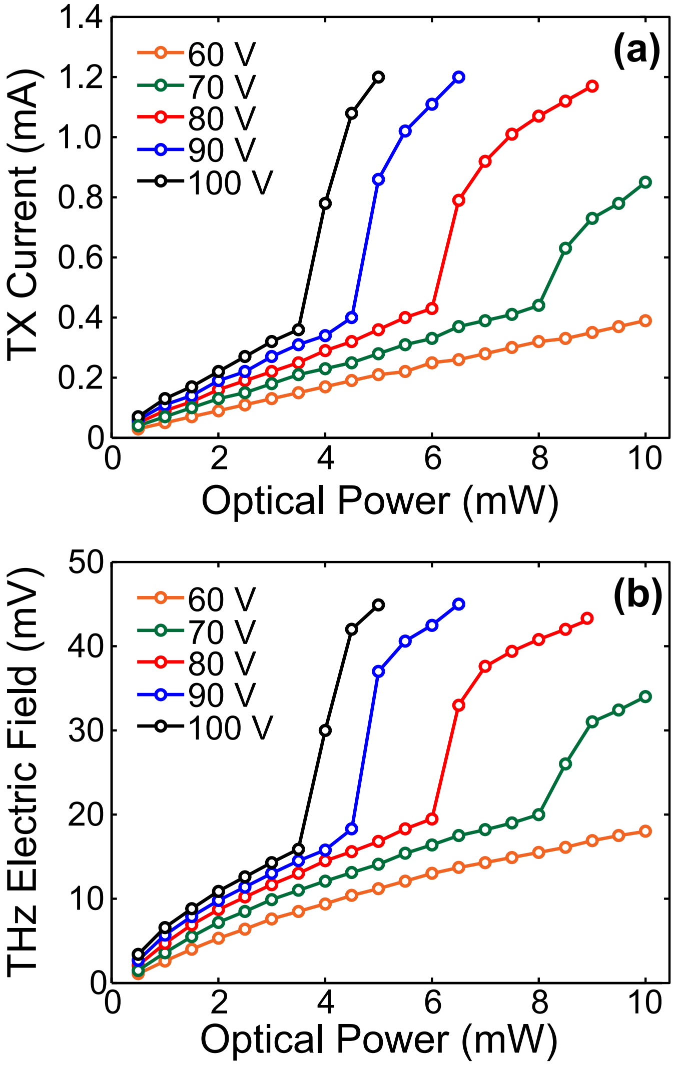

Figure 2.7: Current in the PC emitter (a) and detected THz electric field (b) versus optical excitation power for different applied biases. The sharp "turn-on" transient is most likely due to increasing thermionic current over the Ti/GaAs Schottky barrier.

2.3.3 Nonlinear Emitters

Optical rectification of ultrafast laser pulses in nonlinear media can also be used to generated few-cycle THz pulses. As was previously mentioned, efficient nonlinear generation of THz pulses requires the use of regeneratively amplified optical pulses that have several millijoules of energy and gigawatt peak powers. The spectral components of these pulses mix to generate low-frequency THz harmonics. Nonlinear generation of THz pulses has been demonstrated in several semiconductors [14], including ZnTe [15, 16], $LiNbO_3$ [17, 18, 21] as well as some organic materials such as 4-dimethylamino-Nmethylstilbazolium tosylate (DAST) [19, 20]. Recently, terawatt amplified laser systems have been used to produce extremely high-power THz pulses with energies of several microjoules from tilted phase-front $LiNbO_3$ [21].

2.4 Detectors

In THz Time-Domain Spectrometers, detection is accomplished by measuring the cross-correlation of the incident THz pulse and an ultrafast laser pulse. The detector is optically gated coherently with the arrival of the THz pulse and the THz pulse is sampled at one point in time. The entire THz waveform is resolved by adjusting the delay between it and the optical pulse. Selective gating of the detector only with the arrival of the THz pulse enables very high detection sensitivities, as mentioned previously. The two types of THz-TDS detectors used in this work will be discussed.

2.4.1 Photoconductive Detectors

A photoconductive detector is an optically gated stripline antennae that is externally biased by the incident THz pulse. As can be seen in Fig. 2.8, the geometry of a PC detector is similar to that of an emitter with the addition of a folded dipole between the two striplines. The incident THz pulse is focused on the dipole using a Si lens and drives currents in the detector by accelerating photoexcited carriers. These currents are measured using a lock-in amplifier and are typically several nanoamps at maximum.

The PC receivers were fabricated on a 3” 430 μm thick Silicon-On-Sapphire (SOS) wafer with a 0.5 μm thick Si cap layer. The fabrication process was identical to that used for PC emitters with two exceptions. First, thinner SPR955-1.2 i-line photoresist was spun and exposed on the GCA AutoStep stepper photolithography tool to resolve sub-micron features with sharp corners. Second, 80 nm of Ti and 400 nm of Al were evaporated. Detectors with 5 μm striplines and a 10 μm long dipole (5-10-5) and 2 μm striplines and a 6 μm long dipole (2-6-2) were both fabricated. The larger detectors have smaller bandwidth but greater peak signal level when compared to the smaller detectors.

An additional implantation step was required to reduced carrier lifetime and improve detection bandwidth. Individual chips (each containing six detectors) were commercially dual implanted with O^+ ions at energies of 200 KeV and 100 KeV and a constant dose of 10^{15} cm^2. These defects act as mid-band traps and, at the dose and energies listed above, should reduce the carrier lifetime to < 1 ps. The chips were mounted similar to the emitter chips and placed at the focus of a 6” parabolic mirror. A 6.4 mm tall hyperhemispherical Si lens was butt-coupled to the backside of the chip and the incident optical excitation

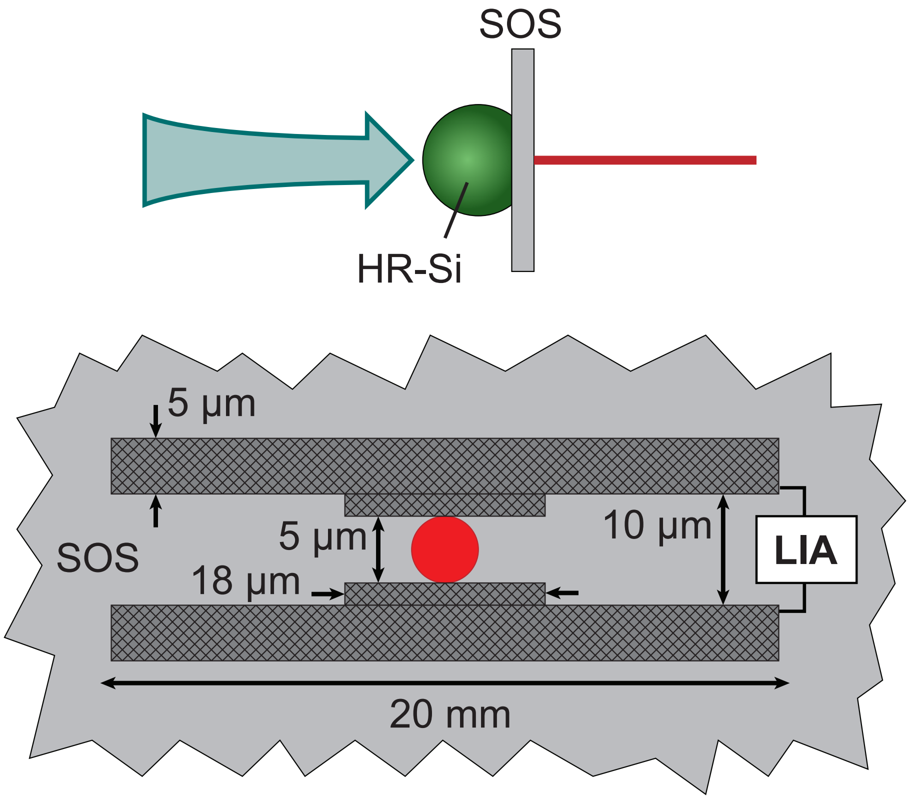

Figure 2.8: A schematic of a THz photoconductive receiver. The receiver is fabricated on a Silicon-on-Sapphire substrate and consists of a Ti/Al folded-dipole with a 5 μm gap for optical excitation. The SOS substrate was intentionally damaged by implantation of O^+ ions to reduce the carrier lifetime to $<$ 1ps and increase the detection bandwidth. A 6.4 mm high-resistivity Si hyperhemispherical lens was butt-coupled to the back of the PC receiver to focus the incident THz pulse on the dipole.

power was 7.5 mW. Figure 2.9 shows an example of THz pulse measured by a 5-10-5 dipole PC receiver. The bandwidth of the detected pulse is limited by the detector geometry. THz bandwidths exceeding 4.5 THz can be achieved by using a smaller 2-6-2 dipole receiver.

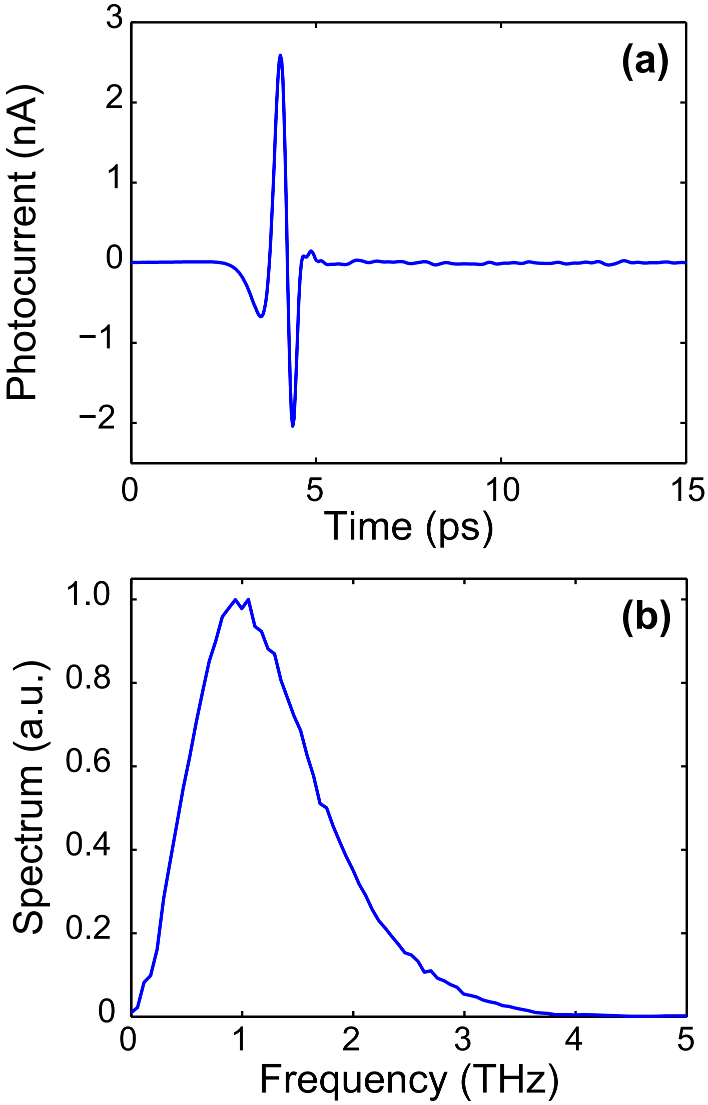

Figure 2.9: The THz electric field and spectrum detected by a 5-10-5 SOS PC receiver. The THz emitter was an SI-GaAs PC switch with an 80 μm gap. The amplitude SNR is 3000:1 and the THz bandwidth exceeds 3 THz. With the same emitter, the detected SNR of a smaller 2-6-2 dipole was reduced to 1000:1, but the bandwidth increased past 4.5 THz.

2.4.2 Nonlinear Detectors

Nonlinear detection of few-cycle THz pulses is based on the electro-optic effect, whereby the THz electric field induces optical birefringence in a nonlinear medium. The induced birefringence produces a phase-shift on a co-propagating optical pulse which is ultimately manifested as a polarization rotation [16, 22, 23, 24, 25, 26]. The nonlinear detectors in this work were based on 1 mm thick $< 110 >$ oriented ZnTe crystals manufactured by eV Products and Nikko Materials. Although other nonlinear media have been used in THz detection [27, 28], ZnTe exhibits the highest responsivity because of a strong nonlinear coefficient, relatively low absorption coefficient from 0.1 - 3 THz, and relatively good phase matching at optical and THz frequencies. The index of refraction of ZnTe is $\approx$3 at 780 nm and is 3.17 - 3.36 from 0.1 - 3 THz [29].

A detailed analysis of the principle of electro optic detection in an arbitrary medium with a zincblende crystalline structure is given in [16]. To achieve maximum sensitivity, the detector was oriented such that the polarization of the THz pulse was parallel to the $< 110 >$ crystalline axis. The polarization of the optical probe pulse was rotated to be parallel to the $< 100 >$ crystalline axis.

Figure 2.10 shows a schematic of a nonlinear THz detector system as well as a photograph of the actual system, respectively. The optical probe pulse is passed through a linear polarizer (extinction ratio >100,000:1) and then co-linearized with the THz pulse using a pellicle beamsplitter. Because the pellicle is substantially thinner than a THz wavelength, its THz transmission is nearly unity. The THz and probe pulses propagate collinearly and through the ZnTe crystal with an adjustable temporal delay. The probe then passes through a $\lambda/4$-waveplate (QWP) and a Wollaston polarizer. Finally, the probe is split based on polarization and measured with balanced Si photodetectors. A detailed analysis of this process is given below.

A pictorial representation of the polarization state of the optical probe as

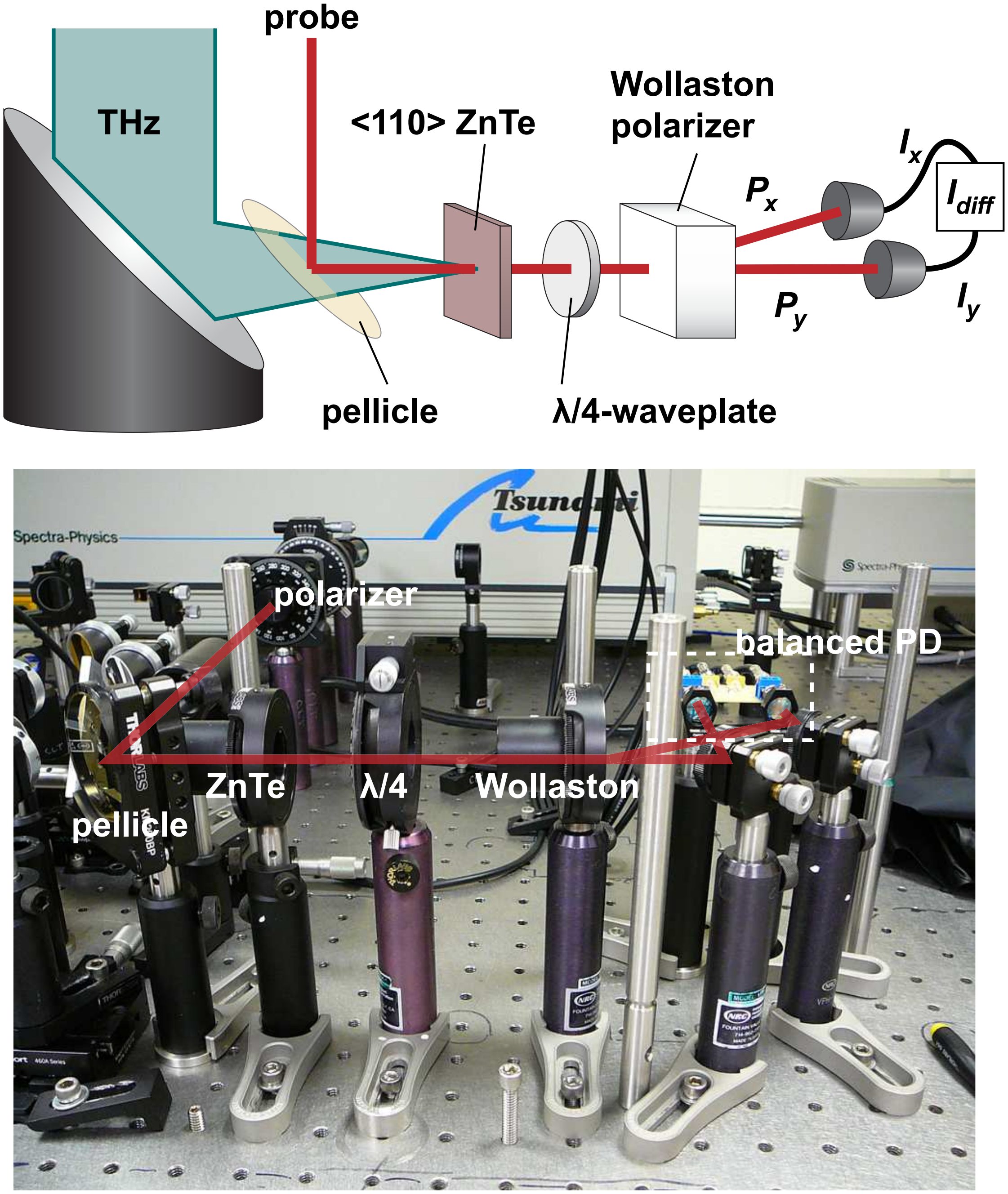

Figure 2.10: A schematic and picture of the nonlinear detection system used in this work for detecting few-cycle THz pulses. The optical probe and THz pulse propagate collinearly through the electro-optic ZnTe crystal. THz-induced birefringence in the ZnTe rotates the polarization of the probe pulse. The differential polarization signal is then measured using balanced photodetectors (see Fig. 2.12).

it propagates through the ZnTe crystal and QWP is shown in Fig. 2.11. For reference, the **xyz** coordinate system is oriented such that the **x**-axis is parallel to the optical table and the probe is propagating in the **z**-direction. Additionally, the $\mathbf{x}'\mathbf{y}'\mathbf{z}$ coordinate system is a $-\pi/4$ rotation of **xyz** around the **z**-axis. After the linear polarizer and before the ZnTe, the polarization of the probe pulse is $\mathbf{y} = \frac{1}{\sqrt{2}}(\mathbf{x}' + \mathbf{y}')$. The THz induced birefringence in ZnTe adds a phase shift ϕ to the probe that is linearly proportional to the amplitude of the incident THz electric field, $\mathbf{E}_{THz}$. $\phi = \xi \mathbf{E}_{THz}$, where ξ is a constant that is based upon material parameters and optical wavelength [16]. After the ZnTe crystal, the probe is elliptically polarized in a polarization state that can be expressed as $\frac{1}{\sqrt{2}}(\mathbf{x}' + e^{j\phi}\mathbf{y}')$.

Next, the probe passes through a QWP that is rotated such that its slow axis is parallel to $\mathbf{y}'$. The probe polarization is $\frac{1}{\sqrt{2}}(\mathbf{x}' + je^{j\phi}\mathbf{y}')$.

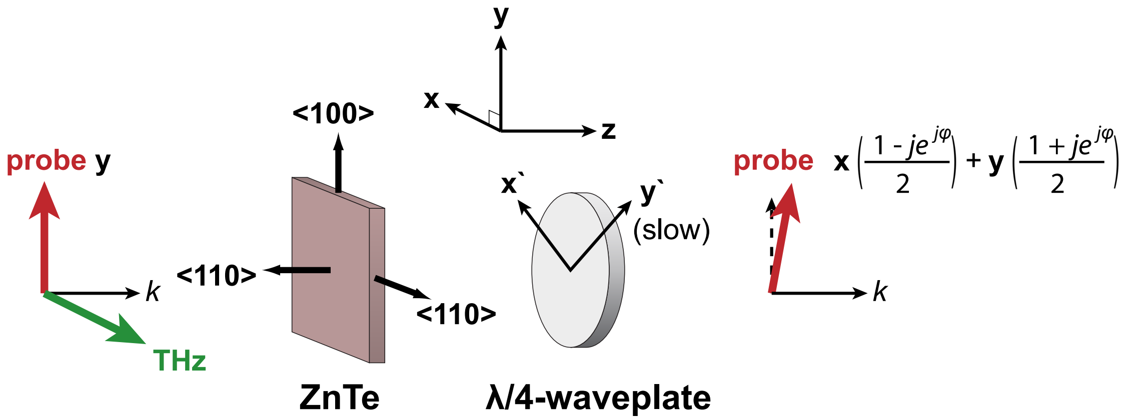

Figure 2.11: The polarization state of the optical probe pulse after it passes through the ZnTe crystal and QWP in the nonlinear THz detector. The probe polarization has been rotated (with respect to the **xy** coordinate system) due to THz-induced birefringence in the ZnTe crystal.

Finally, a Wollaston polarization-selective projects the probe polarization into the **xy** coordinate system and physical separates the beam into its **x** and **y** polarization components. The difference in the power of each beam, $\mathbf{P}_{\Delta} = \mathbf{P}_x - \mathbf{P}_y$, is proportional to

$$\mathbf{P}_\Delta \propto \sin(\phi) \tag{2.3}$$

When the polarization of the THz pulse becomes negative, $\mathbf{P}_\Delta$ also changes sign. In typical THz-TDS systems, $\phi \approx 10^{-3}$, and Eq. 2.3 may be approximated by

$$P_\Delta \propto \phi \tag{2.4}$$

The QWP is essential because it "biases" the detector such that its response is linearly proportional to the amplitude of the incident THz electric field [25]. In the absence of the QWP, $\mathbf{P}_\Delta \propto \cos(\phi)$ which is constant for small ϕ.

A schematic and photograph of the balanced photodetector circuit used in the THz detector are shown in Fig. 2.12. The circuit contained two Hamamatsu S2386-44K Si photodiodes biased at 10 V, two AVX CB027D0104JBA 0.1 μF surface-mount capacitors, and two Vishay TNPW08051K00BEEN 1 KΩ surface-mount resistors. Following the Wollaston, each polarized beam was focused onto a photodiode and the power in each beam was 10 μW. The differential current, $\mathbf{I}_\Delta \propto \mathbf{P}_\Delta$, was input to a Stanford Research SR570 current preamplifier and then to a lock-in amplifier. With the THz pulse blocked, I_{diff} should ideally be 0 if the detector is perfectly balanced. In practice, the common-mode rejection ratio, defined as $\mathbf{I}_x/\mathbf{I}_\Delta$, of 10,000:1 could be achieved by carefully rotating the QWP to adjust $\mathbf{P}_x$ and $\mathbf{P}_y$ and by adjusting the external DC bias of each photodetector.

An example THz waveform measured using the nonlinear detection scheme is shown in Fig. 2.13. The THz bandwidth of the pulse is limited to 3 THz be-

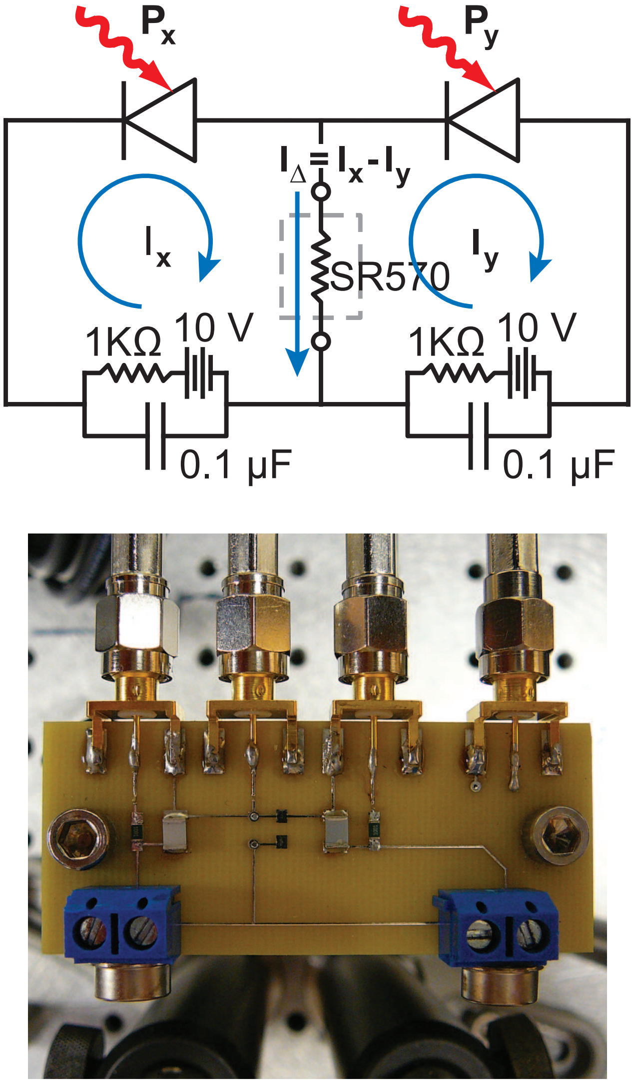

Figure 2.12: A schematic and picture of the balanced photodetector circuit used for nonlinear detection of THz pulses. The output of the circuit, $\mathbf{I}_{\Delta}$ is sent into a lock-in amplifier. The circuit had a maximum common-mode rejection ratio of 10,000:1.

cause of strong acoustic phonon absorption in ZnTe [29]. However, THz-TDS's with very thin ZnTe detectors that exhibit better phase-matching and lower absorption have demonstrated detection bandwidths over 40 THz [26, 30]. ZnTe also has an acoustic phonon band at 1.6 THz [29].

Nonlinear THz detectors suffer from a fundamental problem that ultimately

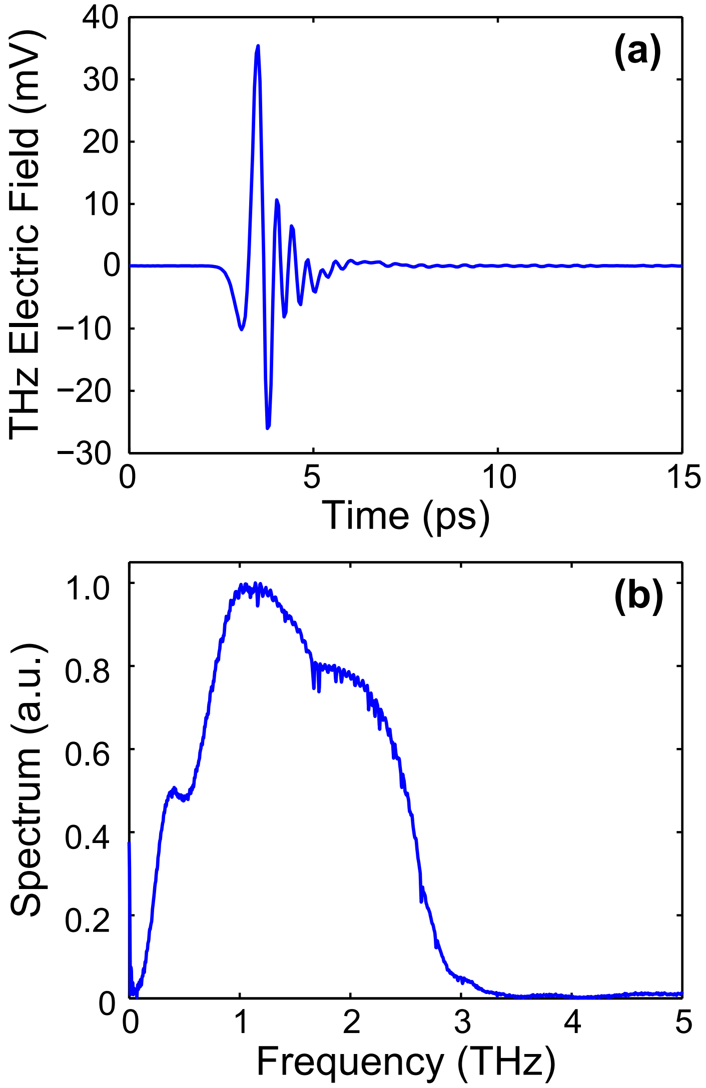

Figure 2.13: The THz electric field and spectrum detected by a nonlinear electro-optic detector based on 1 mm thick $< 110 >$ ZnTe crystal. The THz emitter was an SI-GaAs PC switch with an 80 μm gap. The amplitude SNR is 500:1 and the THz spectrum drops sharply near 3 THz due to phonon absorption the detector. To avoid the effects of multiple internal reflections, a polished 10 mm MgO cube was butt-coupled to the back of the ZnTe.

limits the maximum frequency resolution of the THz-TDS. The round-trip propagation time in a 1 mm thick ZnTe crystal (index $\approx$ 3.1) is 20 ps and, subsequently, long scans of the THz waveform in time will contain strong "baby" pulses separated by this interval as a result of multiple internal reflections. These pulses introduce deep Fabry-Perot fringes into the pulse spectrum at a frequency spacing equal to the inverse round-trip time inside the ZnTe crystal that are not easily removed. Therefore, the frequency resolution of a THz-TDS based on nonlinear detection in a 1 mm thick ZnTe crystal is limited to 50 GHz. To eliminate these Fabry-Perot fringes, a 10 mm MgO (optically transparent) crystal was butt-coupled to the back of the ZnTe. Because MgO is nearly indexed matched to ZnTe at THz frequencies, reflections of the THz pulse from the MgO-ZnTe interface were negligible and the frequency resolution of the THz-TDS was increased to 4.5 GHz.

2.5 Aligning a THz-TDS

The first major step in systematically aligning a THz-TDS is the alignment of the parabolic mirrors. Once the beam path is established and the basic spectrometer geometry is determined, the laser focusing optics for the THz emitter and detector should be installed. Because the THz pulse will propagate (approximately) co-linearly with the laser excitation pulse, the laser beam path and spot size is an excellent reproduction of the future THz pulse path. The parabolic mirror for the emitter (detector) should therefore be aligned with the laser focused tightly at the expected position of the THz emitter (detector).

Alignment of a THz surface emitter and a nonlinear detector is relatively straightforward because, as previously mentioned, the visible laser beam that reflects off or propagates through these components can be used as a reference for the THz path. While the path of the incident laser pulse and generated THz pulse are also co-linear in a PC emitter, the entire laser pulse is absorbed by the emitter substrate and can no longer be used as a visible reference. Therefore, PC emitters must be aligned in two steps. First, the PC dipole is aligned to the incident laser pulse by focusing the laser spot tightly on the dipole and looking at the image of the dipole in the reflected beam with an IR scope. It is important to note that the incident laser beam should not be moved after the parabolic mirrors have been aligned to it. Monitoring the photocurrent from the external DC voltage supply also helps when aligning the dipole. Next, the hyperhemispherical Si lens must be aligned to the dipole (in essence, to the laser pulse). To do this, a collimated 1550 nm amplified spontaneous emission (ASE) source co-linearized with the laser beam can be used. The Si lens should be adjusted such that the ASE radiation transmitted through the entire emitter setup strikes the parabolic mirror in the center. An analogous process is used to align PC detectors.

2.6 Optical-Pump THz-Probe Spectroscopy

With the addition of an optical pump pulse, as shown in Fig. 2.14, the capability of a THz-TDS system can be augmented to realize the time-resolved spectroscopy of ultrafast phenomena. This technique, known as optical-pump THz-probe (OPTP) spectroscopy , utilizes few-cycle THz pulses from a TDS to coherently probe the THz frequency dynamics of an optically excited sample. Unlike most traditional single-color or multi-color optical-pump optical-probe spectroscopy, OPTP allows for the study of the low-frequency collective excitations of a sample. These collective excitations may correspond to rotation or oscillation of the conformation modes of DNA or protein, or the free-carrier response of a bulk semiconductor or graphene sheet. Additionally, because the THz electric field is measured directly in the time-domain, the time-resolved refractive index and conductivity of a sample can be extracted.

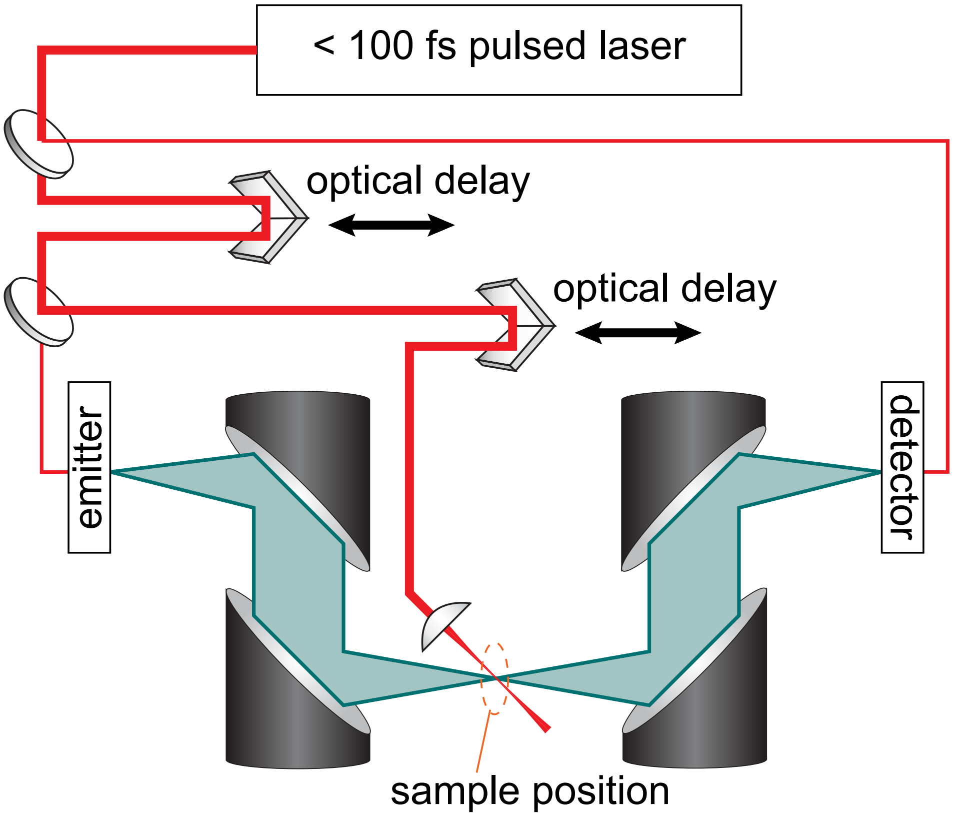

Figure 2.14: A schematic of an optical-pump THz-probe experimental setup. This setup is similar to that in Fig. 2.1 with the addition of an optical pump path. Samples under test are placed at the focus of the parabolic mirrors, excited optically, and then probed with a THz pulse. This system enables experimental measurement of time-dependent complex conductivity as well the time-evolution of the entire frequency-dependent complex conductivity.

As can be seen in Fig. 2.14, OPTP THz-TDS systems have two optical delay stages and subsequently two different temporal delays. The first optical delay controls the temporal delay between the THz pulse and the optical probe pulse that is incident upon the detector. This delay is fundamental to every THz-

TDS. The second optical delay is used to adjust the temporal delay between the THz pulse and the optical pump pulse incident on the specimen under study. Both the optical pump and THz probe pulses are simultaneously chopped and the lock-in amplifier is referenced to the sum (or difference) of these chopping frequencies. A photograph of the actual experimental OPTP setup is shown in 2.15.

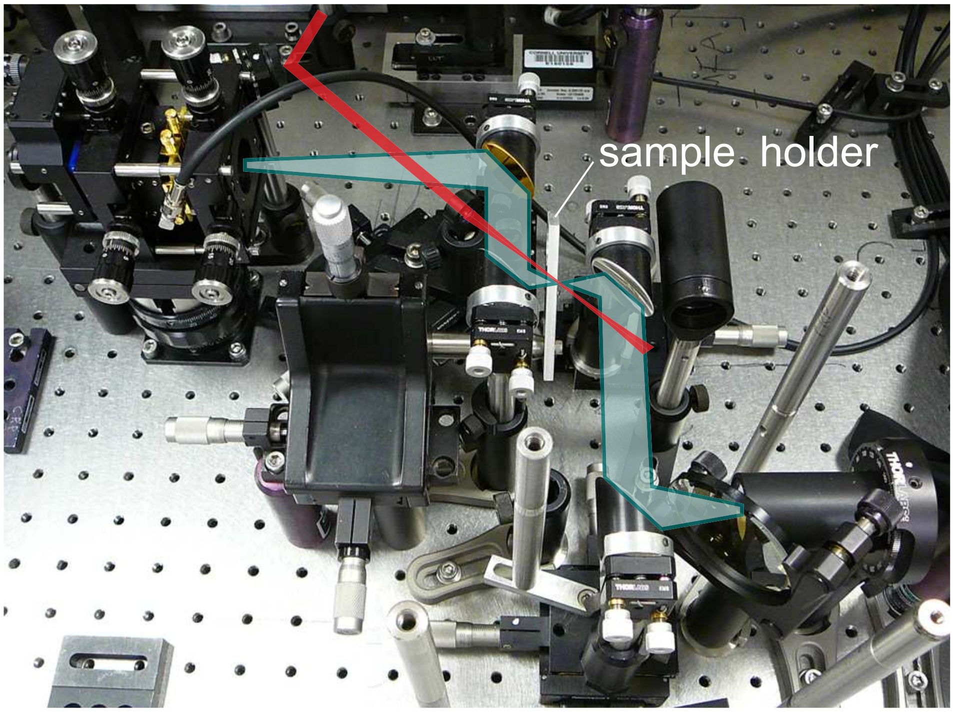

Figure 2.15: A photograph of the actual optical-pump THz-probe experimental setup.

There are two different ways of performing OPTP spectroscopy. To measure the differential THz transmission of a sample (ultimately the time-dependent complex conductivity), the first optical delay is adjusted to maximize the THz signal and is then held constant while the second optical delay is scanned. Measurements of this type will, for example, produce a decaying-exponential plot of the lifetime of photogenerated electron-hole pairs in a semiconductor. This type of measurement technique has been used to directly measure the free-carrier lifetime in radiation-damaged SOS [31] and the relaxation and recombination dynamics in epitaxial graphene [32].

To measure the entire time-evolution of the frequency-dependent complex conductivity, the temporal delay between the optical-pump and THz-probe pulses is held fixed and the entire THz waveform is measured in time by scanning the first delay. The optical-pump THz-probe delay is then incremented and the waveform is scanned again. The time-evolution of the conductivity spectrum can then be extracted by studying the time-evolution of the Fourier transform of each THz pulse at each optical-pump THz-probe delay. The time-dependent complex conductivity spectrum of GaAs nanowires [33] and Ge nanowires [34] was measured using this OPTP technique.

The measured OPTP signal is proportional to the overlap of the THz probe and optical pump on the sample as well as the number of excited carriers. It is therefore beneficial to match the focal size of each pulse while focusing both very tightly. However, the 6″ focal length parabolic mirrors typically found in THz-TDS only focus the THz pulse to a FWHM spot diameter of ≈ 1 mm. Most OPTP systems utilize high pulse energy regeneratively amplified laser systems to achieve very high photogenerated carrier densities even with these large optical focal spots. The measurements presented in the latter chapters of this work, however, were exclusively performed using a standard, un-amplified Ti:Sapphire oscillator. To accommodate for low pulse energy, the standard 6″ focal length parabolic mirrors were replaced with 1″ focal length mirrors and the THz spot size was reduced by nearly 30. The focal spot of the optical pump pulse was then reduced and the excitation density was subsequently increased by nearly the same factor. Of course, the introduction of smaller optics made the entire OPTP system more compact and difficult to align (Fig. 2.15).

CHAPTER 3

AIR-CORE METAL INTEGRATED TERAHERTZ PHOTONICS

3.1 Introduction

Integrated THz photonic components are important for performing THz spectroscopy of vibrational modes in biological and chemical molecules [67, 68, 69], realizing lab-on-a-chip detection platforms with high-sensitivity [35, 36, 37], studying THz nonlinearities, and developing compact sources of coherent THz radiation [38, 39]. Although several types of passive THz waveguides and resonators have been experimentally demonstrated [40, 41, 42, 43, 44], they have typically been fabricated using bulk micromachining techniques and are not suitable for on-chip integration. This chapter will present the first experimental measurements of novel integrated THz air-core metallic photonic components. In addition, the fabrication techniques used for building these devices will be discussed. This chapter will primarily focus on results for square microcavity resonators side-coupled to metal waveguides and present measurements of the cavity quality factors resulting from external coupling and intrinsic cavity loss for different resonator sizes.

3.2 Aperture-Coupled Microcavity Resonators

Figure 3.1 shows a schematic of a square THz microcavity resonator, with side d, coupled to a waveguide via an aperture with width w and thickness t. At near-IR wavelengths, evanescent-field coupling is commonly used to excite dielectric microcavities via waveguides [46]. In these devices, however, THz radiation is aperture-coupled to the air-core resonators. The **y**-polarized electric field propagates in the TE_{10} waveguide mode whose spatial field profile is given by,

$$\mathbf{E} = \mathbf{y}E_o \sin\left(\frac{\pi}{l}x\right)e^{j\beta z} \tag{3.1}$$

where

$$\beta = \sqrt{\left(\frac{2\pi}{\lambda}\right)^2 - \left(\frac{\pi}{l}\right)^2} \tag{3.2}$$

and λ is the free-space wavelength. This mode excites the fundamental TE_{101} mode of the microcavity with the (approximate) spatial profile of,

$$\mathbf{E} = \mathbf{y}E_o \sin\left(\frac{\pi}{d}x\right)\sin\left(\frac{\pi}{d}z\right) \tag{3.3}$$

In a lossless and uncoupled metallic resonator, the resonance frequency of the TE_{101} mode is equal to,

$$\omega_o = \frac{c}{2\pi}\frac{c}{d\sqrt{2}} \tag{3.4}$$

Because the spatial profiles of the TE_{10} mode and TE_{101} mode are constant in the y-direction, the electromagnetic fields in these modes can be simulated using a two-dimensional Finite-Difference Time-Domain (2D-FDTD) method. The simulated resonant THz electric field in the structure is shown in Fig. 3.1.

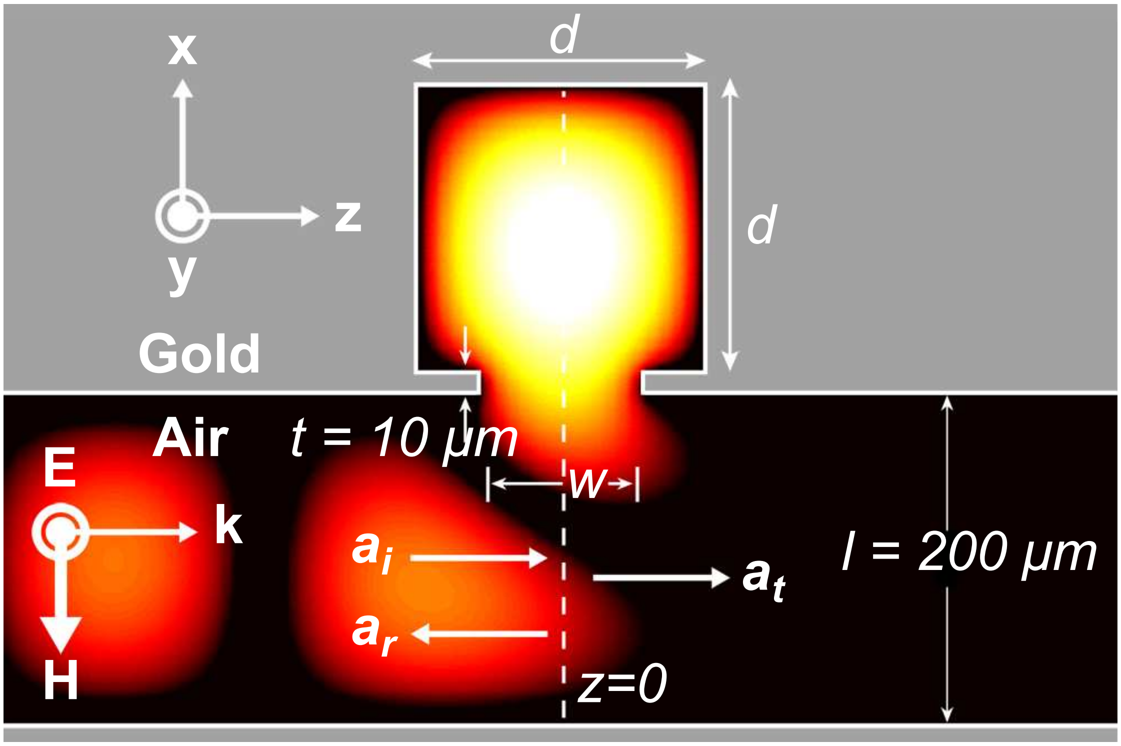

Figure 3.1: Schematic of a THz microcavity resonator side-coupled to a metal waveguide overlayed with the simulated THz electric field from 2D-FDTD. The square resonator has side *d* and the coupling aperture has width *w* and thickness *t*. The THz electric field polarized in $\hat{y}$-direction and the waveguide is 200 μm wide.

3.3 Fabrication

The THz resonators and waveguides under test were fabricated from two heavily doped ($N_A = 10^{20}$ cm^{-3}) 3″ Si wafers that were patterned and bonded together. Heavily doped wafers were selected so that any THz radiation that was coupled to the substrate instead of the waveguide would be significantly attenuated and would not interfere with measurements. First, the side-coupled resonators and waveguides were defined on one wafer in SPR220-3 (2 μm) photoresist using standard photolithography techniques detailed in Table 3.1. The exposure was performed on an ABM contact lithography tool with the near-UV (405 - 365 nm) mirrors installed. A post-exposure bake was performed to activate the resist, improve development, and reduce side-wall roughness. After developing the resist in MIF300, the patterned resist was hardbaked in a convection oven at 90 C for 60 min to improve etch selectivity and durability. The wafer was then etched 150 μm using a Unaxis 770 deep reactive-ion etcher (RIE). The 150 μm etch depth established the waveguide, resonator, and aperture height (dimension in the **y**-direction). An SEM image of a typical etched structure is shown in Fig. 3.3. As can be seen, the coupling aperture was etched anisotropically and was undercut by 20 μm. To achieve maximum verticality, the Unaxis etcher utilizes the Bosch etching processes whereby a two-step passivation and isotropic SF_6 etch cycle is repeated several hundred times. Subsequently, the waveguide sidewalls had 150 nm scallops following the etch, as can be seen in Fig. 3.4. To help reduce scattering and propagation loss from this sidewall roughness, the etched wafer was oxidized with 1 μm of thermal oxide and then dipped in 49% HF acid.

Next, both the etched and blank Si wafers were oxidized with 750 nm of thermal oxide. After oxidation, 50 nm of Ti and 400 nm of Au were conformally deposited on the wafers using a CHA Mark 50 electron beam evaporator in ”Planetary Mode.” The thickness of the Au layer was chosen to be greater than five electromagnetic skin-depths (~80 nm at THz frequencies [47]). Following evaporation, both wafers were immediately pressed together to form a temporary bond. The wafer stack was then permanently bonded under vacuum on an EV501 wafer bonder at a temperature of 350 C and a pressure of 1.5 MPa for 45 minutes [49]. The oxide layer between the Si substrate and metal acted as crucial diffusion barrier that prevented Si atoms from diffusing into the Au layers and disrupting the bond. The bond fidelity was tested by dicing a sample

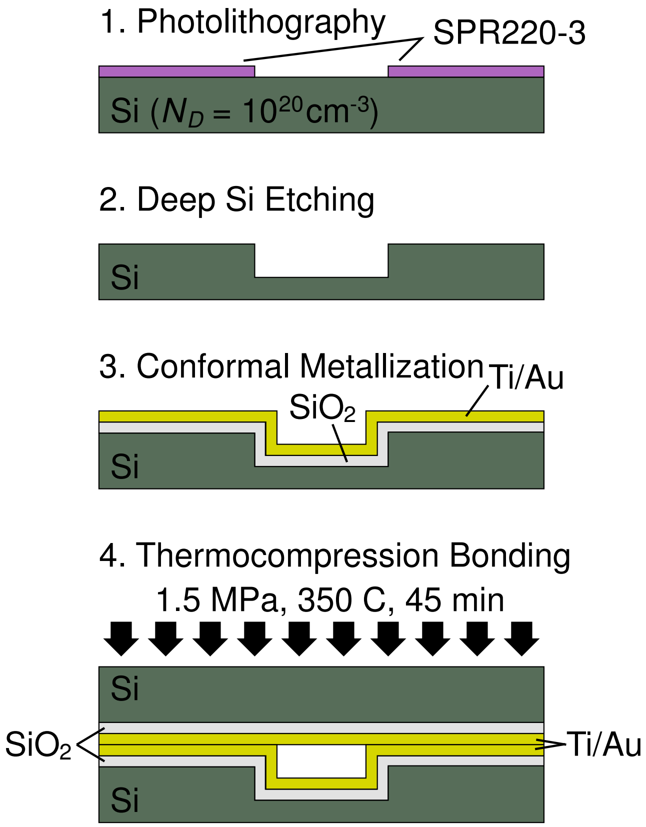

Figure 3.2: The four major fabrication steps: (1) Photolithography; (2) Deep Si Bosch etching; (3) Thermal oxidation and Ti/Au conformal metallization; and, (4) Thermocompression bonding.

wafer into 2 mm x 2 mm squares on the wafer saw. Despite the excessive stress exerted by the saw, over 99% of the diced pieces remained bonded. Finally, the completed devices were diced 7 mm long and the facets were polished until optically smooth at THz frequencies. Figure 3.5 displays one facet of an air-core rectangular metal waveguide.

Table 3.1: The photolithography steps required to define air-core waveguides and resonant cavities in a silicon.

Photolithography Process	
1. P10 prime	30 s @ 3000 RPM
2. spin	45 s @ 4000 RPM
3. solvent bake	90 s @ 115 C
4. exposure	4 s
5. post exposure bake	90 s @ 115 C
6. develop	90 s
7. hard bake	60 min @ 90 C

3.4 Experimental Measurement

Terahertz measurements of the waveguides were conducted using a purged THz Time-Domain Spectrometer (THz-TDS) with a SI-GaAs photoconductive transmitter and a SOS photoconductive receiver [44] arranged in a two-parabolic-mirror U configuration (Fig. 3.6(a)). The spectrometer was pumped by an ultrafast Ti:Sapphire laser and the power incident upon both the transmitter and receiver was 10 mW. With a lock-in amplifier time constant of 100 ms, the power spectral dynamic range of the experiments was 10^6. Chips containing several waveguides were clamped vertically in a metal mount that was connected to a three-axis linear stage. Terahertz radiation from the THz-TDS was coupled into the devices using 6.2 mm tall high-resistivity Si hyperhemispherical lenses butt-coupled to each waveguide facet. The entire coupling setup was placed equidistant bewteen the two 6″ focal length parabolic mirrors. Figure 3.6 shows a picture of the coupling setup. Multiple 80 ps long scans of each device were performed to ensure the repeatability of spectral features resulting from

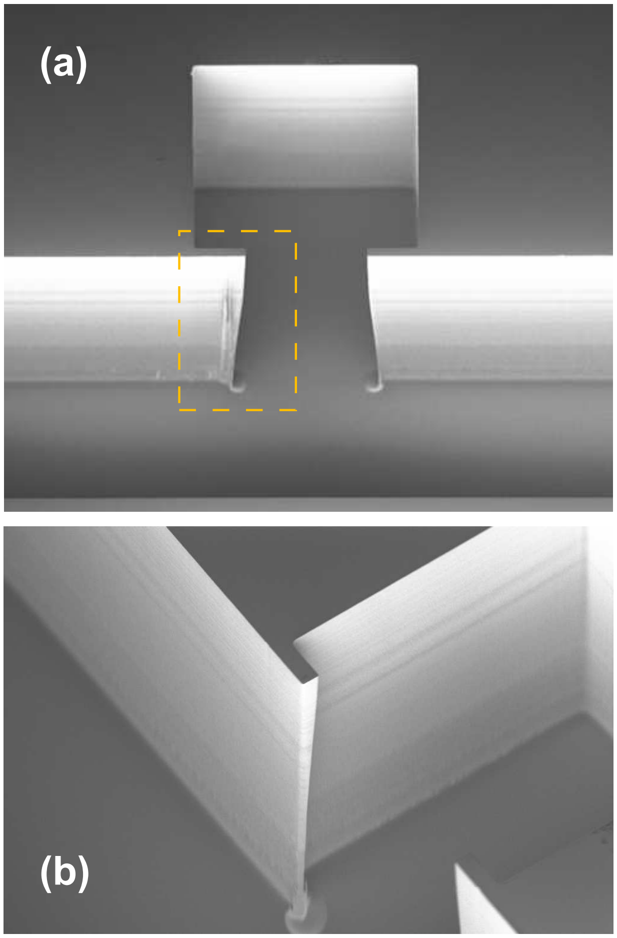

Figure 3.3: (a) SEM of a fabricated waveguide-coupled THz microcavity resonator. (b) Zoomed in view of the coupling aperture (dashed box in (a)). The coupling aperture is undercut due to anisotropic etching.

the excitation of a microcavity.

Three square resonators with sides d = 175 μm, 150 μm, and 125 μm coupled to 200 μm wide waveguides via apertures of average widths w = 110 μm and 100 μm and thicknesses t = 10 μm were measured using the THz-TDS. As an example, the time-domain THz electric field after propagation through a waveguide coupled to a resonator (d = 125 μm and w = 100 μm) is shown in Fig. 3.7. Ringing in the waveform due to waveguide dispersion as well as the frequency-

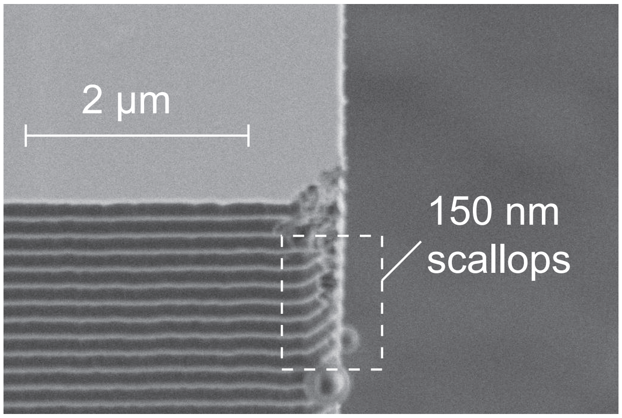

Figure 3.4: Post-etch sidewall roughness due to scalloping from the Bosch deep-Si etch process.

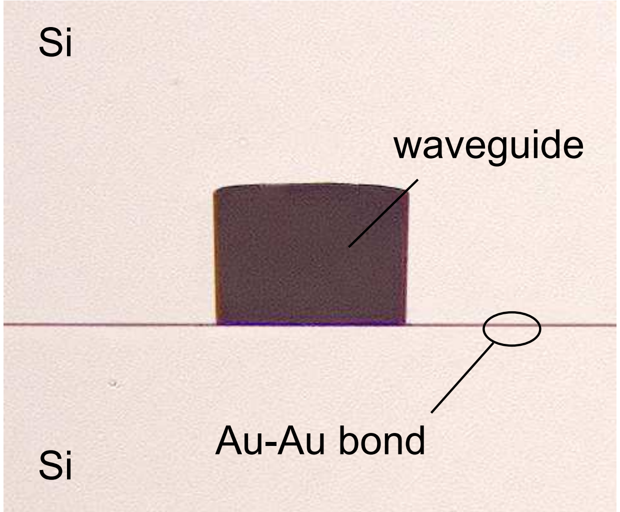

Figure 3.5: Photograph of a polished waveguide facet which shows an air-core metal waveguide and Au-Au bond.

dependent transmission of the resonator extends past 60 ps. The time-domain waveform of the pulse through the waveguide has been shifted in time to eliminate the 107 ps propagation delay from the Si lenses. Figure 3.8 displays the measured power transmitted through the device. The transmission spectrum exhibits a narrow feature at 1.331 THz that corresponds to excitation of the resonant cavity. As can be seen in Fig. 3.7(a), the measured waveguide cutoff fre-

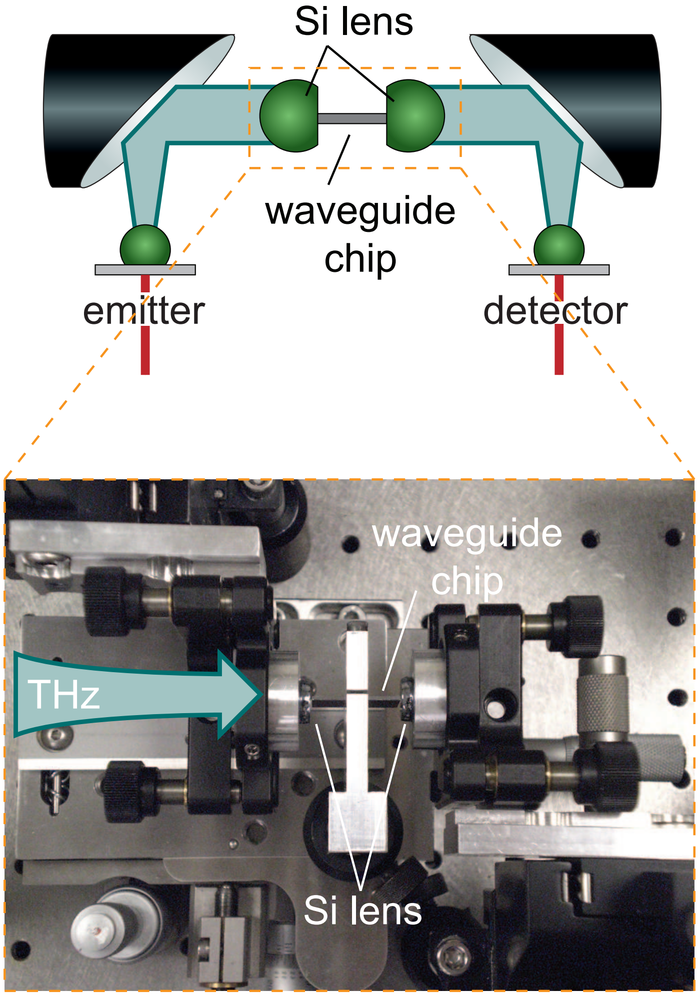

Figure 3.6: The coupling setup used to measure the THz response of the microcavity resonators and waveguides. The waveguide chip mounted between the two Si lenses contains several integrated waveguides.

quency is 0.75 THz. This is in excellent agreement with theoretical predictions. The strong oscillations in the spectrum that begin at 2.15 THz are characteristic of significant excitation of higher order waveguide modes [40].

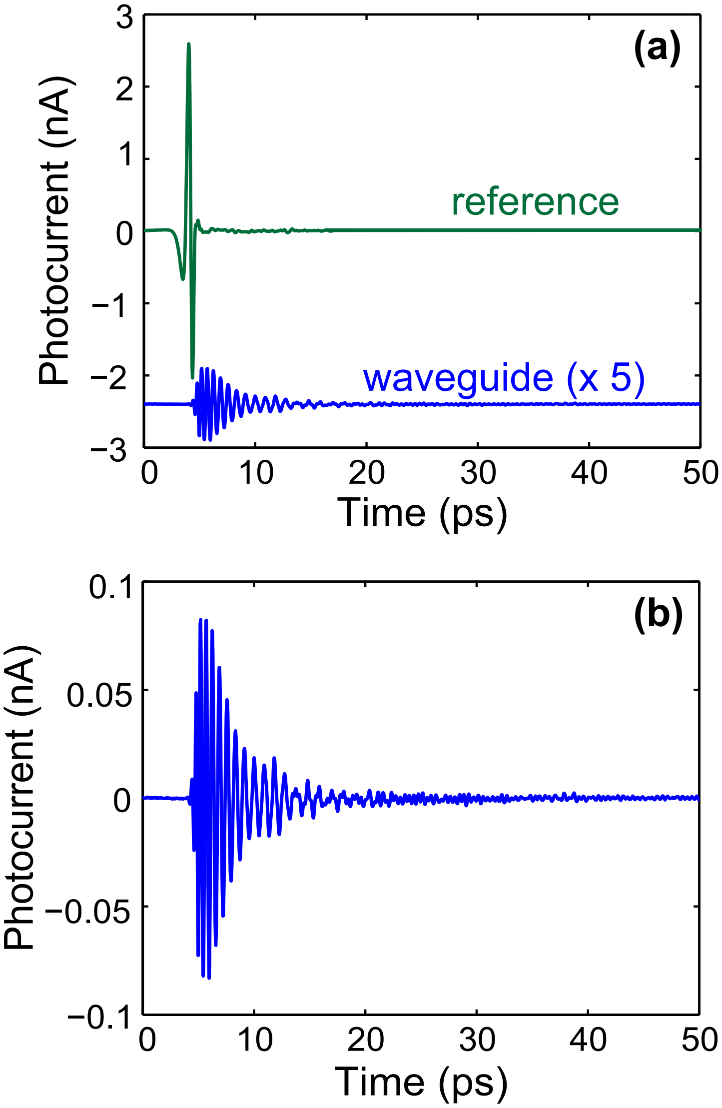

Figure 3.7: (a) The measured THz time-domain electric field waveform of after propagation through free space (green) and the waveguide-coupled resonator structure (d = 125 μm, w = 100 μm) (blue, scaled 5 times and shifted in time). (b) The actual measured waveform after propagation through the waveguide device. Oscillations in the time-domain waveform are from waveguide dispersion and excitation of the resonant cavity.

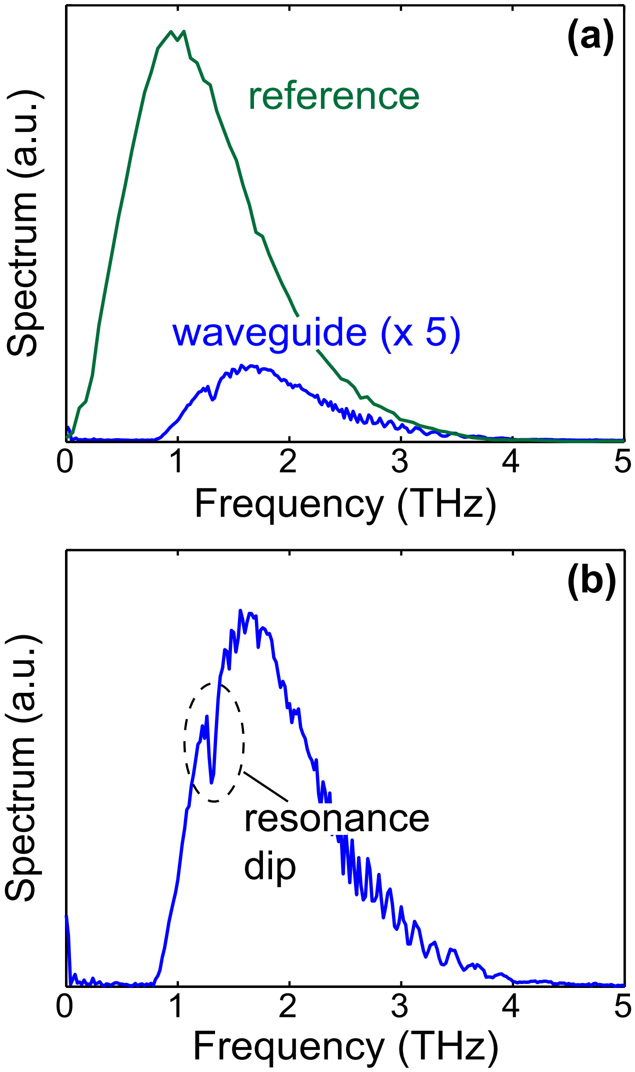

Figure 3.8: (a) The measured THz time-domain amplitude spectrum after propagation through free space (green) and the waveguide-coupled resonator structure (d = 125 μm, w = 100 μm) (blue, scaled 5 times). (b) The actual measured amplitude spectrum after propagation through the waveguide device. The spectrum exhibits a resonance dip near 1.33 THz which is evidence of excitation of the resonant cavity mode. In (a), spectral components below the waveguide cutoff frequency (0.75 THz) do not propagate. Fringes in the spectrum are due to interference of higher-order waveguide modes.

3.5 Theoretical Analysis

Near the resonant frequency, the evolution of the electric field, b, inside of a resonator coupled to a single-mode waveguide can be described by coupled mode theory [50].

$$\frac{db}{dt} = \left(j - \frac{1}{2Q_L} - \frac{1}{2Q_E}\right)\omega_o b + \sqrt{\frac{\omega_o}{2Q_E}} a_i \tag{3.5}$$

In Eq. 3.5, ω_o is the resonance frequency, Q_E and Q_L are the cavity quality factors related to external coupling and intrinsic cavity loss, respectively, and a_i is the incident waveguide field (Fig. 3.1) normalized such that its squared magnitude equals the incident power. The transmitted field is a_t, where $a_t = a_i - b\sqrt{\omega_o/2Q_E}$ [50]. After combining this equation with the time-harmonic solution to Eq. 3.5, the expression obtained for the frequency-dependent power transmission of the coupled waveguide-resonator system, $T(\omega)$, is

$$T(\omega) = \left|\frac{a_t}{a_i}\right|^2 = \left|1 - \frac{1/Q_E}{1/Q_E + 1/Q_L - 2j(1 - \omega/\omega_0)}\right|^2 \tag{3.6}$$

This expression has a Lorentzian shape and is applicable for frequencies close to ω_o. From Eq. 3.6, it can be seen that the power transmission at resonance is reduced from unity and is exactly zero for lossless cavities ($Q_L = \infty$). This occurs because the electromagnetic radiation coupled from a lossless resonator back into the waveguide in the forward direction interferes completely destructively with the incident radiation, a_i.

Figure 3.9, Fig. 3.10, and Fig. 3.11 show the extracted transmission resonances for resonators with d = 175, 150, and 125 μm, respectively. As can be

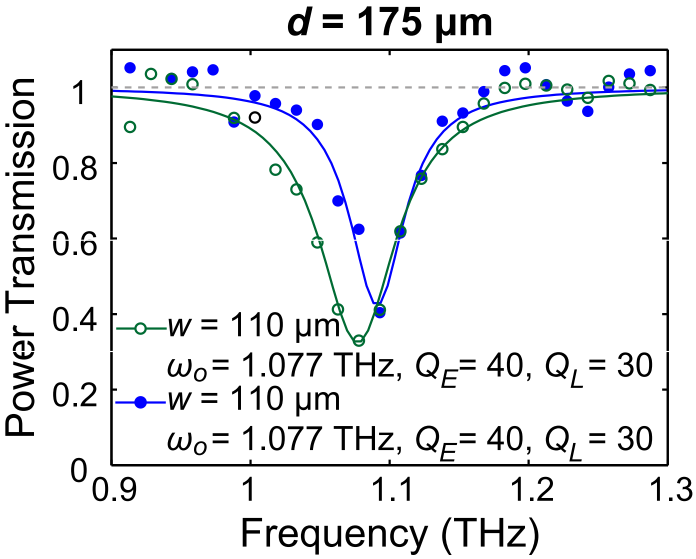

Figure 3.9: Microcavity transmission spectra for resonators with d = 175 μm and average w = 110 μm (open circles) and 100 μm (open squares). Measured values Q_E are between 40 and 90 and a fitting error less than 10% is expected.

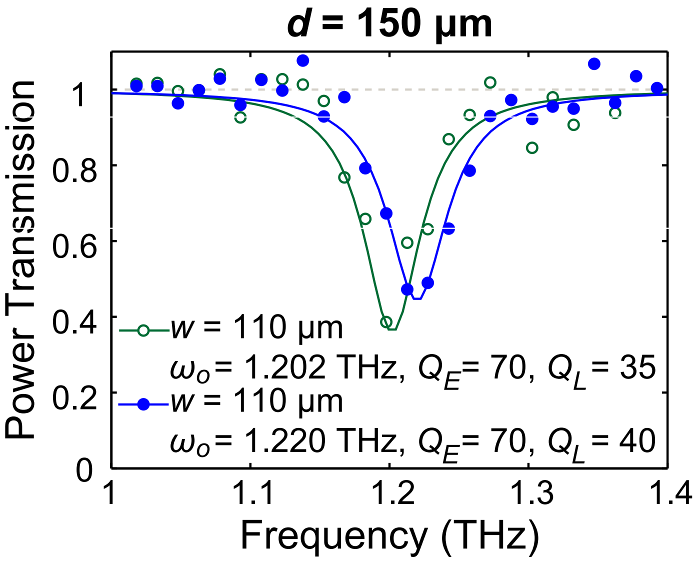

Figure 3.10: Microcavity transmission spectra for a resonator with d = 150 μm and average w = 110 μm (open circles) and 100 μm (closed circles).

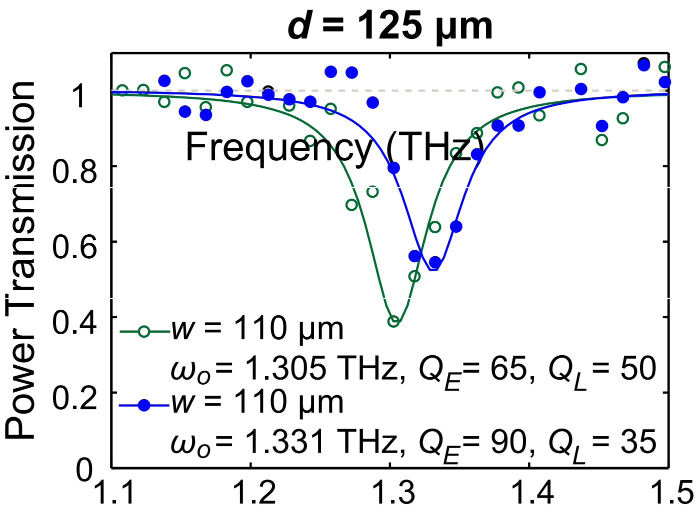

Figure 3.11: Microcavity transmission spectra for a resonator with d = 125 μm and average w = 110 μm (open circles) and 100 μm (closed circles).

seen, the microcavities affect the measured THz-TDS spectra only in a narrow frequency range near resonance. To extract the microcavity transmission spectra, the measured THz-TDS spectra with resonances removed were fitted with fifth-order polynomials near the resonance frequencies and the total THz-TDS spectra were then normalized with these polynomials. Figure 4 shows the transmission spectra of different cavities obtained in this way. The Lorentzian expression in Eq. 3.6 was fitted to the measured microcavity transmission spectra to obtain the values of ω_o, Q_E, and Q_L, which are included in Fig. 3.9, Fig. 3.10, and Fig. 3.11. It can be seen that the measured transmission spectra is well described by a Lorentzian near the resonance frequency. The values of Q_E and Q_L changed by less than 10% when a third-order polynomial was used to extract the transmission spectra.

The increase of ω_o and Q_E with decrease in w matches closely the trends predicted by 2D-FDTD simulations. As the aperture width is reduced, the resonator becomes increasingly decoupled from the waveguide and the coupling quality factor increases. Table 3.2 shows the measured data and simulated results obtained from 2D-FDTD for $d = 175$ μm and w averaged to account for the 20 μm etch undercut mentioned previously. The small discrepancies between these measured and FDTD values can be attributed to nonidealities in the structure dimensions and sidewall verticality that cannot be modeled by two-dimensional simulations. Similar agreement exists between FDTD results and experimental data for the other resonators shown in Fig. 3.10 and Fig. 3.11.

Table 3.2: Measured and simulated values of ω_o, Q_E, and Q_L for $d = 175$ μm. Good agreement between experimental and 2D-FDTD results exists for ω_o and Q_E. Large discrepancy in Q_L may be due to imperfect metallization and defects in the Au-Au bond.

Measured				
d (μm)	w (μm)	ω_o (THz)	Q_E	Q_L
175	100	1.077	40	30
175	90	1.091	65	35

2D-FDTD				
d (μm)	w (μm)	ω_o (THz)	Q_E	Q_L
175	110	1.117	55	370
175	100	1.132	80	354

As can be seen in Table 3.2, the measured and simulated values of Q_L differ significantly. Using a conductivity of 38×10^6 S/m for Au at 1 THz [47, 48], the calculated values of Q_L are between 291 and 370 for all the cavity geometries studied in this work. These values are significantly larger than the measured values of 30 to 40 presented in Fig. 3.9. This disagreement may partially be due to the reduced conductivity of evaporated Au at THz frequencies [51], but is more likely attributable to defects in the Au-Au bond. Imperfections in the bond could lead to a contact resistance of several Ohms that would add in series with the resistance due to Ohmic losses in the cavity sidewalls ($\sim 0.4\ \Omega$) (Fig. 3.4). The calculated values of Q_L agree well with the measured values if a bond resistance of $\sim 3\ \Omega$ is assumed.

From Eq. 3.5, the estimated enhancement of the square-magnitude of the peak THz electric field in the microcavity resonator to that in the waveguide is between 8 and 18 for all of the structures in this work. Achieving strong field enhancement in integrated structures would therefore require THz microcavities with small intrinsic cavity losses. Such structures would be well suited for narrow-band sensing applications, developing integrated sources of THz radiation, and studying THz nonlinearities.

CHAPTER 4

TERAHERTZ SPECTROSCOPY OF BIOLOGICAL MOLECULES USING NOVEL MICROFLUIDIC DEVICES

4.1 Introduction

Important biomolecules, including proteins, RNA, and DNA have vibrational modes with frequencies in the 0.1 THz - 5 THz range [52, 53, 54, 55, 56, 57, 58, 59, 60, 61]. Consequently, THz electromagnetic radiation can be used to probe, detect, and identify biomolecules. The THz absorption spectra of biomolecules reflect the low frequency vibrational modes corresponding to collective molecular oscillations, relative motion of molecular subdomains, and, specifically in DNA molecules, twisting and deformation of the double-helix structure [52, 53, 54]. Compared to higher frequency Raman modes, the low frequency vibrational modes in DNA are extremely sensitive to composition and topology, and reflect features specific to specific DNA sequences. In addition, because these vibrational modes have frequencies in the THz range, the complex refractive index a biomolecule is sensitive to its primary, secondary and tertiary molecular structure as well as to its specific conformational state. Therefore, THz spectroscopy can also be used for the detection and identification of biomolecular compositions and conformations.

Several studies of biomolecules in the THz frequency range have been conducted [55, 56, 57, 58, 59, 60, 61]. Due to strong water absorption at THz frequencies, these studies have typically been limited to dry or partially hydrated specimens. In [55], THz time-domain spectroscopy (THz-TDS) was performed on dried films of biomolecules that were up to 7.5 mm thick. The use of thick dry films also helps to increase the measurement SNR by increasing the interaction length between the THz radiation and the biological specimen. In [56, 57], THz-TDS of hydrated liquid-phase biomolecules prepared in gel films was performed. Studies of the THz absorption of biomolecules in large volume aqueous solutions were conducted in [58], but these experiments required the use of a high-power free electron laser. Unfortunately, such high-power THz sources are very large, expensive, and are not readily available. Recently, integrated spectroscopy systems based upon microstrip waveguides have been proposed and demonstrated in [59, 60, 61]. However, the performance of these devices suffers from the limited bandwidth of microstrip components.

The techniques utilized in most of these measurements are fundamentally limited in many ways and do not facilitate the development of integrated THz sensing platforms. Instead, it is advantageous to perform the spectroscopy of biological molecules should be performed in liquid phase – whether it be in buffered aqueous solution, in blood, or other liquid buffers – in compact microfluidic devices for several reasons: (1) microfluidic chips can facilitate interchanging biological specimen andreacting biological specimen with chemicals or other agents in real-time; (2) the dimensions of microfluidic channels can be designed to facilitate the use of low-power THz-TDS systems by avoiding excess water absorption and can enable the spectroscopy of picomole quantities of biomolecules; and, (3) microfluidic channels can easily be integrated with photonic elements and other devices to realize multifunctional spectroscopy platforms with high sensitivity. A schematic of such an integrated THz sensing platform based on microfluidic channels is shown in Fig. 4.1. The realization of these devices requires materials that have low loss and dispersion from optical to THz frequencies, are mechanically stable and chemically inert, and are compatible with microfabrication.

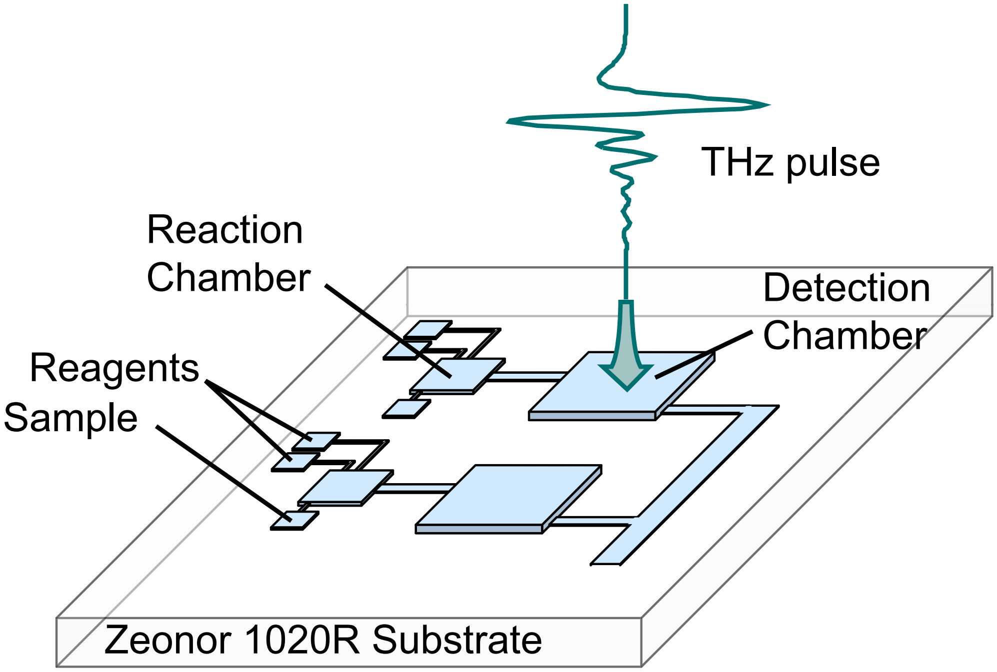

Figure 4.1: A system for on-chip THz sensing. The device contains arrays of sample and reagent inputs, reaction chambers, and detection chambers for THz as well as optical and IR spectroscopy.

4.2 Materials for Microfluidics

4.2.1 PDMS and Zeonor 1020R

Microfluidic channels are commonly fabricated from polydimethylsiloxane elastomer (PDMS), which is a flexible, heat-curable polymer that has high transmission at optical wavelengths. Due to its high water content, PDMS exhibits large absorption at THz frequencies and is therefore unsuitable for use in THz devices. Additionally, PDMS microfluidic channels are formed by bonding an embossed PDMS slab with a glass or Quartz substrate. This would further increase THz losses. Fortunately, there exists a much more promising material from which THz devices can be constructed. This material, known as Zeonor 1020R, is a mechanically rigid polymer that exhibits high transmission from UV to Far-IR wavelengths, has significantly lower water content than PDMS [62], and is resistant to most solvents and corrosives. Zeonor 1020R is produced by the Zeon Corporation is, at the time of this work, was available in 2 mm thick, clear plaques.

4.2.2 The Complex Index of PDMS and Zeonor 1020R

The dispersion and optical absorption coefficients of both Zeonor 1020R and PDMS from 0.25 THz - 3 THz were measured using the THz-TDS based on a <100> n-InAs emitter and a 1 mm <110> ZnTe electro-optic detector described earlier. Because both the Zeonor and PDMS slabs were thick and exhibited only broad spectral features, the temporal length of the spectrometer scan was limited so as to avoid etalon effects caused by multiple internal reflections. The index of refraction and absorption coefficient of Zeonor and PDMS were then extracted from the measured transmission data using Fresnel's equation for the frequency-dependent amplitude transmission through a dielectric slab, t, without multiple internal reflections

$$t = \frac{E_m(\omega)}{E_r(\omega)} = \frac{4n}{(1+n)^2} e^{i\frac{\omega}{c}(n-1)d} \tag{4.1}$$

In Eq. 4.1, $E_m(\omega)$ is the measured THz spectrum of the pulse after propagation through the slab, $E_r(\omega)$ is the THz spectrum of the reference pulse, d is the slab thickness, and n is the complex index of refraction of the slab. The absorption coefficients of Zeonor and PDMS calculated from the extracted complex indices of refraction are shown in Fig. 4.2.

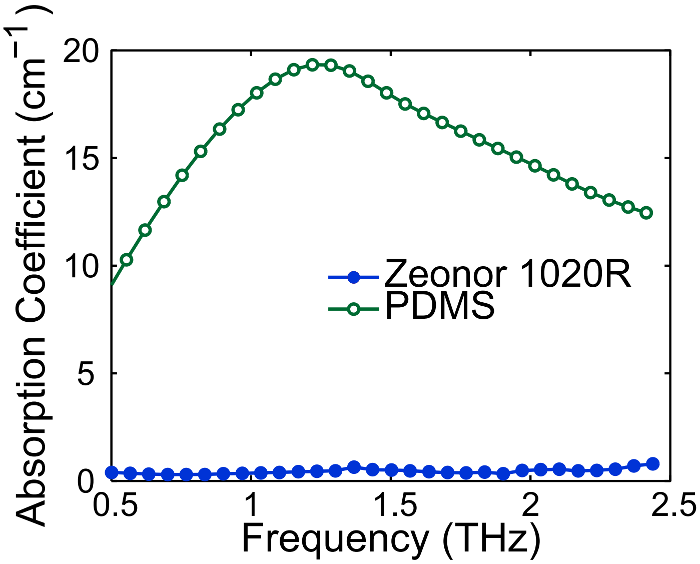

Figure 4.2: The measured absorption coefficient of Zeonor 1020R and PDMS. Zeonor has a nearly constant index of 1.518 (not shown) and an absorption coefficient <1 cm^{-1} at THz frequencies, which is 10-20 times smaller than that of PDMS.

Zeonor 1020R has a measured index of approximately 1.518 and an absorption coefficient <1 cm^{-1} from 0.5 THz - 2.5 THz. The low absorption of Zeonor over a large frequency range makes it very well suited for use in THz spectroscopy.

4.3 Fabrication

The fabrication of microfluidic devices out of Zeonor 1020R involvesdutilizing a multi-step hot-embossing technique that has been described in [63, 64]. A pictorial representation of the major steps involved is shown in Fig. 4.3 (a) and (b). The template for embossing the channel was constructed from a 4″ Si wafer.

First, a 5 mm wide x 25 mm long channel was defined on the wafer in SPR220-3 (2 μm) photoresist using standard photolithography techniques detailed in Table 3.1. The exposure was performed on an ABM contact lithography tool with the near-UV (405 - 365 nm) mirrors installed. A post-exposure bake was performed to activate the resist, improve development, and reduce side-wall roughness. After developing the resist in MIF300, the patterned resist was hard-baked in a convection oven at 90 C for 60 min to improve etch selectivity and durability.

The channel was then etched into the Si wafer using a Unaxis 770 deep reactive-ion etcher (RIE). The exposed wafer surrounding the channel was etched 95 μm deep thereby leaving the channel defined as a mesa in the center of the wafer.

To form the channel, a 14.5 cm^2 square Zeonor piece was embossed with the Si wafer template on a hotpress at a temperature of 115 C and a pressure of 2.55 MPa. The piece was then cooled under load until its temperature was below the glass transition temperature (102 C [62]). Fluid input and output ports were then defined using a small end-mill and any excess Zeonor was removed with a knife. Next, the embossed piece and a blank 14.5 cm^2 Zeonor square were soaked in an ethanol/decalin (80/20) solution for 30 s and 1 min, respectively. The pieces were then rinsed in ethanol, dried and bonded on a hotpress at a temperature of 65 C and a pressure of 1.6 MPa for 40 min to form the channel. A picture of a typical completed device is shown in Fig. 4.3 (b). Finally, syringe needles were glued over the input (output) ports to facilitate the injection (removal) of solutions into (out of) the device.

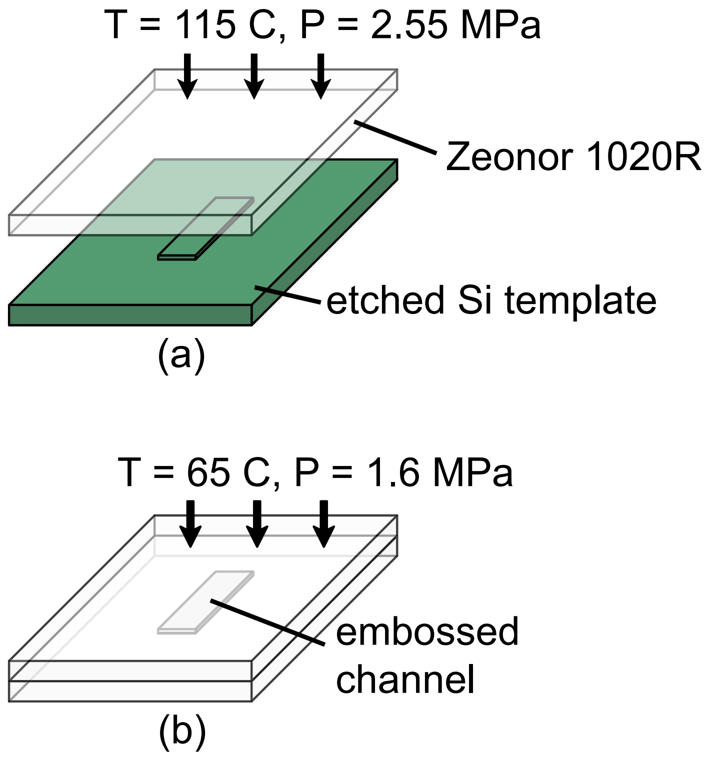

Figure 4.3: Fabrication of the microfluidic devices used in this work. The microfluidic channel is defined between two slabs of Zeonor 1020R using a hot embossing technique and is irradiated normally by pulses from a THz-TDS. The final channel depth was 95 μm.

4.4 The Absorption Spectrum of Bovine Serum Albumin

4.4.1 Overview of BSA

The absorption spectrum of the protein bovine serum albumin (BSA) at THz frequencies was measured using Zeonor microfluidic channels. BSA is a well studied proteins, is readily available, and is inexpensive. It is a polypeptide chain consisting of 583 amino acids [65] with a sequence homology similar to Human Serum Albumin [58]. BSA has a heart-shaped ellipsoidal geometry [53] with a 54% α-helix and 18% β-sheet structure and has a molecular weight of approximately 66.430 kDa [65]. Importantly, spectroscopy of BSA at THz frequencies has also previously been reported [55, 58, 59].

Aqueous solutions of globulin-free and fatty-acid-free lyophilized BSA powder (Sigma-Aldrich A0281 Batch #075K7545) were prepared in a 0.05 M phosphate buffer (pH = 7.5) at concentrations of 101 mg/mL (pH = 7.0), 200 mg/mL (pH = 6.9), and 305 mg/mL (pH = 6.9) as measured by 279 nm UV spectrophotometry. At these high concentrations, the uncertainty in the measurement of the BSA concentration was approximately ±10%.

4.4.2 The Absorption Coefficient of BSA Solutions

The complex THz transmission spectra of the empty microfluidic channel, the channel filled with phosphate buffer, and the same channel filled with the BSA solutions were obtained in succession. The microfluidic device was placed at the focus between two 90-degree off-axis parabolic mirrors and the entire experimental setup was N_2 purged. To avoid perturbing the experimental setup, the solutions were pumped into the channel with syringes connected to long Tygon tubing. Scans of the phosphate buffer with a 0.02 THz resolution and BSA solutions exhibited no significant features with spectral width less than 0.15 THz between 0.5 THz - 2.5 THz. This observation is consistent with the THz absorption spectra of water and BSA reported in [55, 58, 59].

The THz transmission of each solution was averaged over three successive scans with a measured reproducibility near 98%. Equation 4.1 is not valid for extracting the absorption coefficient from the measured THz transmission because multiple internal reflections inside the 95 μm channel cannot be ignored.

Instead, the complex index was extracted using Eq. 4.2 which includes these effects but neglects multiple reflections from the thick Zeonor slabs on either side of the channel.

$$t = \frac{E_s(\omega)}{E_a(\omega)} = n_s e^{i\frac{\omega}{c}(n_s-1)d_c} \left[\frac{(n_z+1)^2 - (n_z-1)^2 e^{2i\frac{\omega}{c}d_c}}{(n_z+n_s)^2 - (n_z-n_s)^2 e^{2i\frac{\omega}{c}n_s d_c}} \right] \tag{4.2}$$

$E_s(\omega)$ and $E_a(\omega)$ are the measured THz spectra of the pulse after propagation through the channel filled with solution and with air, respectively. d_c is the channel depth, n_z and n_s are the complex indices of Zeonor and the solution, respectively.

The extracted absorption coefficients of the phosphate buffer and BSA solutions are shown in Fig. 4.4. Consistent with the experimental results in [59], a monotonic decrease in the absorption coefficient of the BSA solution with increasing concentration is observed. This is due to the expulsion of solvent molecules by less-absorbing BSA molecules. The change in absorption coefficient between the 0.05 M phosphate buffer and the 101 mg/mL BSA solution is 15 cm^{-1} - 20 cm^{-1}, or 8%.

4.4.3 The Molecular Absorption Coefficient of BSA

The total THz absorption coefficient of the BSA solution, α_s, can be written in the following way as a linear superposition of the absorption coefficients of the phosphate buffer, α_{pb}, and the hydrated BSA molecules, α_{bsa},

$$\alpha_s = \alpha_{bsa} \frac{V_{bsa}}{V_{bsa} + V_{pb}} + \alpha_{pb} \frac{V_{pb}}{V_{bsa} + V_{pb}} \tag{4.3}$$

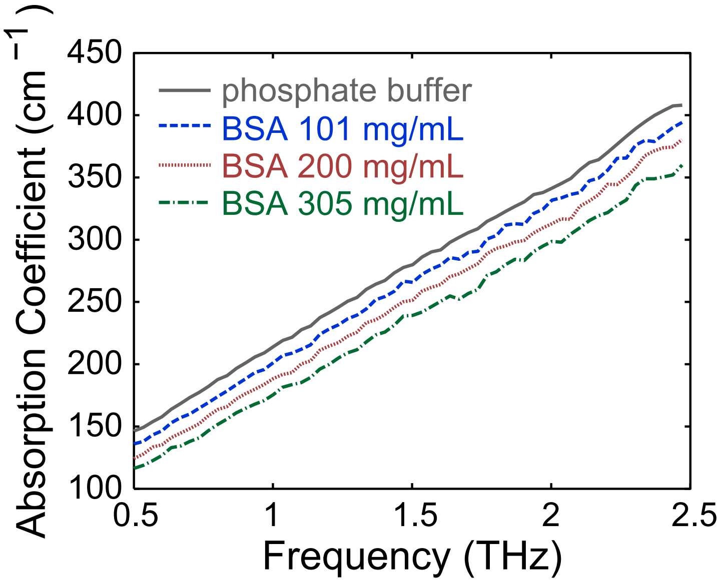

Figure 4.4: The absorption coefficient of the phosphate buffer and BSA solutions measured by THz-TDS using microfluidic devices. Values are extracted using Eq. 4.2.

The values of α_{pb} are already shown in Fig. 4.4. V_{bsa} and V_{pb} are the volumes of the BSA and phosphate buffer in the solution. Based upon density measurements of BSA solutions reported in [58], a molecular radius of 2.8 nm for hydrated BSA was used to calculate V_{bsa}. Figure 4.5 displays the extracted values of α_{bsa} as a function of frequency. The error bars indicate the observed ±10% error in the measurement of the concentrations of the BSA solutions. The absorption coefficient plotted in Fig. 4.5 approaches zero at low frequencies and increases nearly monotonically from 0.5 THz - 2.5 THz due to the increase in the density of molecular vibrational modes [58]. The values of the absorption coefficient extracted from measurements of the 101 mg/mL and 200 mg/mL BSA solutions do not exhibit significant concentration dependence in agreement with Beer's Law [66]. The slight concentration dependence observed for the 305 mg/mL solution is most likely due to uncertainties in the exact solution concentration.

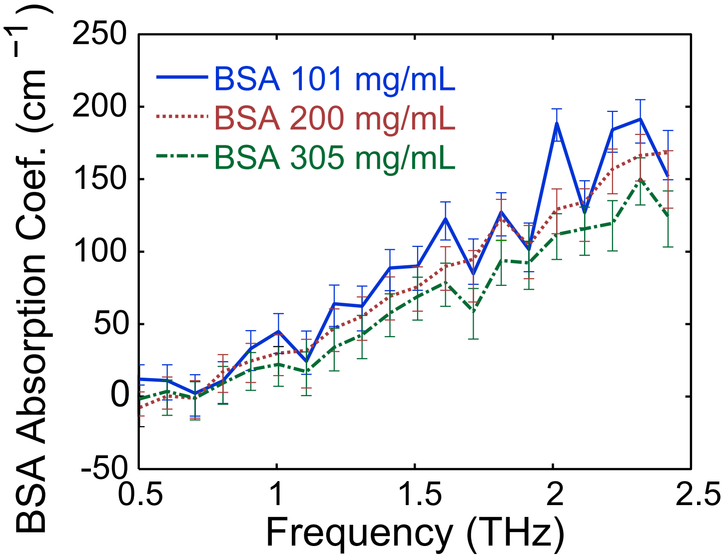

Figure 4.5: The measured molecular absorption coefficient of hydrated BSA molecules. In agreement with Beer's Law, the absorption coefficient does not depend on solution concentration.

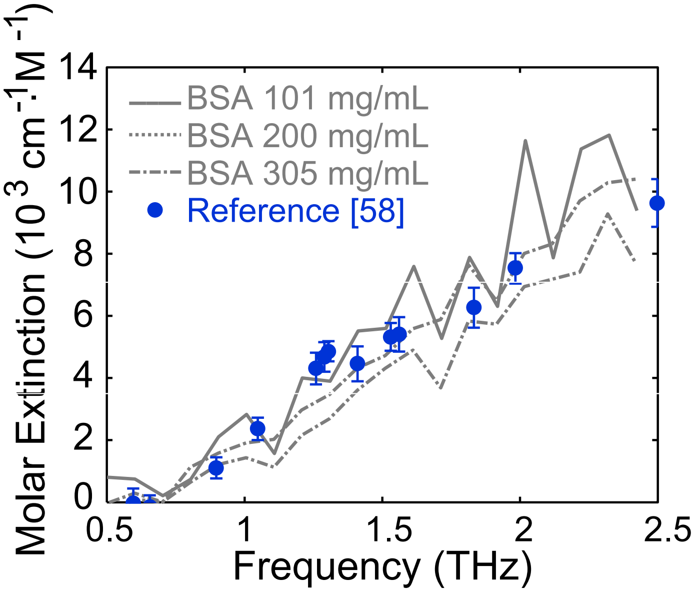

Figure 4.6: The molar extinction of BSA measured using microfluidic channels (from Fig. 4.5) compared to the results in [58] obtained using a high-power free-electron laser. The excellent agreement between the data demonstrates the feasibility of performing THz spectroscopy of biomolecules in microfluidic channels using low-power THz sources.

The molar extinction of BSA molecules in aqueous solution (cm^{-1} M^{-1}), α_{mbsa}, is related to α_{bsa} by

$$\alpha_{mbsa} = \alpha_{bsa} N_A V_{mbsa} \tag{4.4}$$

where N_A is Avogadro's Number and V_{mbsa} is the volume of a hydrated BSA molecule in liters [58]. In Fig. 4.6, we compare our measurement of the molecular extinction of BSA to those reported in [58] using large-volume aqueous solutions of BSA and a high-power THz free-electron laser. The good agreement from 0.5 - 2.5 THz demonstrates the feasibility of performing THz spectroscopy of biomolecules in aqueous solutions using microfluidic channels using low-power THz sources. It should be noted no scaling was used to achieve the fit Fig. 4.6 and that the data is absolute, within the indicated error margins. Assuming a minimum BSA solution concentration of 100 mg/mL, a microfluidic channel of area 500×500 μm^2, and a channel depth of 50 μm, the minimum measurable quantity of BSA is approximately 10 picomoles (0.6 μg).

CHAPTER 5

MEASUREMENT OF THE ULTRAFAST CARRIER DYNAMICS OF EPITAXIAL GRAPHENE USING OPTICAL-PUMP TERAHERTZ-PROBE SPECTROSCOPY

5.1 An Overview of the Electronic Structure of Graphene

Graphene is a 2D lattice of Carbon atoms arranged in a honeycomb crystal structure, as shown in Fig. 5.1 [70, 71]. The direct lattice of graphene is hexagonal and is defined by the lattice vectors $\mathbf{R_1}$ and $\mathbf{R_2}$,

$$\mathbf{R_1} = a\left(\frac{\sqrt{3}}{2}\mathbf{x} + \frac{1}{2}\mathbf{y}\right) \tag{5.1}$$

$$\mathbf{R_2} = a\mathbf{y} \tag{5.2}$$

where the lattice parameter $a = 2.46$ Å. Each primitive cell has a two atom basis consisting of Carbon atoms A and B (Fig. 5.1). The reciprocal lattice of graphene also has a hexagonal structure and the first Brillouin Zone is characterized by the **K** and **K**` points that are each three-fold degenerate. The importance of these points is discussed below.

The conduction and valence bands in graphene result from the formation of π-bands by interacting p_z-orbitals on neighboring A and B atoms. It is convenient to represent these orbitals as eigenvectors in a two-dimensional space,

$$\phi^A_{p_z} = \begin{pmatrix} 1 \\ 0 \end{pmatrix} \qquad \phi^B_{p_z} = \begin{pmatrix} 0 \\ 1 \end{pmatrix} \tag{5.3}$$

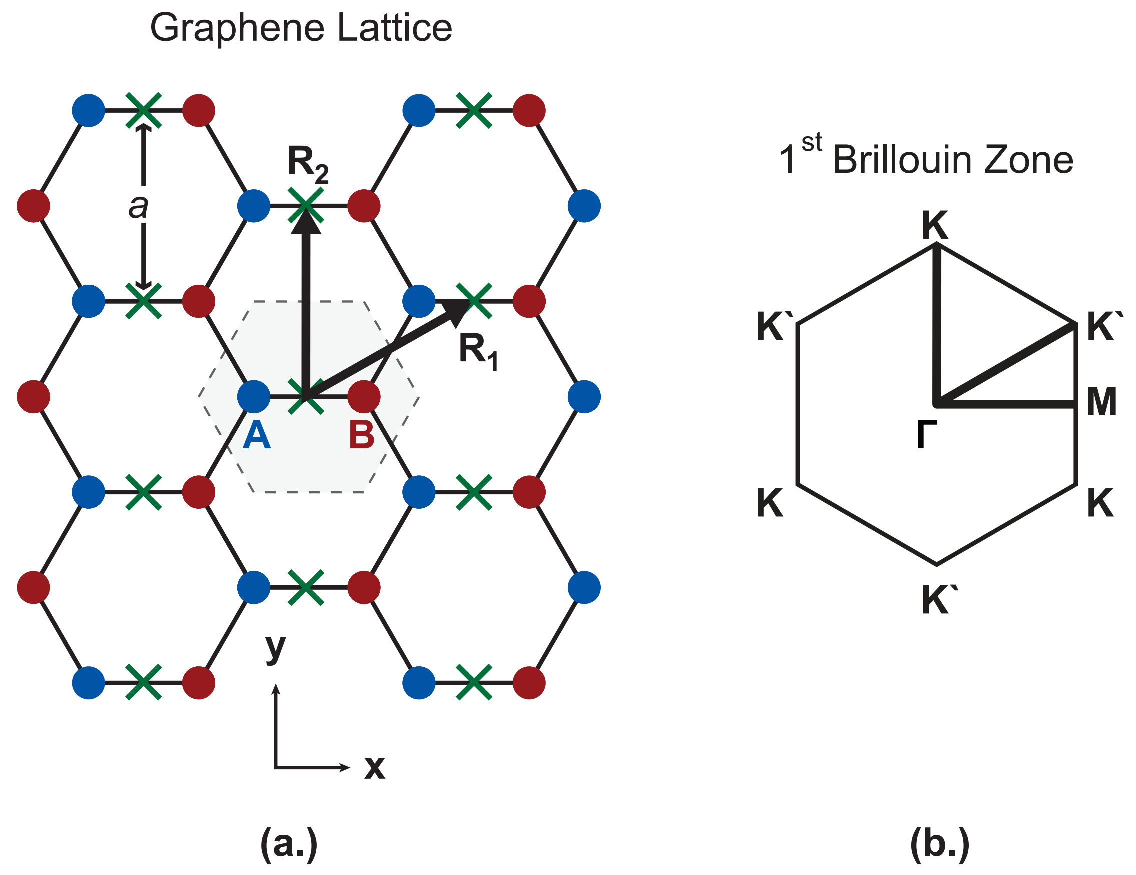

Figure 5.1: The hexagonal crystal lattice of graphene. Lattice points are shown as green crosses. Each primitive cell contains two carbon atoms, A and B. The reciprocal lattice of graphene is also hexagonal. The first Brillouin Zone contains three symmetric **K** points and three symmetric **K**` points.

The conduction and valence band Bloch functions can then be represented in terms of these basis vectors. Considering only first nearest-neighbor interactions, the tight-binding Hamiltonian for graphene is [70, 71],

$$\hat{\mathbf{H}} = \begin{pmatrix} \epsilon_p & -V_{pp_\pi} f(\mathbf{k}) \\ -V_{pp_\pi} f^*(\mathbf{k}) & \epsilon_p \end{pmatrix} \tag{5.4}$$

where the bonding energy $V_{pp_\pi} = 3.0$ eV. $f(\mathbf{k})$ is the atomic structure factor

$$f(\mathbf{k}) = e^{i\mathbf{k}\cdot\mathbf{n_1}} + e^{i\mathbf{k}\cdot\mathbf{n_2}} + e^{i\mathbf{k}\cdot\mathbf{n_3}} \tag{5.5}$$

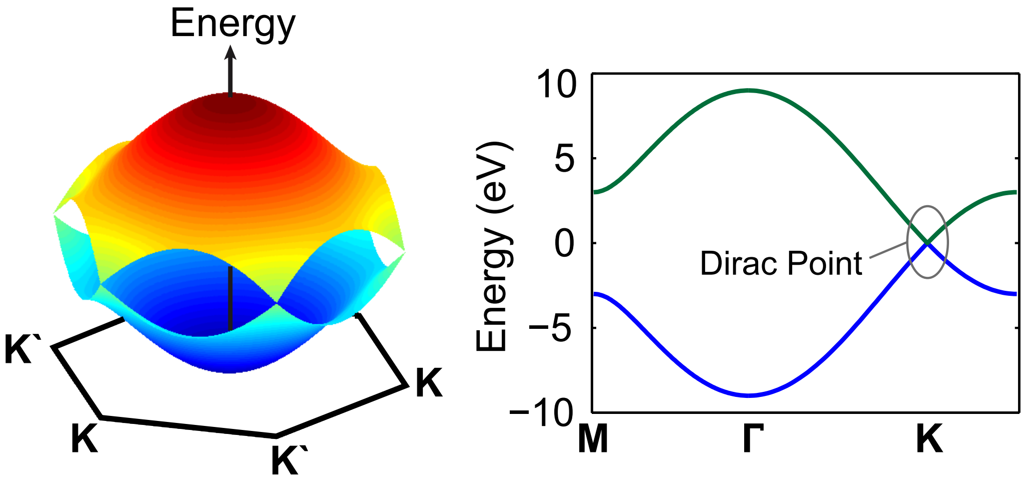

Figure 5.2: Tight-binding band-structure calculations of the conduction and valence bands of graphene. Graphene has zero-bandgap and linear dispersion at the **K** and **K`** points (Dirac points) in the first Brillouin Zone. Carriers at these points behave similar to massless Dirac fermions.

and $\mathbf{n_1} = \frac{a}{\sqrt{3}}\mathbf{x}$, $\mathbf{n_2} = \frac{a}{\sqrt{3}}(-\frac{1}{2}\mathbf{x} + \frac{\sqrt{3}}{2}\mathbf{y})$, and $\mathbf{n_3} = \frac{a}{\sqrt{3}}(-\frac{1}{2}\mathbf{x} - \frac{\sqrt{3}}{2}\mathbf{y})$ are vectors pointing from A to the nearest-neighbor B atoms. In Eq. 5.4, orbitals of neighboring atoms were assumed to be orthogonal. This assumption leads to the (incorrect) result that the conduction and valence bands in graphene are perfectly symmetric. However, for the purpose of this work, higher-order effects arising from the asymmetry of these bands can be ignored. The eigenvectors of the Hamiltonian in Eq. 5.4 corresponding to the conduction band and valence band Bloch functions are

$$\psi_c = \frac{1}{\sqrt{2}}\begin{pmatrix} 1 \\ -f^*(\mathbf{k})/|f(\mathbf{k})| \end{pmatrix} \qquad \psi_v = \frac{1}{\sqrt{2}}\begin{pmatrix} 1 \\ f^*(\mathbf{k})/|f(\mathbf{k})| \end{pmatrix} \tag{5.6}$$

At the Γ-point ($\mathbf{k} = 0$), the conduction band is formed from A and B orbitals that are perfectly out of phase (anti-bonding). Figure 5.2 shows the complete calculated band-structure of graphene.

The electronic structure of graphene has two salient features that make it a promising material for use in futuristic ultra high-speed electronic and optical devices. First, as can be seen in Fig. 5.2, the band-structure exhibits a six-fold degenerate zero-crossing at the **K** and **K`** points that marks both the minimum conduction band energy and the maximum valence band energy. In other words, graphene has zero-bandgap [70, 71]. Second, the band-structure near these points is linear, as is the density of states. Electrons in graphene located at either the **K** or **K`** points have a linear energy momentum dispersion relation and behave like massless Dirac fermions [70, 71, 72].

To illuminate this second point, the Hamiltonian in Eq. 5.4 can be linearized near the **K**-point (known as the Dirac Point) and takes on the following form,

$$\hat{\mathbf{H}} = \hbar \upsilon_f \begin{pmatrix} 0 & k_x - ik_y \\ k_x + ik_y & 0 \end{pmatrix} = \hbar \upsilon_f \sigma \cdot \mathbf{k} \tag{5.7}$$

where $\upsilon_f = 10^6 m/s$ is the Fermi velocity and σ is two-dimensional vector of the 2x2 Pauli spin operators [85]. This representation of the Hamiltonian, which is only valid near the Dirac Points, is similar to that which describes massless spin-1/2 Weyl neutrinos [72]. The energy eigenvalues of Eq. 5.7 are

$$E = \pm \hbar \upsilon_f \sqrt{k_x^2 + k_y^2} = \pm \hbar \upsilon_f |\mathbf{k}| \tag{5.8}$$

In this expression, the positive (negative) sign is chosen when referring to the energy of conduction (valence) band electrons.

The massless Dirac Hamiltonian for graphene is formulated in a two-dimensional basis spanned by vectors describing electron pseudo-spin. The concept of pseudo-spin should not be confused with normal electron spin; in fact, the two are not related. Instead, pseudo-spin refers to the p_z-orbitals of the A and B Carbon atoms in the graphene primitive cell.

The ultra-high carrier mobility characteristic of graphene is partially due to the absence of backscattering and is intimately related to the massless nature of electrons near the Dirac points [72]. As can be seen from Eq. 5.7, massless electrons in graphene are chiral and the electron's pseudo-spin has a component in the direction of its momentum. Therefore, when an electron scatters in backwards and its momentum is changed from $\mathbf{k}$ to $-\mathbf{k}$, its pseudo-spin is also rotated by π. However, because spin-1/2 particles are symmetric about 4π rotations – two complete rotations of the spinor wavefunction –, the electronic

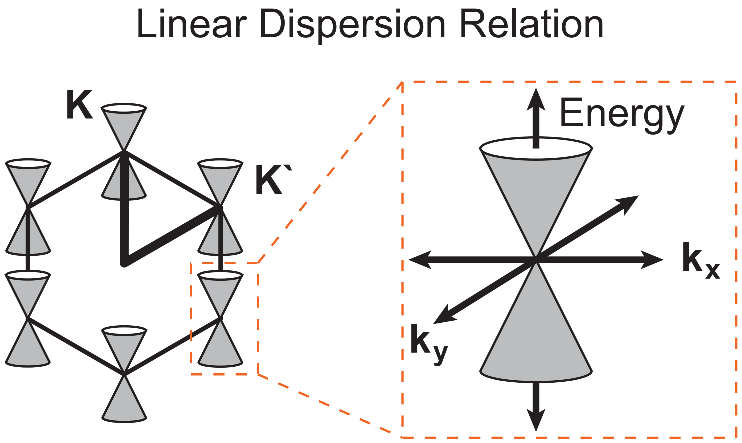

Figure 5.3: A cartoon schematic of the linear energy-momentum dispersion relation in graphene at the six Dirac points. Linear dispersion for electrons in graphene only exists near these points.

wavefunctions resulting from clockwise scattering paths and counter-clockwise scattering paths destructively interfere [72]. The electronic wavefunction after π-rotation of the pseudo-spin is 180 degrees out of phase with the same wavefunction after a rotation by $-\pi$.

5.2 Motivation

The unique electronic and optical properties of graphene make it a promising material for the development of high-speed electron devices, including field-effect transistors, pn-diodes, Terahertz oscillators, and electronic and optical sensors [71, 73, 74, 75, 76, 77]. The realization of graphene-based devices requires understanding the non-equilibrium carrier dynamics as well as the rate at which electron-hole recombination occurs.

Previous measurements of the ultrafast intraband relaxation dynamics of photogenerated electrons and holes in epitaxial graphene using both degenerate [78] and non-degenerate [79] optical-pump optical-probe spectroscopy have been conducted. Similar measurements of exfoliated graphene mono- and multi-layers have also been carried out [80]. These measurements were sensitive to the interband conductivity of graphene and probed the time evolution of the carrier occupation at specific energies in the bands. An important result from these measurements, as well as similar measurements of graphite and carbon nanotubes [81, 82, 83, 84], is that the initial non-equilibrium photoexcited carrier distribution rapidly thermalizes within 30 - 200 fs of excitation and then cools to 300 K in approximately 1 ps due to strong phonon scattering. These results agree very well with the theoretically predicted intraband phonon scattering rates of ~100fs - 1ps in graphene [82].

Because optical-pump optical-probe spectroscopy is only able to resolve the dynamics of the high-energy tails of the electron and hole distributions in graphene, studying the band-edge relaxation and recombination dynamics of cool carriers requires utilizing time-resolved optical-pump THz-probe spectroscopy. At room temperature, the thermal distribution of electrons energies in graphene extends tens-of-meV into the conduction band and resonant interband absorption of THz frequency photons is negligible. Therefore, the optical response of graphene in the THz frequency range at 300K is dominated instead by the intraband conductivity – the free carrier response. Due to the linear dispersion relation of graphene, the intraband conductivity depends not only on the total carrier concentration but also on the carrier distribution in energy [85]. Therefore, optical-pump THz-probe spectroscopy can be used to study the time-evolution of the density of photoexcited electrons and holes as well as the time-evolution of the shape and temperature of their distributions. Using this technique, new insight into the rates of carrier thermalization, cooling, recombination, and relaxation in graphene can be gained. From theoretical predications, it is expected that interband carrier recombination in graphene due to plasmon emission [92], optical phonon scattering [82], and Auger scattering [93] should occur on a 1 - 20 ps timescale at 300 K.

Additionally, it should be noted that the time-resolution of optical-pump THz-probe measurements presented in this chapter is limited by lifetime of the induced sample polarization (in this case, surface currents induced by the incident THz pulse) which is ultimately governed by the electron and hole momentum relaxation times. As will be shown, the momentum relaxation times of the samples used in this work were less than 20 fs and the measurement resolution was therefore ~130 fs. It is expected that all of the ultrafast carrier dynamics in the previous optical-pump optical-pump measurements of the same samples [78] will be present in the optical-pump THz-probe measurements presented below.

5.3 Sample Preparation

The epitaxial graphene samples used in this work were grown on the carbon face of semi-insulating 6*H*-SiC wafers using techniques that have been reported previously [86]. As discussed in [78, 85], X-ray photoemission, Raman, and optical/IR/THz transmission spectroscopy were used to characterize each sample to determine the number of carbon atom layers and the carrier momentum relaxation time. In the following discussion, sample B consists of ~12 carbon

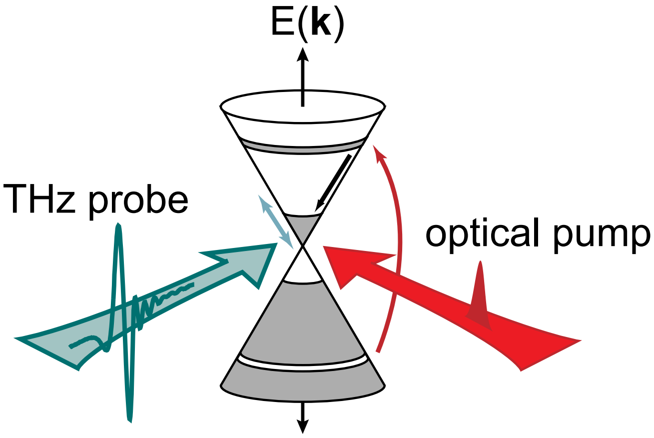

Figure 5.4: A cartoon schematic of optical-pump THz-probe measurements of graphene. Electrons near the band-edge (**K** or **K**` points) are optically excited by an ultrafast laser pulse. Their relaxation and recombination dynamics are then probed at different temporal delays by a few-cycle THz pulse. Because of thermal population of carriers, the THz optical response of graphene at room temperature is dominated by the free carrier response (intraband processes).

atom layers with a momentum relaxation time $\tau \sim 20$ fs and sample C consists of ~19 layers with $\tau \sim 4$ fs [85]. These times were extracted by fitting the optical transmission spectrum of the samples, measured from 200 μm to 400 nm by Fourier-Transform InfraRed (FTIR) spectroscopy, with a theoretical model for conductivity that incorporates both interband (resonant absorption) and intraband (free-carrier response) effects [85].

Raman spectroscopy (at 488 nm) of the samples revealed a G peak close to 1580 cm^{-1} and a D peak close to 1350 cm^{-1}. The D peak is forbidden in perfect graphene layers since it requires an elastic scattering process to satisfy momentum conservation [87, 88]. This is made possible by disorder. The presence of the D peak therefore indicates the presence of disorder in the samples. The average ratio of the intensity of the Raman G and D peaks, I_G/I_D, was 17 for sample B and 2 for sample C. This indicates significantly more disorder in the latter sample [87, 88]. Results from optical-pump optical-probe spectroscopy of sample B were reported earlier in [78].

5.4 Experimental Setup

Details of the optical-pump THz-probe setup are described earlier in Section 2.6. The epitaxial graphene samples were placed at the focus of a 90° off-axis, 1f̈ocal length, parabolic mirror and were excited with 1 nJ - 16 nJ optical pulses (780 nm). The samples were pumped and probed from the backside of the graphene layers through the SiC substrate. Exciting the graphene layers from the backside improved the fidelity of the measurements in two ways. First, the pump-probe signal level was increased because the THz electric-field at the SiC-graphene interface when exciting from the backside was enhanced over the air-graphene interface when exciting from the front. Second, the deleterious effects of multiple reflections of the pump pulse inside the SiC substrate were minimized. The optical pump pulses were focused to a FWHM spot size of 350 - 400 μm to closely match the size of the THz probe. The time-dependent transmission of the THz probe pulse through the optically excited sample was measured by delaying the optical pump pulse with respect to the THz probe. The pump and probe signals were mechanically chopped at 256 Hz and 179.2 Hz, respectively, and the change in the transmission was measured using a lock-in amplifier referenced to the sum of these frequencies.

5.5 The Optical Response of Graphene at THz Frequencies

The complex amplitude transmission of the THz pulse through the graphene layers and the SiC substrate normalized to the transmission through the SiC substrate is (Appendix 1),

$$t = \frac{1}{1 + N\eta_o\,\sigma_{\text{intra}}/(1 + n_{\text{SiC}})} \tag{5.9}$$

N is the number of carbon atom layers, η_o is the free-space impedance, and n_{SiC} is the refractive index of SiC and equals ~2.55. The transmission is related to the complex intraband conductivity of graphene, σ_{intra}, which is given by [85],

$$\sigma_{\text{intra}} = i\frac{e^2/\pi\hbar^2}{\omega + i/\tau}\int_0^\infty \left[f\left(\epsilon - \epsilon_{\text{Fc}}, T\right) + f\left(\epsilon + \epsilon_{\text{Fv}}, T\right)\right] d\epsilon \tag{5.10}$$

In this expression, τ is the momentum relaxation time, $f(\epsilon - \epsilon_{\text{F}}, T)$ is the Fermi-Dirac distribution with carrier temperature T, and ϵ_{Fc} and ϵ_{Fv} are the Fermi energies of conduction band and valence band electrons, respectively. A detailed derivation of the intraband conductivity from the electron-hole propagator in graphene is given in Appendix 2.

The electron and hole densities in graphene are,

$$\begin{pmatrix} n \\ p \end{pmatrix} = \frac{2}{\pi v^2\hbar^2}\int_0^\infty f\begin{pmatrix} \epsilon - \epsilon_{\text{Fc}} \\ \epsilon + \epsilon_{\text{Fv}} \end{pmatrix}, T \Bigg) \epsilon\, d\epsilon \tag{5.11}$$

Equations 5.10 and 5.11 show that, unlike in semiconductors with parabolic energy bands in which the Drude intraband conductivity depends solely upon the total carrier, the intraband conductivity of graphene depends on the shape of the carrier distribution in addition to the carrier density. In graphene, a hotter carrier distribution corresponds to a smaller intraband conductivity than a cooler distribution with the same carrier density. This can be understood intuitively in the following way: As the distribution cools (with carrier density held constant), the non-equilibrium electron (hole) Fermi level moves up (down) toward the band edge in such a way that, despite the concurrent reduction of the tail of the distribution in the conduction (valence) band, the integral of the Fermi distribution in Eq. 5.10 – the total ”area” under the distribution in the band – increases. Therefore, the intraband conductivity, which is linearly proportional to this integral increases as well.

In intrinsic photoexcited graphene layers, $n = p$ and $\epsilon_{\mathrm{Fc}} = -\epsilon_{\mathrm{Fv}}$. In epitaxial graphene, the first one or two carbon atom layers adjacent to the SiC substrate are expected to have a large carrier density [86, 79]. However, the change in the THz intraband conductivity, as measured in our experiments, is dominated by the large number of intrinsic layers. The contribution of the doped layers to our measurements has therefore been ignored in the discussion that follows.

5.6 Carrier Relaxation and Recombination Processes in Graphene

Figure 5.5 shows the measured THz pulse transmitted through graphene sample B with (scaled for clarity) and without optical excitation for a probe delay of 1 ps. In this work, we measured the change in the transmission of the peak of the THz probe pulse caused by optical excitation. Because of the small momentum relaxation time of samples B and C, the real part of the intraband conductivity is much larger than the imaginary part and is nearly dispersionless in the low THz frequency range. In addition, the first order contribution from the change in the imaginary part of the conductivity to the change in the pulse transmission is exactly zero at the peak of the THz pulse. Consequently, near the peak, optical excitation primarily affects the amplitude of the THz probe pulse and does not distort the pulse shape or shift the pulse in time.

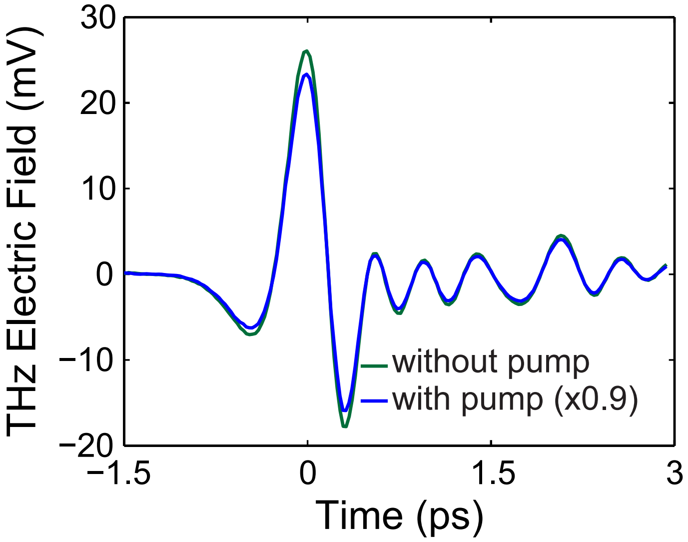

Figure 5.5: Measured THz pulses transmitted through the epitaxial graphene sample B without (grey) and with (black, scaled) an optical pump pulse preceding the peak of the THz pulse by 1 ps. The the intraband conductivity of both samples B and C is almost entirely real and is nearly dispersionless at low THz frequencies. Consequently, the amplitude of the peak of the THz probe pulse is altered in the presence of the optical excitation but the pulse shape is not distorted nor is it shifted in time. Ringing after the pulse is due to absorption from water vapor.

Figure 5.6(a) displays the experimentally measured time-dependent change in the real part of the normalized transmission of sample B resulting from excitation by a 14.8 nJ optical pulse. This pulse was focused to a 250μm spot-size and produced a photoexcited carrier density of 3×10^{11} cm^{-}2. The time evolution of the transmission exhibits two distinct features: (1) an initial rapid decrease until 0.75 ps - 1 ps (left of dashed vertical line in inlay) followed by (2) a slow increase from 1 ps - 15 ps. The initial rapid decrease, shown in the inlay in Fig. 5.6, is within the (estimated) 130 fs temporal resolution of our measurements and is consistent with an increase in conductivity due to cooling of the thermalized carrier distribution after photoexcitation. The slow increase in the transmission is due to the decrease in conductivity resulting from electron-hole recombination and does not follow a simple exponential dependence (Fig. 5.6(b)). This is indicative of density-dependent carrier recombination times.

The likely processes by which non-equilibrium photogenerated electron and hole distributions return to equilibrium are shown pictorially in Fig. 5.7. Immediately following optical excitation, electrons (holes) are in a non-thermal distribution with a large population near 0.8 (-0.8) eV from the band edge. Within 10 fs - 150 fs, this distribution thermalizes and cools to form a hot Fermi-Dirac distribution [78]. Intraband phonon scattering further cools the thermalized carriers between 150 fs and 1 ps. Beyond ~1 ps, electron-hole recombination is the dominant processes affecting the intraband conductivity and the THz transmission. Intraband relaxation times in the 0.4 ps - 1.7 ps range were measured by the authors previously using optical-pump and optical-probe spectroscopy of epitaxial graphene [78]. The intraband relaxation times measured in this work are slightly different. This small difference can be attributed to the fact that in [78] the time-dependent optical transmission depended on the carrier occupation at a specific energy in the high energy tail of the distribution, whereas in the present case the time-dependent THz transmission is sensitive to the changes in the distribution at all energies.

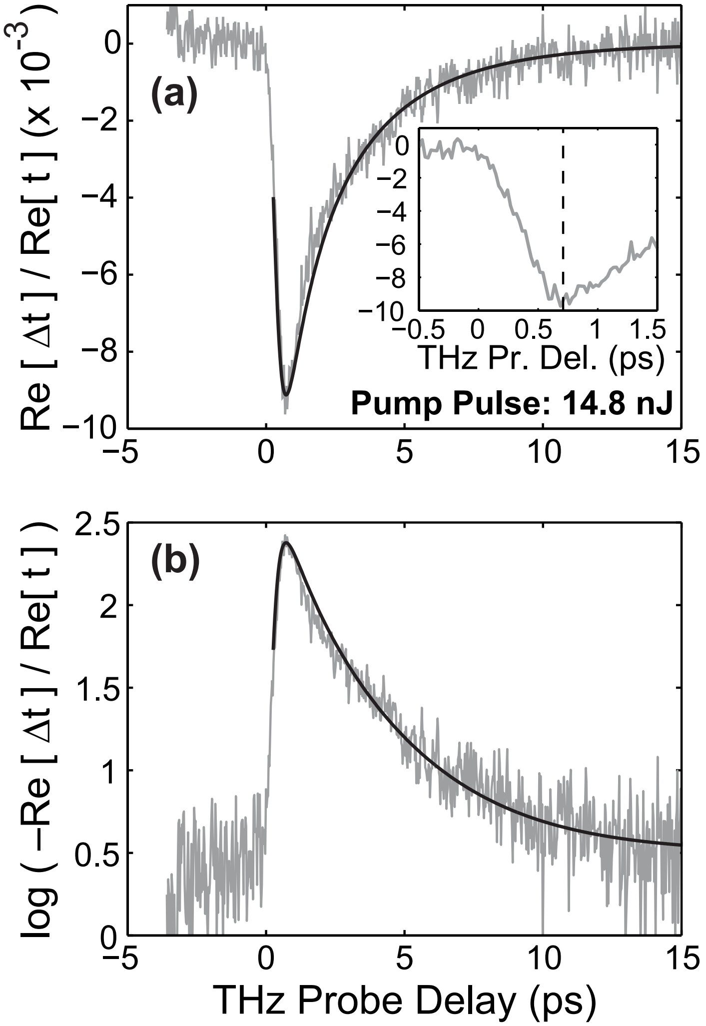

Figure 5.6: (a) The measured change in the real part of the complex amplitude transmission (grey) and the theoretical fit (black) for pump pulse energy of 14.8 nJ (sample B). The transmission decreases rapidly until 0.75 ps - 1 ps and then increases slowly from 1 ps - 15 ps. The inlay shows the initial rise in the transmission, which occurs on a timescale longer than the experimental resolution of 130 fs. (b) The same data plotted on a logarithmic scale. The slow increase in the transmission does not follow an exponential curve.

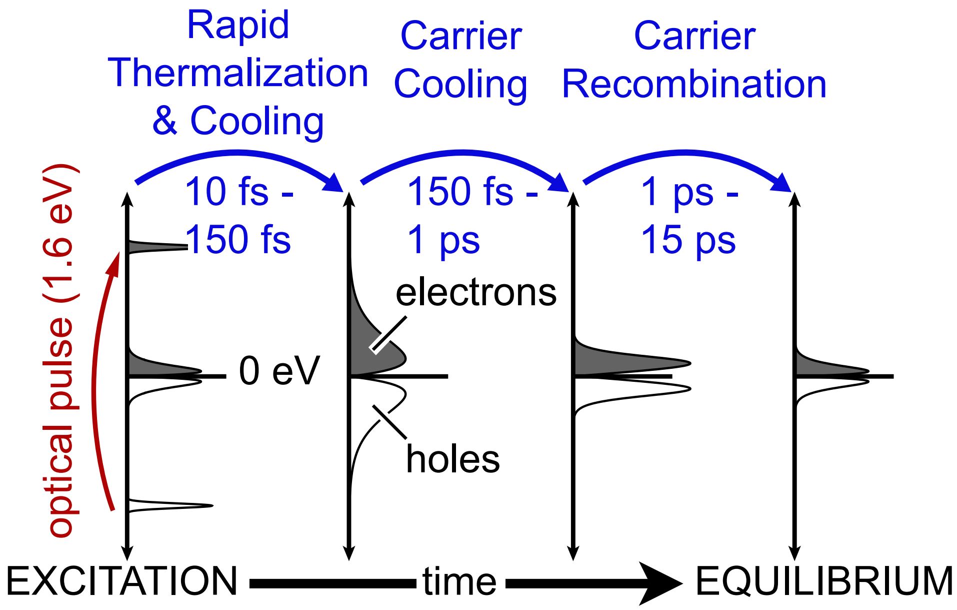

Figure 5.7: A schematic of the likely processes by which optically-excited, non-equilibrium electron and hole distributions approach equilibrium. After excitation, the distribution rapidly thermalizes and cools. The hot thermally distributed carriers are then cooled further due to intraband phonon scattering. Finally, electrons and holes recombine until the equilibrium distribution is restored.

5.7 Theoretical Model

The simple coupled rate equations below can be used to model the carrier dynamics after optical excitation and subsequent thermalization.

$$\frac{d}{dt}T = -\frac{T - T_{\text{eq}}}{\tau_c} \tag{5.12}$$

$$\frac{d}{dt}n = -B\left(n^2 - n_{\text{eq}}^2\right) - Cn\left(n^2 - n_{\text{eq}}^2\right) \tag{5.13}$$

These equations model the cooling of the carrier temperature T towards the equilibrium temperature with a phenomenological time constant τ_c and the decay of the carrier population due to recombination. The mechanisms responsible for electron-hole recombination in graphene could include plasmon emission, intervalley and intravalley optical phonon scattering, and Auger scattering. In general, recombination rates due to these processes are expected to have non-trivial carrier density dependencies [77, 82, 93, 91, 94]. Additionally, carrier generation rates cannot be ignored in the analysis [93]. We assume that the net recombination rate $R(n)$ can be expressed as a quadratic function of n, $R(n) = B(n^2 - n_{eq}^2)$, where it is assumed that $n = p$ and n_{eq} is the carrier density at thermal equilibrium. B is a fitting parameter. Equations 5.12, 5.12, and 5.11 are solved self-consistently at every point in time for a given density of photogenerated carriers. From the time-dependent carrier temperature T and density n, the conductivity σ_{intra} and the THz transmission can be determined.

The agreement between the model (black) and the measured data (grey) for the THz probe transmission transient is also shown in Fig. 5.6. For a pump pulse energy of 14.8 nJ, the photoexcited carrier density was estimated to be $\sim 5 \times 10^{11}$ cm^{-2}. To best fit the measured data, the carrier temperature within the ~200 fs of thermalization was found to be 1250 K. The temporal resolution of the experiments limited the ability to resolve the dynamics of the high-energy non-thermal photoexcited carriers immediately upon excitation. Within one resolution timescale (~ 130 fs) following excitation, it is expected that the carriers rapidly thermalize with a temperature of several thousand K and cool from 1250 K via phonon scattering [84, 81, 82]. The values of τ_c and B were found to be 200 fs and 1.8 cm^2 s^{-1}, respectively. To explore the carrier density dependence of the measured transients, experiments were conducted with optical pump pulse energies varying from 1 nJ to 15 nJ. The model also exhibits an excellent fit to

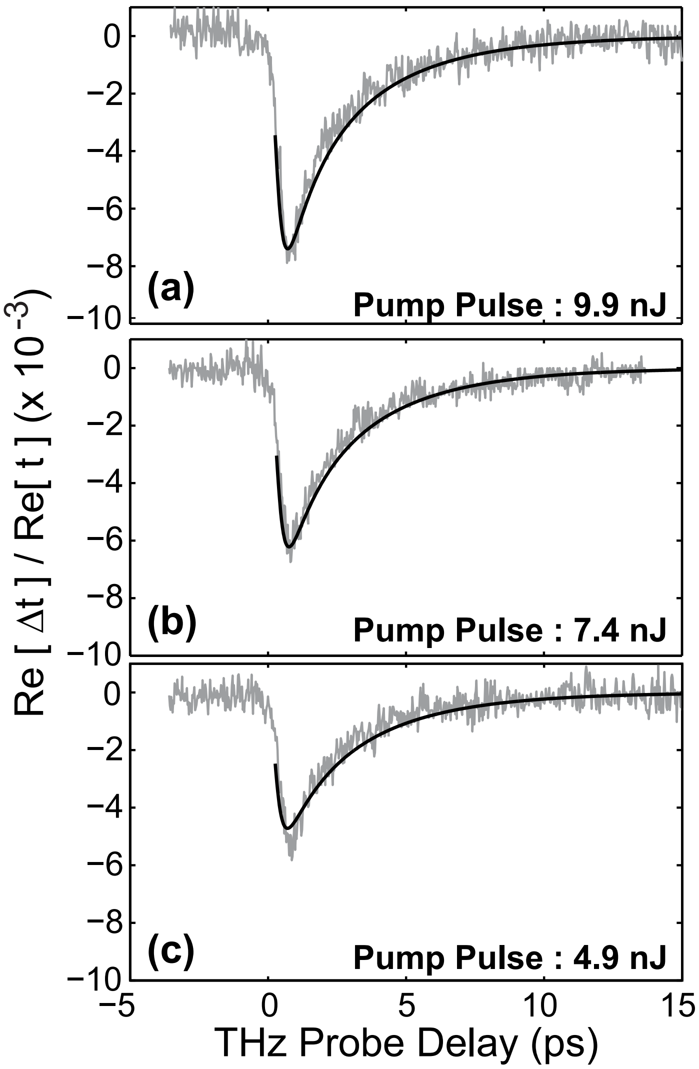

Figure 5.8: The theoretically predicted and experimentally measured changes in the real part of the transmission for optical-pump pulse energies of (a) 9.9 nJ, (b) 7.4 nJ, and (c) 4.9 nJ (sample B). The model captures both the fast decrease and the slow increase of the transmission for different pump pulse energies.

the data for different pump pulse energies, as shown in Fig. 5.8 for pump pulse energies of 9.9, 7.4, and 4.9 nJ. In the model, the initial photoexcited carrier density and the initial carrier temperature were scaled linearly with the pump pulse energy [78]. It is important to emphasize here that the model captures the initial decrease in the transmission, the peak change in the transmission, and the slow increase in the transmission for different pulse energies without changing the values of B or τ_c. Figure 5.9 shows good agreement between the measured and the calculated peak change (absolute minimum, see inlay) in the THz transmission for pump pulse energies varying from 1 nJ to 15 nJ. The extracted value of τ_c agrees well with the calculated and measured inelastic carrier-phonon intraband scattering times in graphene [89] and in carbon nanotubes [81, 90]. Using the extracted value of B, the calculated recombination rates for carrier densities in the $10^{11} - 10^{12}$ cm^{-2} range are approximately equal to the summation of the theoretically predicted recombination rates due to optical phonon scattering and Auger scattering in graphene [**?**, 93]. It should be mentioned that the net recombination rate $R(n)$ can have a carrier density dependence different from the assumed quadratic expression. For example, in [93] it has been shown that the Auger recombination rate in graphene can have a cubic dependence on the carrier density. The coefficient B can also be carrier density dependent [93]. However, for the values of the carrier density relevant to our experiments the calculated auger recombination rates have an almost quadratic dependence on the carrier density [93]. In addition, within the resolution of our experiments, a constant value of B adequately fits the data.

In [78] and [85] it was shown that the intraband energy and momentum relaxation rates in epitaxial graphene depend on material disorder. Disorder could also affect the interband recombination rates since disorder can modify

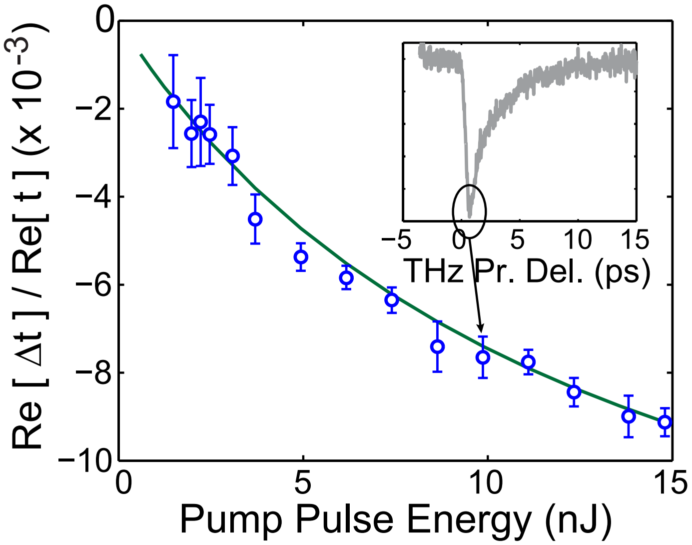

Figure 5.9: The measured and the predicted peak change in the real part of the complex THz transmission for different pulse energies (sample B).

the density of states [95] and/or provide the additional momentum necessary to satisfy the conservation rules in recombination processes [96, 97]. Optical-pump THz-probe spectroscopy was performed on epitaxial graphene sample C which, as discussed earlier, is significantly more disordered than sample B. The value of B for sample C was obtained using the methods discussed above and equals 3.1 cm^2 s^{-1}. The carrier recombination rate is approximately twice as fast in sample C than in sample B for the same carrier density.

CHAPTER 6

MEASUREMENT OF THE CARRIER DYNAMICS AND POLARIZATION-SELECTIVE TERAHERTZ RESPONSE OF ORIENTED GERMANIUM NANOWIRES USING OPTICAL-PUMP TERAHERTZ-PROBE SPECTROSCOPY

6.1 Motivation

In recent years, semiconductor nanowires have gathered much interest. Nanowires have been applied to an array of applications that highlight their versatility as building blocks of integrated electronic (transistors) and photonic (waveguides, lasers, photodetectors, solar cells) components [103, 104, 105, 106, 107, 108]. Germanium nanowires are of particular interest due to the attractive material properties of germanium, including large electron and hole mobilities and large optical absorption in the visible/near-IR. These properties could make germanium nanowires useful for next generation electrical and photonic devices, such as transistors, CMOS compatible photodetectors, and solar cells. Before any of these devices can be built, however, it is important to first understand the fast electrical and optical response as well as ultrafast dynamics of carriers in nanowires. In this chapter, results of the optical-pump THz-probe (OPTP) measurements of the ultrafast carrier dynamics in photoexcited germanium nanowires using will be presented.

The ultrafast carrier dynamics of group III-V, II-VI, and IV semiconductor nanowires have been studied with optical-pump optical-probe spectroscopy [109, 110]. These measurements are sensitive primarily to the carrier occupation of specific regions in the energy bands. Optical-pump THz-probe spectroscopy, in which the probe photon energy (~5 meV) is substantially less than the bandgap, is sensitive to not only the total carrier density but also to the distribution of these carriers in energy within the bands. The latter is true since the energy distribution of carriers affects the optical conductivity at THz frequencies [32]. Optical-pump THz-probe spectroscopy can therefore be used to simultaneously study both intraband relaxation and interband recombination dynamics of photoexcited electrons and holes on ultrafast time scales. As will be discussed, these measurements show intraband carrier relaxation rates (attributed to intravalley and intervalley phonon scattering) in the 1.5-2 ps range and carrier density-dependent recombination rates (attributed to nanowire surface defects) in the 75-125 ps range at room temperature in 80 nm diameter wires.

The fast electrical response of nanowires at THz frequencies can also be studied with OPTP spectroscopy [33]. Using this technique, the measured carrier momentum scattering time is in the 60-90 fs range. Additionally, the THz response of oriented nanowires is strongly dependent upon the polarization of the incident THz field. The differential THz transmission through photoexcited nanowires is most affected when the THz field is polarized parallel to the nanowires, while no appreciable response is detected when the THz field is polarized perpendicular to the nanowires. The shape anisotropy of the nanowires at subwavelength scales leads to a strong polarization dependent macroscopic THz response.

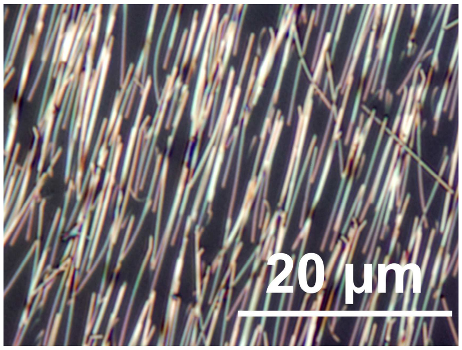

Figure 6.1: Darkfield optical micrograph of oriented 80 nm diameter germanium nanowires placed flat on a quartz substrate (100X, NA 0.9 objective). Note: Nanowires appear wider than 80 nm due to diffraction.

6.2 Sample Preparation and Experimental Setup

Germanium nanowires used in this work were ~80 nm in diameter and ~10 μm in length (see Fig. 6.1). They were grown via CVD in a hot-walled quartz tube furnace using Germane as the source gas and gold nanoparticles for the catalyst [111]. Germanium nanowires produced with this method are known to grow predominantly in the $\langle 111 \rangle$ direction [112]. Alignment of nanowires was achieved on quartz crystal substrates using a contact printing method previously reported by Fan *et al.*[113]. Nanowires used in this experiment were not intentionally doped, and expected initial carrier density is less than 10^{17} $1/\mathrm{cm}^3$.

The OPTP spectroscopy experimental setup used was identical to that discussed in Chapter 5, with the addition of a wire-grid THz polarizer placed after the nanowire sample.

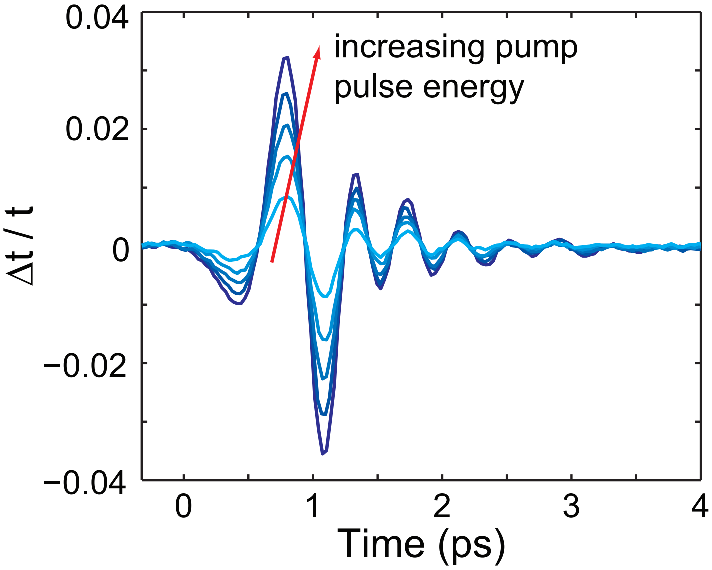

Figure 6.2: The measured differential amplitudes of THz pulses transmitted through photoexcited germanium nanowires for pump pulse energies of 10.2, 8.2, 6.1, 4.1, and 2.0 nJ are plotted for a fixed pump-probe delay. The THz field is polarized parallel to the nanowires, and the differential amplitudes plotted are scaled by the peak amplitude of the transmitted THz pulse in the absence of photoexcitation.

6.3 Carrier Relaxation and Recombination Processes in Germanium Nanowires

Figure 6.2 shows the measured differential amplitudes of THz pulses transmitted through photoexcited germanium nanowires for pump pulse energies of 10.2, 8.2, 6.1, 4.1, and 2.0 nJ at a fixed pump-probe delay. The THz field is polarized parallel to the nanowires. Since double-chopping is employed, the measured differential signal is affected only by the THz response of the photoexcited carriers within the nanowires. Figure 6.2 displays no measurable carrier density dependence in the frequency dispersion of the THz response since the measured pulse shape remains unchanged for different pump pulse energies (only the pulse amplitude changes). As discussed in detail below, carrier density independent dispersion is a result of very small surface plasmon frequencies. These results show that the dynamics of photoexcited carriers can be studied by measuring the differential amplitude of the peak of the transmitted THz pulse as a function of the pump-probe delay [31].

Figure 6.3 shows the measured differential amplitude of the peak of the THz probe pulse as a function of the pump-probe delay for different optical pump energies. The THz transmission decreases in the first ~5 ps following the optical excitation and then recovers on a 75-125 ps time scale. These two time scales in the measured transient can be explained by the intraband and interband carrier dynamics, respectively. The optical pulse creates electron-hole pairs near the Γ-point in the germanium reciprocal lattice (see Fig. 6.4). Electrons quickly scatter from the Γ-point to the X-point within 100 fs due to strong intervalley phonon scattering, after which they scatter to the lowest L-valley within a few picoseconds [114]. Photoexcited holes in the three valence bands are also expected to thermalize within 0.5 ps [114] and cool due to optical phonon emission within a few picoseconds [115]. The presence of high mobility electrons in the L-valley and high mobility holes at the top of the light hole band causes the THz optical conductivity to increase. Therefore, the transmission of the incident THz radiation decreases as the photoexcited carriers relax to these points within the first several picoseconds after optical excitation. The transmission of the THz radiation then recovers (increases) on a slower time scale as the hole and the electron densities decrease due to interband recombination.

Using a simple theoretical model discussed below, the fits to the measured

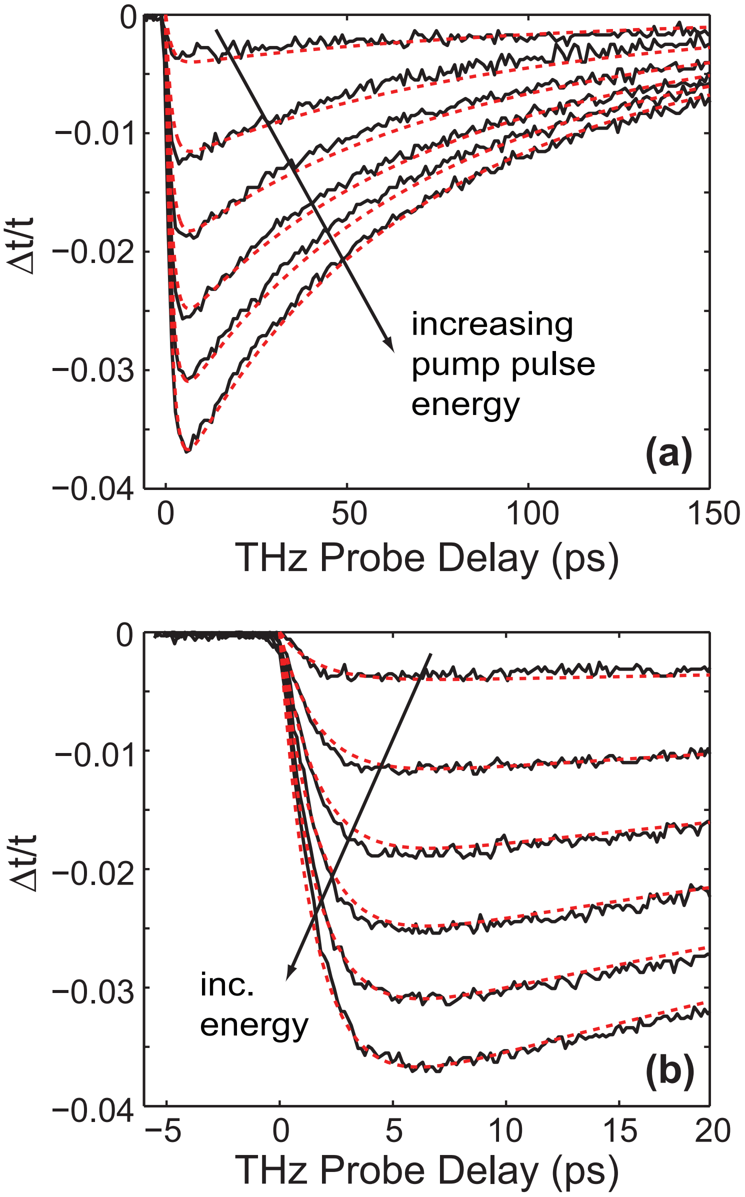

Figure 6.3: (a) Measured (solid lines) normalized differential amplitude $\Delta t/t$ of the peak of the THz probe pulse is plotted as a function of the pump-probe delay for optical pump energies of 12 nJ, 9.8 nJ, 7.6 nJ, 5.4 nJ, 3.3 nJ, and 1.1 nJ. The theoretical fit (dashed lines) is also shown. THz probe transmission is seen to recover on a 75-125 ps time scale. (b) Close-up of the differential transmission transient.

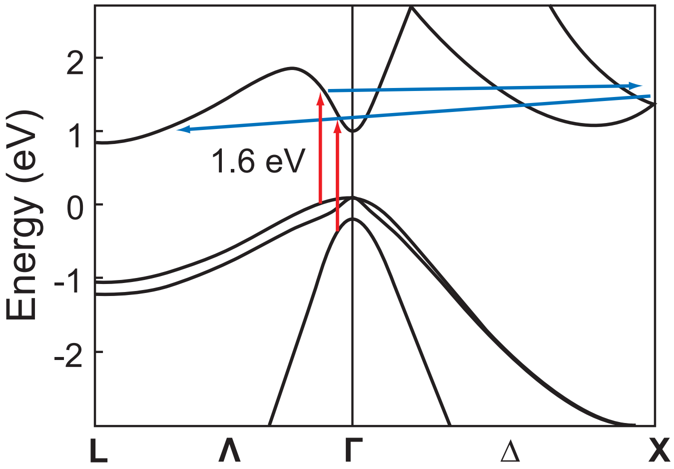

Figure 6.4: Ultrafast dynamics of photoexcited carriers in a germanium nanowire energy band are depicted [114]. Electrons are photoexcited near the Γ point and quickly scatter to the X point. In the next few picoseconds electrons scatter to the L-valley where they remain until they recombine with the holes.

transients are also shown in Fig. 6.3. A characteristic time scale of 1.7 ps is extracted for the initial transmission decrease. Since the experiment is sensitive to the total conductivity of both electrons and holes, this value of 1.7 ps corresponds to an average intraband relaxation time associated with hole cooling and electron scattering from the X-point to the L-point. The measured relaxation time is consistent with the calculated rates and previously reported measurement results [109, 115, 116]. In bulk germanium, carrier recombination rates are highly dependent on the doping density. Recombination times as long as hundreds of microseconds for undoped germanium [117] and as short as hundreds of picoseconds for doped germanium [116] have been reported. Our measurements show that electrons and holes in 80 nm germanium nanowires recombine with carrier density-dependent recombination times between 75-125 ps. This shorter time scale, compared to that in bulk germanium, indicates that surface defect states may be responsible for faster recombination in agreement with recent electrical and optical pump-probe measurements [109, 118].

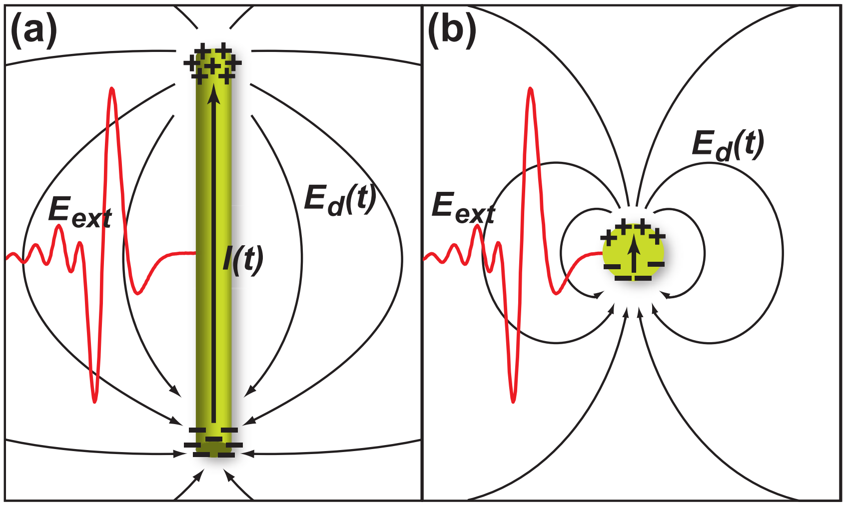

Figure 6.5: (a) A nanowire oriented parallel to the polarization of the external THz field (E_{ext}). The depolarization field (E_d) due to charge confinement on the surface of the nanowire is weak, allowing a Drude-like induced current. (b) A nanowire oriented perpendicular to the external field polarization. Here, the depolarization field is strong, suppressing the induced current.

6.4 The Plasmon Response of Germanium Nanowires

The THz frequency response of a finite length nanowire can be described by the Drude model modified to consider the depolarization fields [119] due to the induced charges on the surface of the nanowire [33, 120, 121]. The inclusion of the depolarization field leads to a surface-plasmon-like resonance in the frequency dependent current response of the nanowire. The current $I(\omega)$ in a nanowire of cross-sectional area A can be written as,

$$I(\omega) = A\frac{\sigma_\circ}{1 - i\omega\tau}(E_{\text{ext}}(\omega) + E_d(\omega)) \tag{6.1}$$

where $\sigma_\circ$ is the DC conductivity of the nanowire material, τ is the carrier momentum scattering time (assumed to be the same for both electrons and holes [122]), $E_{\text{ext}}(\omega)$ is the applied field and $E_d(\omega)$ is the depolarization field. The above expression can also be expressed as, $I(\omega) = A\sigma_{\text{eff}}(\omega)E_{\text{ext}}(\omega)$, where the effective conductivity $\sigma_{\text{eff}}(\omega)$ is

$$\sigma_{\text{eff}}(\omega) = \frac{\sigma_\circ}{1 - i\omega\tau(1 - \Omega_p^2/\omega^2)} \tag{6.2}$$

Here, Ω_p is the frequency of the surface plasmon resonance. Ω_p is related to the bulk plasma frequency ω_p by a constant factor g that depends on the polarization of the applied field with respect to the nanowire axis (see Fig. 6.5). For a field polarized perpendicular to the nanowire, g equals $\sqrt{\epsilon_s/(\epsilon_s + \epsilon_\circ)}$, where ϵ_s and $\epsilon_\circ$ are the permittivities of the nanowire material and free-space, respectively. In the case of the field polarization parallel to the nanowire, the value of g is small and is on the order of $(d/L)\sqrt{\epsilon_s/\epsilon_\circ}$, where d and L are the diameter and length of the nanowire respectively. Since $d \ll L$, when the field is polarized parallel to the nanowires, Ω_p is much smaller than ω_p. Ω_p was estimated to be less than 300 GHz for even the largest photoexcited carrier densities in these experiments. The interaction between nanowires is expected to reduce the depolarization field inside the nanowires and, therefore, further reduce the value of Ω_p. At frequencies much larger than Ω_p, $\sigma_{\text{eff}}(\omega)$ reduces to the Drude result. In the DC limit, $\sigma_{\text{eff}}(\omega)$ goes to zero as is expected for a finite-length uncontacted nanowire. The differential THz transmission (normalized to the transmission in the absence of photoexcitation) can be written as (see Appendix I),

$$\frac{\Delta t(\omega)}{t} = \frac{1}{1 + \sigma_{\text{eff}}(\omega)\, F(\omega)\, \eta_\circ\, f\, d/(1+n)} - 1 \tag{6.3}$$

$$\approx -\sigma_{\text{eff}}(\omega)\, F(\omega)\, \eta_\circ\, f\, d/(1+n) \tag{6.4}$$

where $\eta_\circ$ is the impedance of free space, $f \approx .08$ is the fill factor of the nanowires, $d = 80$ nm is the diameter of a nanowire, and $n = 1.96$ is the THz refractive index of the quartz substrate [123]. $F(\omega)$ is an overlap factor that accounts for the frequency dependence of the measured THz response due to the mismatch between the optical and THz focus spots. Assuming Gaussian transverse intensity profiles for the optical and THz beams, the overlap factor is found to be,

$$F(\omega) = \omega^2/(\omega_\circ^2 + \omega^2) \tag{6.5}$$

where $\omega_\circ \approx 2\pi c/a$ is approximately the frequency corresponding to the standard deviation, $a = 150\ \mu$m, of the optical beam transverse intensity profile. In the case of the THz field polarized along the nanowires, since $\Omega_p \ll \omega$ for frequencies ω in the 0.5-3.0 THz range, $\sigma_{\text{eff}}(\omega)$ has the frequency dependence of the Drude model. There is therefore no carrier density dependence in the frequency dispersion of the differential THz transmission, in agreement with the measured results shown earlier in Fig. 6.2. Figure 6.6 shows the measured frequency spectra (solid lines) of $|\Delta t(\omega)/t|$ for different pump pulse energies. Also shown are the theoretical fits (dashed lines) obtained from Eq. 6.4. As seen in 6.6, the theory agrees well with both the frequency dependence and the carrier density dependence of the data. The extracted momentum scattering time is $\tau = 70 \pm 15$ fs, which corresponds to an effective electron plus hole mobility of 1590 $\text{cm}^2/(\text{V}\cdot\text{sec})$. This is smaller than the reported value for the bulk germanium electron plus hole mobility of 5700 $\text{cm}^2/(\text{V}\cdot\text{sec})$ at 300 K [122].

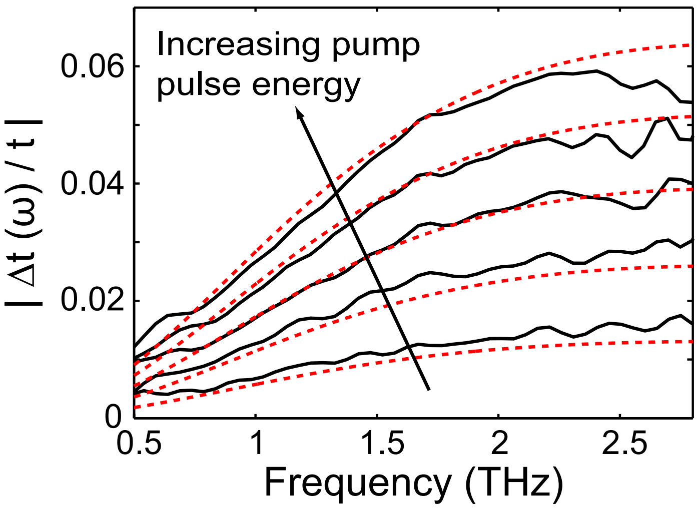

Figure 6.6: Data (solid) and theory (dashed) for the spectra of the differential THz transmission $|\Delta t(\omega)/t|$ is plotted for different pump pulse energies. The theory assumes a standard deviation of ~150 μm for the optical intensity profile at the focus and a momentum scattering time $\tau = 70 \pm 15$ fs independent of the carrier density.

6.5 Rate-Equation Model for Carrier Dyanmics

Equation 6.4 shows that the differential THz transmission is approximately proportional to the carrier density through $\sigma_{\text{eff}}(\omega)$. If the carrier density changes on a time scale much slower than the momentum scattering time, then the differential amplitude of any one point on the transmitted THz pulse measured as a function of the pump-probe delay can be used to study ultrafast carrier dynamics. The time resolution in the experiments was limited by the width of the optical pump pulse to ~150 fs.

To describe the complete differential THz transmission transient shown in Fig. 6.3, the time dependence of the photoexcited carrier densities in the germanium nanowires was modeled with rate equations. Because the measured differential transmission depends on the total conductivity of both electrons and holes, and, as mentioned earlier, the time scales associated with the intraband relaxation dynamics of both electrons and holes are expected to be nearly the same, both electron and hole dynamics can be modeled with the same rate equations. The photoexcited electron and hole density at higher energies, N', were assumed to relax with a characteristic time τ_r. The density of the cool electrons and holes at the L- and Γ-valleys, respectively, is N and it is assumed that only cool, high mobility electrons and holes interact with the THz radiation until they recombine [114]. Recombination in bulk germanium with low doping is generally attributed to Shockley-Reed-Hall (SRH) defect assisted recombination. Auger recombination becomes dominant for doping densities above 10^{18} cm^{-3} [117]. Surface defect recombination in nanowires is also expected to have carrier density dependence similar to that of the bulk SRH mechanism.

The recombination rate is described by a second-order polynomial in the electron and hole density N.

$$\frac{dN'}{dt} = -\frac{N'}{\tau_r} \qquad\qquad \frac{dN}{dt} = \frac{N'}{\tau_r} - (A\,N + B\,N^2) \tag{6.6}$$

The initial photoexcited density $N'(t = 0)$ is estimated to be 4.5×10^{18} $1/\mathrm{cm}^3$ for a 12 nJ pump pulse and is assumed to scale linearly with the pump pulse energy. The DC conductivity $\sigma_\circ$ equals $(\mu_e + \mu_h)eN$, where μ_e and μ_h are the electron and hole mobilities. Agreement between the rate equation model and the data is shown in Fig. 6.3, where the extracted values of the various parameters for best fit are as follows: $\tau_r = 1.7$ ps, $A = 8.8 \times 10^9$ 1/sec, and $B = 2 \times 10^{-9}$ $\mathrm{cm}^3/\mathrm{sec}$. This model agrees with the data for all pulse energies. The necessity of the B parameter indicates carrier density-dependent recombination rates in germanium nanowires, which is consistent with density-dependent SRH surface and Auger recombination [124].

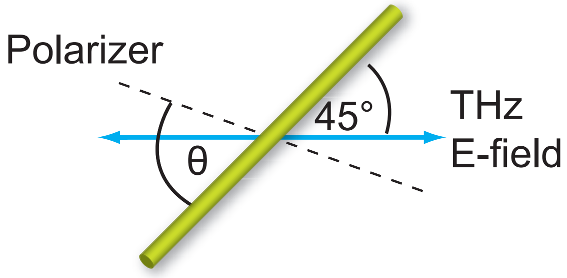

Figure 6.7: The incident THz polarization is fixed at 45° with respect to the nanowire axis. A polarizer is rotated at an angle θ with respect to the nanowire axis to select THz polarization post-transmission.

6.6 Polarization Dependence of the THz Transmission

Photoexcited carriers in oriented nanowires are expected to exhibit a polarization dependent THz response due to the geometries depicted in 6.5. To study this phenomenon, the incident THz electric field was polarized at 45° with respect to the nanowires (see 6.7). As a result, the field had components both parallel and perpendicular to the nanowires. After transmission through the nanowire sample, the field polarization was selected for measurements of $\Delta t/t$ by rotating the polarizer through an angle θ with respect to the nanowires.

Figure 6.8 shows the measured values of $|\Delta t/t|$ for different angles θ. The most striking feature of the data is the absence of any measurable THz response when the field is polarized perpendicular to the nanowires. In this case, the surface plasmon frequency Ω_p equals $\omega_p \sqrt{\epsilon_s/(\epsilon_s + \epsilon_\circ)}$ and is in the tens of THz range for the photoexcited carrier densities in these experiments. From Eq. 6.2, it can

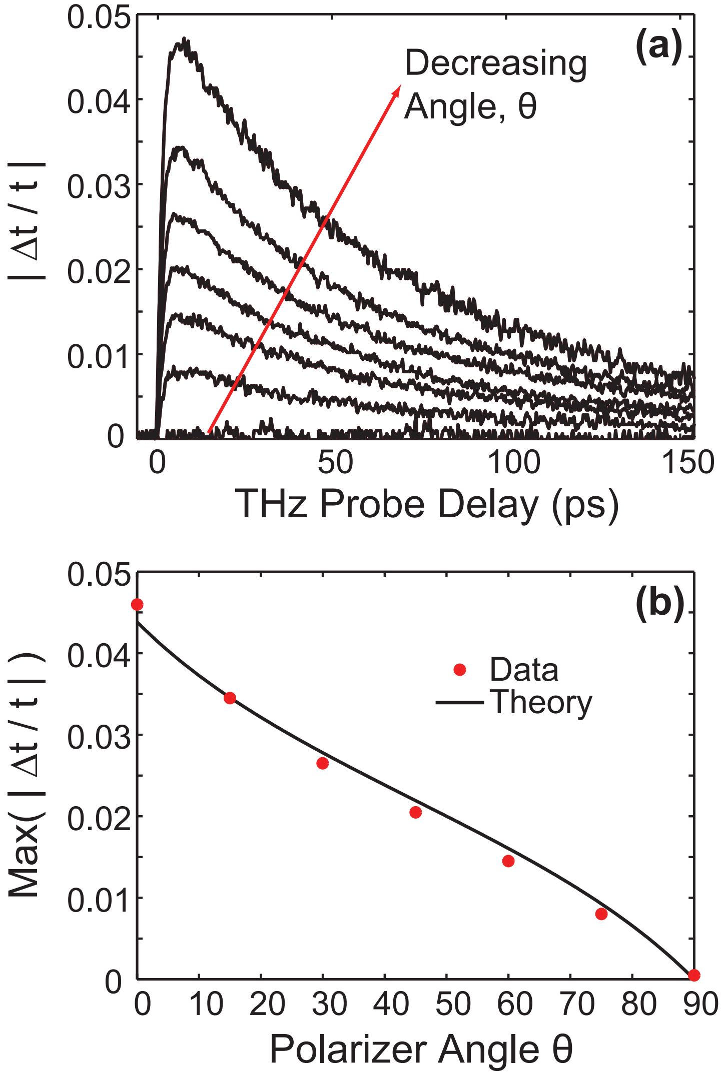

Figure 6.8: (a) Measured differential terahertz transmission $|\Delta t/t|$ for polarizer angles of $\theta = 0, 15, 30, 45, 60, 75, 90$ degrees. At $\theta = 90$ degrees, $|\Delta t/t|$ is negligibly small and lost in the noise. (b) Maximum values of $|\Delta t/t|$ from 6.8(a) are plotted versus the polarizer angle θ. The angular dependence expected from the theory is also plotted (solid line).

be seen that when $\Omega_p \gg \omega$ and the product $\omega\tau$ is not too small, the induced current is significantly reduced compared to the case when $\Omega_p \ll \omega$. Therefore, for perpendicular THz field components the depolarization field is strong enough to suppress the induced current, and so the resulting THz response is much weaker compared to that for parallel components. In this way, the shape anisotropy of the nanowires on subwavelength scales determines the polarization dependence of the THz response. Assuming that the THz response of oriented nanowires is negligibly small when the field is polarized perpendicular to the nanowires, the measured THz transmission is expected to be proportional to the cosine of the angle between the field polarization and the nanowire axis. In our experiments, since the field polarization is selected post-transmission, the measured values of $|\Delta t/t|$ are expected to be proportional to $\cos(\theta)/\cos(\pi/4-\theta)$. 6.8(b) shows that the (peak) values of $|\Delta t/t|$ exhibit exactly this angular dependence.

APPENDIX A

AMPLITUDE TRANSMISSION COEFFICIENT OF EPITAXIAL GRAPHENE

Consider a plane wave propagating in free space with electric field $E_i\mathbf{x}$ and wave vector $k_i\mathbf{z}$ incident upon a SiC substrate with N thin layers of epitaxial graphene, as shown in Fig. A.1. Each graphene layer has 2D conductivity σ (units: $Amps/Volt$). The reflected and transmitted electric fields are labelled E_r and E_t, respectively and the SiC substrate has a refractive index of n.

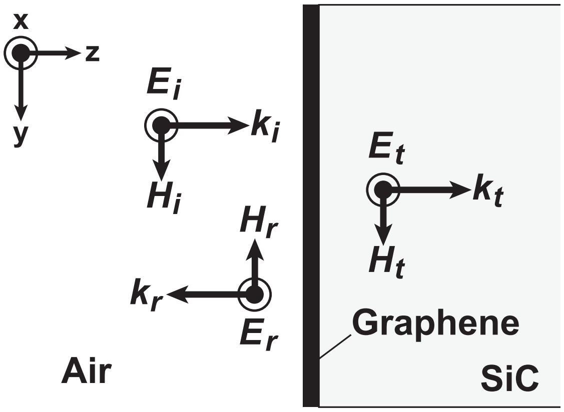

Figure A.1: The interface bewteen air and epitaxial graphene grown on a SiC substrate. The graphene layers are extremely thin compared to the wavelength of the incident radiation and can therefore be treated as infinitely thin conductive sheets with a 2D conductivity.

From Maxwell's Equations, the boundary conditions for the electric and magnetic fields at the air-graphene interface are [99],

$$E_i + E_r = E_t \tag{A.1}$$

$$H_i - H_r = H_t + N\sigma E_t \tag{A.2}$$

Using the standard definition for amplitude reflection and transmission co-effiecients, $r = E_r/E_i$ and $t = E_t/E_i$, Eq. (A.2) can be rewritten as

$$2 - t(1 + n) = N\sigma\eta_o t \tag{A.3}$$

where η_o is the impedance of free space. This equation then simplifies to

$$t = \frac{2}{1+n}\frac{1}{1+\frac{N\sigma\eta_o}{1+n}} \tag{A.4}$$

The first term on the right is the amplitude transmission coefficient of an air-SiC substrate without any graphene layers.

APPENDIX B

DERIVATION OF THE INTRABAND CONDUCTIVITY OF GRAPHENE

The longitudinal dielectric function of graphene in the relaxation time approximation, ϵ, can be written as [98, 100],

$$\epsilon(\mathbf{q}, \omega) = 1 - V(\mathbf{q})\Pi(\mathbf{q}, \omega) \tag{B.1}$$

where $\mathbf{q}$ is the longitudinal plasmon wave vector, $V(\mathbf{q}) = e^2/2\epsilon q$ is the bare 2D Coulomb interaction energy and $\Pi(\mathbf{q}, \omega)$ is the electron-hole propagator [92] which is related to the well-known Lindhard potential [100, 101, 102]. The propagator describes the self-consistent dielectric response of an electron gas to an externally applied potential. The induced charge density in the electron gas $\rho(\mathbf{q}, \omega)$ is [101],

$$\rho(\mathbf{q}, \omega) = e^2\Pi(\mathbf{q}, \omega)\phi(\mathbf{q}, \omega) \tag{B.2}$$

Using $\mathbf{E} = -\nabla\phi$, and assuming that the charge density can be written as a time-harmonic plane-wave, this expression becomes

$$\rho(\mathbf{q}, \omega) = i\frac{e^2}{|\mathbf{q}|}\Pi(\mathbf{q}, \omega)E(\mathbf{q}, \omega) \tag{B.3}$$

From the charge continuity equation and definition of conductivity [99], it can easily be shown that

$$\rho(\mathbf{q}, \omega) = \frac{\sigma}{\omega}\mathbf{q} \cdot E(\mathbf{q}, \omega) \tag{B.4}$$

Finally, Eq. B.3 and Eq. B.4 are combined to arrive at the following expression for the complex conductivity, $\sigma(\mathbf{q},\omega)$, as a function of $\Pi(\mathbf{q},\omega)$,

$$\sigma(\mathbf{q},\omega) = \frac{i\omega e^2}{|\mathbf{q}|^2}\Pi(\mathbf{q},\omega) \tag{B.5}$$

This conductivity has both intraband and interband contributions that are related to the intraband and interband components of the propagator. From [92], the the intraband component of the collisionless propagator, $\Pi^0_{intra}(\mathbf{q},\omega)$, can be calculated from the following 2D k-space integral,

$$\Pi^0_{intra}(\mathbf{q},\omega) = 4\int \frac{d\mathbf{k}}{(2\pi)^2}\left(1 + \frac{|\mathbf{k}| + \mathbf{k}\cdot\mathbf{q}/|\mathbf{k}|}{|\mathbf{k}+\mathbf{q}|}\right)\frac{f(\mathbf{k}) - f(\mathbf{k}+\mathbf{q})}{\hbar\omega + i\eta + E(\mathbf{k}) - E(\mathbf{k}+\mathbf{q})} \tag{B.6}$$

In the long-wavelength limit, the intraband conductivity should be independent of $\mathbf{q}$. Therefore, from Eq. B.5, Equation B.6 must be expanded to second-order in $\mathbf{q}$. To start, the integrand can easily be rewritten as

$$\begin{aligned}\Pi^0_{intra}(\mathbf{q},\omega) \quad = \quad & 4\int \frac{d\mathbf{k}}{(2\pi)^2}\left(1 + \frac{|\mathbf{k}| + |\mathbf{q}|\cos\theta}{|\mathbf{k}+\mathbf{q}|}\right)f(\mathbf{k})\cdot \\ & \left[\frac{1}{\hbar\omega + i\eta + E(\mathbf{k}) - E(\mathbf{k}+\mathbf{q})} - \frac{1}{\hbar\omega + i\eta + E(\mathbf{k}-\mathbf{q}) - E(\mathbf{k})}\right]\end{aligned} \tag{B.7}$$

Keeping only terms up to second-order in $\mathbf{q}$, the propagator simplifies to

$$\Pi^0_{intra}(\mathbf{q},\omega) \approx 4|\mathbf{q}|^2\frac{\hbar\upsilon}{(\hbar\omega + i\eta)^2}\int \frac{d\mathbf{k}}{(2\pi)^2}f(\mathbf{k})\frac{1}{|\mathbf{k}|} \tag{B.8}$$

This integral can be transformed from k-space to energy using the linear energy-momentum dispersion relation in graphene $E = \hbar\upsilon_f|\mathbf{k}|$. As a reminder to the reader, only the low-energy electrons in graphene located near the Dirac Points are characterized by linear dispersion.

$$\Pi^0_{intra}(\mathbf{q},\omega) \approx \frac{2}{\pi}|\mathbf{q}|^2 \frac{\hbar v}{(\hbar\omega + i\eta)^2} \int_0^\infty dE f(E) \tag{B.9}$$

The dielectric function in Eq. B.1 for an electron gas with a scattering time τ is related to the collisionless Linhdard dielectric constant, $\epsilon^0(\mathbf{q},\omega) = 1 - V(\mathbf{q})\Pi^0(\mathbf{q},\omega)$ by [98],

$$\epsilon(\mathbf{q},\omega) = 1 + \frac{(1 + i/\omega\tau)(\epsilon^0(\mathbf{q},\omega + i/\tau) - 1)}{1 + (i/\omega\tau)((\epsilon^0(\mathbf{q},\omega + i/\tau) - 1)/(\epsilon^0(\mathbf{q},0) - 1))} \tag{B.10}$$

Equation B.9 is substituted into Eq. B.10 and the limit as $\eta \to 0$ is taken. By comparing the resulting expression for $\epsilon(\mathbf{q},\omega)$ in Eq. B.1, the propagator for graphene with an electron scattering time τ is

$$\Pi_{intra}(\mathbf{q},\omega) = 2|\mathbf{q}|^2 \frac{1}{\pi\hbar^2\omega(\omega + i/\tau)} \int_0^\infty dE f(E) \tag{B.11}$$

This result is then be substituted into the expression for conductivity in Eq. B.5. Finally, the intraband conductivity of graphene is

$$\sigma_{intra} = 2i \frac{e^2/\pi\hbar^2}{\omega + i/\tau} \int_0^\infty dE f(E) \tag{B.12}$$

The result in Eq. B.12 is identical to that given in [85].

BIBLIOGRAPHY

[1] X.C. Zhang, J.T. Darrow, B.B. Hu, D.H. Auston, M.T. Schmidt, P. Tham and E.S. Yang, ″Optically induced electromagnetic radiation from semiconductor surfaces″, Appl. Phys. Lett. **56**, 2228 (1990).

[2] J.N. Heyman, P. Neocleous, D. Hebert, P.A. Crowell, T. Muller and K. Unterrainer, ″Terahertz emission from GaAs and InAs in a magnetic field″, Phys. Rev. B **64**, 85202 (2001).

[3] P. Gu, M. Tin, S. Kono, K. Sakai and X.C. Zhang, ″Study of terahertz radiation from InAs and InSb″, J. Appl. Phys. **91**, 5533 (2002).

[4] R. Ascazubi, I. Wilke, K. Denniston, H. Lu and W.J. Schaff, ″Terahertz emission by InN″, Appl. Phys. Lett. **84**, 4810 (2004).

[5] R. Adomavieius, A. Urbanowicz, G. Molis, A. Krotkus and E. Satkovskis, ″Terahertz emission from p-InAs due to the instantaneous polarization″, Appl. Phys. lett. **85**, 2463 (2004).

[6] R. Mendis, M. L. Smith, L. J. Bignell, R. E. M. Vickers, and R. A. Lewis, ″Strong terahertz emission from (100) p-type InAs″, J. Appl. Phys. **98**, 126104 (2005).

[7] P. LeFur and D.H. Auston, ″A kilovolt picosecond optoelectronic switch and Pockel's cell″, Appl. Phys. Lett. **28**, 21 (1976).

[8] D.H. Auston, K.P. Cheung, and P.R. Smith, ″Picosecond photoconducting Hertzian dipolse″, Appl. Phys. Lett. **45**, 284 (1984).

[9] D. Grischkowsky, M.B. Ketchen, C.C. Chi, I.N. Dulling, N.J. Halas, J.M. Halbout and P.G. May, ″Capacitance free generation and detection of subpicosecondelectrical pulses on coplanar transmission lines″, IEEE J. Quant. Elect. **24**, 221 (1988).

[10] N. Katzenellenbogen and D. Grischkowsky, ″Efficient generation of 380 fs pulses of THz radiation by ultrafast laser pulse excitation of a biased metal-semiconductor interface″, Appl. Phys. Lett. **58**, 222 (1991).

[11] D. Grischkowsky and N. Katzenellenbogen, ″Femtosecond pulses of terahertz radiation: physics and applications″, OSA Proc. on Picosecond Electronics and Optoelectronics **9**, 9 (1992).

[12] J.E. Pedersen, V.G. Lyssenko, J.M. Hvam, P.U. Jepsen, S.R. Keiding, C.B. Sorensen and P.E. Lindelof, ”Ultrafast local field dynamics in photoconductive THz antennas”, Appl. Phys. Lett. **62**, 1265 (1993).

[13] E. Castro-Camus, J. Lloyd-Hughes and M.B. Johnston, ”Three-dimensional carrier-dynamics simulation of terahertz emission from photoconductive switches”, Phys. Rev. B **71**, 195301 (2005).

[14] J.B. Khurgin, ”Optical rectification and terahertz emission in semiconductors excited above the band gap”, J. Opt. Soc. Am. B **11** 2492 (1994).

[15] G.L. Dakovski, B. Kubera and J. Shan, ”Localized terahertz generation via optical rectification in ZnTe”, J. Opt. Soc. Am. B **22**, 1667 (2005).

[16] Q. Chen, M. Tani and X. C. Zhang, ”Electro-optic transceivers for terahertz-wave applications”, J. Opt. Soc. Am. B **18**, 823 (2001).

[17] Y.S. Lee, T. Meade, M. DeCamp and T.B. Norris, ”Temperature dependence of narrow-band terahertz generation from periodically poled lithium niobate”, Appl. Phys. Lett. **77**, 1244 (2000).

[18] A.G. Stepanov, J. Hebling and J. Kuhl, ”Efficient generation of subpicosecond terahertz radiation by phase-matched optical rectification using ultrashort laser pulses with tilted pulse fronts”, Appl. Phys. Lett **83** 3000 (2003).

[19] P.Y. Han, M. Tani, F. Pan and X.C. Zhang, ”Use of the organic crystal DAST for terahertz beam applications”, Opt. Lett. **25**, 675 (2000).

[20] A. Schneider, M. Neis, M. Stillhart, B. Ruiz, R. U.A. Khan and P. Gnter, ”Generation of terahertz pulses through optical rectification in organic DAST crystals: theory and experiment”, J. Opt. Soc. Am. B **23**, 1822 (2006).

[21] K.L. Yeh, M.C. Hoffmann, J. Hebling and K.A. Nelson, ”Generation of 10 J ultrashort terahertz pulses by optical rectification”, Appl. Phys. Lett. **90** 171121 (2007).

[22] Q. Wu and Q.C. Zhang, ”Free-space electro-optic sampling of terahertz beams”, Appl. Phys. Lett. **67**, 3523 (1995).

[23] G. Gallot and D. Grischkowsky, ”Electro-optic detection of terahertz radiation”, J. Opt. Soc. Am. B **16**, 1204 (1999).

[24] A. Nahata, D.H. Auston, T.F. Heinz and C. Wu, ”Coherent detection of freely propagating teraherz radiation by electro-optics sampling”, Appl. Phys. Lett. **68**, 150 (1996).

[25] R.W. Boyd, *Nonlinear Optics*, Academic Press, Boston, USA (2008).

[26] A. Leitenstorfer, S. Hunsche, J. Shah, M.C. Nuss and W.H. Knox, ”Detectors and sources for ultrabroadband electro-optic sampling: experiment and theory”, Appl. Phys. Lett. **74**, 1515 (1999).

[27] Q. Wu and Q.C. Zhang, ”7 terahertz broadband GaP electro-optic sensor”, Appl. Phys. Lett. **70**, 1784 (1996).

[28] C. Winnewisser, P.U. Jepsen, M. Schall, V. Schyja and H. Helm, ”Electro-optic detection of THz radiation in LiTaO3, LiNbO3 and ZnTe”, Appl. Phys. Lett. **70**, 3069 (1997).

[29] G. Gallot, J. Zhang, R.W. McGowan, T.I. Jeon and D. Grischkowsky, ”Measurements of the THz absorption and dispersion of ZnTe and their relevance to the electro-optic detection of THz radiation”, Appl. Phys. Lett. **74**, 3450 (1999).

[30] R. Huber, A. Bordschelm, F. Tauser and A. Leitenstorfer, ”Generation and field-resolved detection of femtosecond electromagnetic pulses tunable up to 41 THz”, Appl. Phys. Lett. **76**, 3191 (2000).

[31] K.P.H. Lui and F.A. Hegmann, ”Ultrafast carrier relaxation in radiation-damaged silicon on sapphire studied by optical-pump-terahertz-probe experiments”, Appl. Phys. Lett. **78**, 3478 (2001).

[32] P.A. George, J. Strait, J. Dawlaty, S. Shivaraman, M.V.S. Chandrashekhar, F. Rana and M.G. Spencer, ”Ultrafast optical-pump terahertz-probe spectroscopy of the carrier relaxation and recombination dynamics in epitaxial graphene”, Nano Lett. **8**, 4248 (2008).

[33] P. Parkinson, J. Lloyd-Hughes, Q. Gao, H.H. Tan, C. Jagadish, M.B. Johnston and L.M. Herz, ”Transient terahertz conductivity of GaAs nanowires”, Nano Lett. **7**, 2162 (2007).

[34] J.H. Strait, P.A. George, M. Levendorf, M. Blood-Forsythe, F. Rana and J. Park, ”Measurements of the carrier dynamics and terahertz response of

oriented germanium nanowires using optical-pump terahertz-probe spectroscopy", (accepted Nano. Lett., 2009).

[35] J.S. Melinger, N. Laman, S.S. Harsha, D. Grischkowsky, "Line narrowing of terahertz vibrational modes for organic thin polycrystalline films within a parallel plate waveguide", Appl. Phys. Lett. **89,** 251110 (2006).

[36] M. Nagel, P.H. Bolívar, M. Bruscherseifer, H. Kurz, A. Bosserhoff, R. Büttner, "Integrated planar terahertz resonators for femtomolar sensitivity label-free detection of DNA", Appl. Opt. **41,** 2074 (2002).

[37] H. Kurt, D.S. Citrin, "Photonic crystals for biochemical sensing in the terahertz region", Appl. Phys. Lett. **87,** 041108 (2005).

[38] G. Fasching, A. Benz, K. Unterrainer, R. Zobl, A.M. Andrews, T. Roch, W. Schrenk, G. Strasser, "Terahertz microcavity quantum-cascade lasers", Appl. Phys. Lett. **87,** 211112 (2005).

[39] P.A. George, C. Manolatou, F. Rana, A.I. Akinwande, "Integrated microcavity klystrons for generating high power coherent THz radiation", 2005 Conf. Las. Elect. Opt., CThX5 (2005).

[40] G. Gallot, S.P. Jamison, R.W. McGowan, D. Grischkowsky, "Terahertz waveguides", J. Opt. Soc. Am. B **17,** 851 (2000).

[41] R. Mendis, D. Grischkowsky, "Undistorted guided-wave propagation of subpicosecond terahertz pulses", Opt. Lett. **26,** 846 (2001).

[42] K. Wang, D.M. Mittleman, "Metal wires for terahertz wave guiding", Nature **432,** 376 (2004).

[43] M. Wächter, M. Nagel, H. Kurz, "Metallic slit waveguide for dispersion-free low-loss terahertz signal transmission", Appl. Phys. Lett. **90,** 061111 (2007).

[44] A.L. Bingham, D. Grischkowsky, "High Q, one-dimensional terahertz photonic waveguides", Appl. Phys. Lett. **90,** 091105 (2007).

[45] A.L. Bingham, D. Grischkowsky, "Terahertz two-dimensional high-Q photonic crystal waveguide cavities", Opt. Lett. **92,** 348 (2008).

[46] K. Vahala, *Optical Microcavities* (World Scientific, New Jersey, 2004).

[47] D. M. Pozar, *Microwave Engineering* (Wiley, New Jersey, 2005), pp. 687.

[48] B. Williams, H. Callebaut, S. Kumar, Q. Hu, ″3.4-THz quantum cascade laser based on longitudinal-optical-phonon scattering for depopulation″, Appl. Phys. Lett. **82,** 1015 (2003).

[49] C.H. Tsau, S.M. Spearing, M.A. Schmidt, ″Wafer-level thermocompression bonds″, J. of Micromech. Sys. **11,** 641 (2002).

[50] C. Manolatou, M.J. Khan, S. Fan, P.R. Villeneuve, H.A. Haus, J. Joannopoulos, ″Coupling of modes analysis of resonant channel add-drop filters″, IEEE J. Quant. Elect. **35,** 1322 (1999).

[51] N. Laman, D. Grischkowsky, ″Reduced conductivity in the terahertz skin-depth layer of metals″, Appl. Phys. Lett. **90,** 122115 (2007).

[52] S. Hayward and N. Go, ″Collective variable description of native protein dynamics″, Ann. Rev. Phys. Chem. **46**, 223 (1995).

[53] M.C. Chen and R.C. Lord, ″Laser-excited Raman spectroscopy of biomolecules: conformational study of bovine serum albumin″, J. Am. Chem. Soc. **98**, 990 (1976).

[54] W. Zhuang, Y. Feng, and E.W. Prohofsky, ″Self-consistent calculation of localized DNA vibrational properties at a double-helix–single-strand junction with anharmonic potential″, Phys. Rev. A **41**, 7033 (1990).

[55] A.G. Markelz, and A. Roitberg, and E.J. Heilweil, ″Pulsed terahertz spectroscopy of DNA, bovine serum albumin and collagen between 0.1 and 2.0 THz″, Chem. Phys. Lett. **320**, 42 (2000).

[56] T.R. Globus, D.L. Woolard, T. Khromova, T.W. Crowe, M. Bykhovskaia, B.L. Gelmont, J. Hesler, and A.C. Samuels, ″THz-spectroscopy of biological molecules″, J. Bio. Phys. **29**, 89 (2003).

[57] T.R. Globus, D.L. Woolard, T.W. Crowe, T. Khromova, M. Bykhovskaia, B.L. Gelmont, and J. Hesler, ″Terahertz Fourier transform characterization of biological materials in a liquid phase″, J. Phys. D **39**, 3405 (2006).

[58] J. Xu, K.W. Plaxco, and S.J. Allen, ″Probing the collective vibrational dynamics of a protein in liquid water by terahertz absorption spectroscopy″, Prot. Sci. **15**, 1175 (2006).

[59] J. Kitagawa, T. Ohkubo, M. Onuma, and Y. Kadoya, ”THz spectroscopic characterization of biomolecule/water systems by compact sensor chips”, Appl. Phys. Lett. **89**, 041114 (2006).

[60] T. Baras, T. Kleine-Ostmann, and M. Koch, ”On-chip THz detection of biomaterials: a numerical study”, J. Bio. Phys. **29**, 187 (2003).

[61] M. Nagel, P.H. Bolivar, M. Brucherseifer, H. Kurz, A. Bosserhoff, and R. Büttner, ”Integrated THz technology for label-free genetic diagnostics”, Appl. Phys. Lett. **80**, 154 (2002).

[62] ”Zeonor Production Information Sheet”, Zeon Corporation (2004).

[63] T.I. Wallow, A.M. Morales, B.A. Simmons, M.C. Hunter, K.L. Krafcik, L.A. Domeier, S.M. Sickafoose, K.D. Patel, and A. Gardea, ”Low-distortion, high-strength bonding of thermoplastic microfluidic devices employing case-II diffusion-mediated permeant activation”, Lab on a Chip **7**, 1825 (2007).

[64] B.G. Hawkins, A.E. Smith, Y.A. Syed, and B.J. Kirby, ”Continuous-flow particle separation by 3D insulative dielectrophoresis using coherently shaped, dc-biased, ac electric fields”, Anal. Chem. **79**, 7291 (2007).

[65] ”Bovine Serum Albumin Product Information Sheet”, Sigma-Aldrich (2000).

[66] R.D. Levine, *Molecular Reaction Dynamics*, Cambridge Univeristy Press (2005).

[67] D.L. Woolard, W.R. Loerep, M.S. Shur, *Terahertz Sensing Technology: Vol. 1 and 2* (World Scientific, New Jersey, 2003).

[68] A. Markelz, S. Whitmire, J. Hillebrecht, R. Birge, ”THz time domain spectroscopy of biomolecular conformational modes”, Phys. Med. Biol., **47,** 3797 (2002).

[69] J. Xu, K.W. Plaxco, S.J. Allen, ”Collective dynamics of lysozyme in water: terahertz absorption spectroscopy and comparison with theory”, J. Phys. Chem. B **110,** 24255 (2006).

[70] R. Saito, G. Dresselhaus and M. . Dresselhaus, *Physical Properties of Carbon Nanotubes*, Imperial College Press, London, UK (1999).

[71] A.H. Castro Neto, F. Guinea, N.M.R. Peres, K.S. Novoselov and A.K. Geim, ”The electronic properties of graphene”, arXiv:con-mat/0709.1163 (2007).

[72] T. Ando, T. Nakanishi and R. Saito, ”Berry’s phase and absence of back scattering in carbon nanotubes”, J. Phys. Soc. Jap. **67**, 2857 (1998).

[73] K.S. Novoselov, A.K. Geim, S.V. Morozov, D. Jian, M.I. Katsnelson, I.V. Grigorieva, S.V. Dubonos and A.A. Firsvo, ”Two-dimensional gas of massless Dirac fermions in graphene”, Nature **438**, 197 (2005).

[74] Y. Zhang, Y. Tan, H.L. Stormer and P. Kim, ”Experimental observation of the quantum Hall effect and Berry’s phase in graphene”, Nature **438**, 201 (2005).

[75] G. Liang, N. Neophytou, D.E. Nikonov and M.S. Lundstrom, ”Performance projections for ballistic graphene nanoribbon field-effect transistors”, IEEE Trans. Elec. Dev. **54**, 657 (2007).

[76] C. Berger, Z. Song, X. Li, X. Wu, N. Brown, C. Naud, D. Mayou, T. Li, J. Hass, A.N. Marchenkov, E. H. Conrad, P. N. Frist and W. A. de Heer, ”Electronic confinement and coherence in patterned epitaxial graphene”, Science **213**, 1191 (2006).

[77] F. Rana, ”Graphene terahertz plasmon oscillators”, IEEE Trans. Nanotechnology **7**, 91 (2008).

[78] J.M. Dawlaty, S. Shivaraman, M. Chandrashekhar, F. Rana and M. G. Spencer, ”Measurement of ultrafast carrier dynamics in epitaxial graphene”,Appl. Phys. Lett. **92**, 042116 (2008).

[79] D. Sun, Z. Wu, C. Divin, X. Li, C. Berger, W. A. de Heer, P. First and T. Norris, ”Hot Dirac fermions in epitaxial graphene”, arXiv:con-mat/0803.2883 (2008).

[80] D. Song, K.F. Mak, Y. Wu, C.H. Lui, M. Sfeir, S. Rosenblatt, H. Yan, J. Maultzsch and T. Heinz, ”Experimental measurement of ultrafast carrier dynamics in mono-and multi-layer graphene samples”, Bul. of Am. Phys. Soc. **53**, L29.7 (2008).

[81] T. Hertel and G. Moos, ”Electron-phonon interaction in single-wall carbon nanotubes: A time-domain study”, Phys. Rev. Lett. **84**, 5002 (2000).

[82] F. Rana, P.A. George, J.H. Strait, J. Dawlaty, S. Shivaraman, MVS Chandrashekhar, and M.G. Spencer, ”Carrier recombination and generation rates for intravalley and intervalley phonon scattering in graphene”, Phys. Rev. B **79**, 115447 (2009).

[83] T. Kampfrath, L. Perfetti, F. Schapper, C. Frischkorn and M. Wolf, ”Strongly coupled optical phonons in the ultrafast dynamics of the electronic energy and current relaxation in graphite”, Phys. Rev. Lett. **95**, 187403 (2005).

[84] G.G. Samsonidze, E.B. Barros, R. Saito, J. Jiang, G. Dresselhaus and M.S. Dresselhaus1, ”Electron-phonon coupling mechanism in two-dimensional graphite and single-wall carbon nanotubes”, Phys. Rev. B **75**, 155420 (2007).

[85] J.M. Dawlaty, S. Shivaraman, J. Strait, P. George, M. Chandrashekhar, F. Rana, M.G. Spencer, D. Veksler and Y. Chen, ”Measurement of the optical absorption spectra of epitaxial graphene from terahertz to visible”, Appl. Phys. Lett. **93**, 131905 (2008).

[86] W.A. de Heer, C. Berger, X. Wu, P.N. First, E.H. Conrad, X. Li. T. Li, M. Sprinkle, J. Hass, M. Sadowski, M. Potemski and G. Martinez, ”Epitaxial graphene”, arXiv:con-mat/0704.0285 (2007).

[87] C. Faugeras, A. Nerriere, M. Potemski, A. Mahmood, E. Dujardin, C. Berger and W.A. de Heer, ”Few layer graphene on SiC, pyrolitic graphite and graphene: a Raman scattering study”, arXiv:con-mat/0709.2538 (2000).

[88] A.C. Ferrari and J. Robertson, ”Interpretation of Raman spectra of disordered and amorphous carbon”, Phys. Rev. B **61**, 14095 (2000).

[89] W.K. Tse, E.H. Hwang, and S. Das Sarma, ”Ballistic hot electron transport in graphene”, arXiv:con-mat/0806.0436 (2008).

[90] V. Perebeinos, J. Tersoff and P. Avouris, ”Electron-phonon interaction and transport in semiconducting carbon nanotubes”, Phys. Rev. Lett. **94**, 086802 (2005).

[91] E.H. Hwang and S. Das Sarma, ”Dielectric function, screening, and plasmons in two-dimensional graphene”, Phys. Rev. B **75**, 205418 (2007).

[92] F. Rana and F.R. Ahmad, ”Plasmon amplification through stimulated emission at terahertz frequencies in graphene”, arXiv:con-mat/0704.0607v2 (2007).

[93] F. Rana, ”Electron-hole generation and recombination rates for Coulomb scattering in graphene”, Phys. Rev. B **76**, 155431 (2007).

[94] P. Harrison, *Quantum Wells, Wires, and Dots*, John Wiley and Sons, NY (USA) (2005).

[95] B.Y. Hu, E.H. Hwang, S.D. Sarma, ”Density of states of disordered graphene”, arXiv:con-mat/0805.2148 (2008).

[96] C.H. Grein, H. Ehrenreich, ”Modeling of disorder influenced Auger recombination in strained-layer type-II superlattices”, J. Appl. Phys., **93**, 1075 (2003).

[97] M. Takeshima, ”Theory of phonon-assisted Auger recombination in semiconductors”, Phys. Rev. B., **23**, 771 (1981).

[98] N.D. Mermim, ”Lindhard dielectric function in the relaxation-time approximation”, Phys. Rev. B, **1**, 2362 (1970).

[99] H. Haus and J. Melcher, *Electromagnetic Fields and Energy*, Prentice Hall, NY, USA (1989).

[100] H. Haug and S. Koch, *Quantum Theory of the Optical and Electroni Properties of Semiconductors*, World Scientific, London, UK (2005).

[101] H. Ehrenreich and M.H. Cohen, ”Self-consistent field approach to the many-electron problem”, Phys. Rev. **115**, 786 (1959).

[102] C. Kittel, *Quantum Theory of Solids*, Wiley (1987).

[103] B. Tian and T. J. Kempa and C. M. Lieber, ”Single nanowire photovoltaics”, Chem. Soc. Rev. **38**, 16 (2009).

[104] W. Lu and C. M. Lieber, ”Nanowire transistor performance limits and applications”, IEEE Trans. Electron Dev. **55**, 2859 (2008).

[105] D.J. Surbuly, M. Law, H. Yan and P. Yang, ”Semiconductor nanowires for subwavelength photonics integration”, J. Phys. Chem. B **109**, 15190 (2005).

[106] Y.H. Ahn and J. Park, ”Efficient visible light detection using individual germanium nanowire field effect transistors”, ppl. Phys. Lett. **91**, 162102 (2007).

[107] M. Law, J. Goldberger and Peidong Yang, ”Semiconductor Nanowires and Nanotubes”, Annu. Rev. Mater. Res. **34**, 83 (2004).

[108] R. Agarwal and C.M. Lieber, ”Semiconductor nanowires: ptics and optoelectronics”, Appl. Phys. A **85**, 209 (2006).

[109] R.P. Prasankumar, S. Choi, S.A. Trugman, S.T. Picraux and A.J. Taylor, ”Ultrafast electron and hole dynamics in germanium nanowires”, Nano. Lett. **8**, 1619 (2008).

[110] C.K. Sun. S.Z. Sun, K.H. Lin, K.Y.J. Zhang, H.L. Liu, S.C. Liu and J.J. Wu, ”Ultrafast carrier dynamics in ZnO nanorods”, Appl. Phys. Lett. **87**, 023106 (2005).

[111] Y. Cui, L.J. Lauhon, M.S. Gudiksen, J. Wang and C.M. Lieber, ”Diameter-controlled synthesis of single-crystal silicon nanowires”, Appl. Phys. Lett. **78**, 2214 (2001).

[112] H. Jagannathan, M. Deal, Y. Nishi, J. Woodruff, C. Chidsey and Paul C. McIntyre, ”Nature of germanium nanowire heteroepitaxy on silicon substrates”, J. of Appl. Phys. **100**, 024318 (2006).

[113] Z. Fan, J.C. Ho, Z.A. Jacobson, R. Yerushalmi, R.L. Alley, H. Razavi and A. Javey, ”Wafer-scale assembly of highly ordered semiconductor nanowire arrays by contact printing”, Nano. Lett. **8**, 20 (2008).

[114] D.W. Bailey and C.J. Stanton, ”Calculations of femtosecond differential optical transmission in germanium”, J. Appl. Phys. **77**, 2107 (1994).

[115] K. Tanaka, H. Ohtake, H. Nansei, and T. Suemoto, ”Subpicosecond hot-hole relaxation in germanium studied by time-resolved inter-valence-band Raman scattering”, Phys. Rev. B **52**, 10709 (1995).

[116] A. Urbanowicz, R. Adomavičius and A. Krotkus, ”Terahertz emission from photoexcited surfaces of Ge crystals”, Phys. B **367**, 152 (2005).

[117] E. Gaubas, M. Bauža, A. Uleckas and J. Vanhellenmont, ”Carrier lifetime studies in Ge using microwave and intrared light techniques”, Mat. Sci. in Semicond. Proc. , 781 (2006).

[118] F. Léonard, A.A. Talinm, B.S. Swartzentruber and S.T. Picraux, ”Diameter-

dependent electronic transport properties of Au-catalyst/Ge-nanowire Schottky diodes", Phys. Rev. Lett. **102**, 106805 (2009).

[119] C. Kittel, *Introduction to Solid State Physics*, John Wiley & Sons (2005).

[120] J.M. Pitarke, V.M. Silkin, E.V. Chulkov and P.M. Echenique, "Theory of surface plasmons and surface-plasmon polaritons", Rep. on Prog. in Phys **70**, 1 (2007).

[121] H.K. Nienhuys and V. Sundström, "Influence of plasmons on terahertz conductivity measurements", Appl. Phys. Lett. **87**, 012101 (2005).

[122] O. Madelung, *Semiconductors: Group IV Elements and III-V Compounds*, Springer-Verlag (1991).

[123] C.M. Randall and R.D. Rawcliffe, "Refractive indices of germanium, silicon, and fused quartz in the far infrared", Appl. Opt. **6**, 1889 (1967).

[124] R.S. Muller and T.I. Kamins, *Device Electronics for Integrated Circuits*, John Wiley & Sons (2003).